PHOTO-PHYSICAL STUDIES AND BANDGAP ENGINEERING ON TRANSITION METAL CHALCOGENIDES FOR APPLICATIONS IN PHOTOCATALYSIS
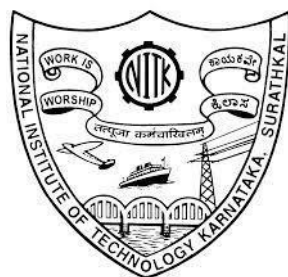
Thesis

submitted in partial fulfilment of the requirements for the degree of

DOCTOR OF PHILOSOPHY

by

SULAKSHANA SHENOY

DEPARTMENT OF PHYSICS

NATIONAL INSTITUTE OF TECHNOLOGY KARNATAKA,

SURATHKAL, MANGALORE-575025

OCTOBER, 2021

DECLARATION

by the Ph.D. Research Scholar

I hereby *declare* that the research thesis entitled **"PHOTO-PHYSICAL STUDIES AND BANDGAP ENGINEERING ON TRANSITION METAL CHALCOGENIDES FOR APPLICATIONS IN PHOTOCATALYSIS"**, which is being submitted to the **National Institute of Technology Karnataka, Surathkal** in partial fulfilment of the requirements for the award of the **Degree of Doctor of Philosophy in Physics** is a *bonafide report of the research work carried out by me under the guidance of Dr. Kartick Tarafder and Dr. Kishore Sridharan*. The material contained in this research thesis has not been submitted to any University or Institution for the award of any degree.

Sulakshana
08|10|2021

Sulakshana Shenoy

Register Number: 165116PH16F06

Department of Physics

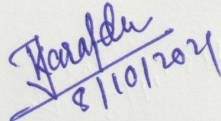National Institute of Technology

Karnataka, Surathkal

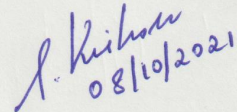Place: NITK-Surathkal

Date: 08-10-2021

CERTIFICATE

This is to *certify* that the research thesis entitled **"PHOTO-PHYSICAL STUDIES AND BANDGAP ENGINEERING ON TRANSITION METAL CHALCOGENIDES FOR APPLICATIONS IN PHOTOCATALYSIS"**, submitted by **Sulakshana Shenoy** (Register Number: 165116PH16F06) as the record of the research work carried out by her, is *accepted as the research thesis submission* in partial fulfillment of the requirements for the award of degree of Doctor of Philosophy.
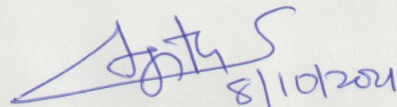
Research Supervisors

Dr. Kartick Tarafder
Assistant Professor
Department of Physics
NITK Surathkal-575025

Dr. Kishore Sridharan
UGC-Assistant Professor
Department of Nanoscience and
Technology
University of Calicut-673635

Chairperson-DRPC
(Signature with Date and Seal)

ASSOCIATE PROFESSOR & HEAD
Physics Department
NITK Surathkal, Mangalore-575025
KARNATAKA

ABSTRACT

Two-dimensional (2D) transition metal chalcogenides (TMCs) based photocatalysts have recently attracted significant research attention for addressing the current worldwide challenges of energy shortage and environmental pollution. This thesis is mainly focused on the design and development of visible-light-driven TMCs based photocatalytic systems that are useful for both the generation of clean energy through solar water-splitting reaction and also towards the degradation of harmful organic pollutants present in water. The influence of structure-to-photocatalytic property relationship (size and shape effects) of semiconductor nanostructures are determined by systematic modifications in the synthesis methods to obtain photocatalysts of different size and morphology and their role in enhancement of the photocatalytic activity is studied. Significant attention is paid on building heterojunctions between two semiconductors having well-aligned band structures and possessing intimately contacted interfaces that are propitious to the effective separation and transfer of photogenerated charge carriers, bringing an excellent performance. Furthermore, first-principles calculation based on density functional theory (DFT) are used to investigate the structural, electronic (band structure and density of states) and optical properties of the TMCs-based photocatalysts. Besides, band edge positions of the semiconductor and the band alignment with respect to the normal hydrogen electrode is determined theoretically. It is anticipated that this work will provide a better understanding of the fundamental photocatalytic mechanism, assisted by the development of advanced photocatalysts and studying their photocatalytic performance towards both environmental remediation and production of clean energy.

Keywords: Photocatalysis, transition metal chalcogenides, hydrogen generation, pollutant degradation

ACKNOWLEDEMENTS

CONTENTS

List of Figures

List of Tables

NOMENCLATURE

PPCPs	Pharmaceutical and Personal Care Products
Eps	Emerging Pollutants
WWTW	Waste Water Treatment Works
AOPs	Advanced Oxidation Processes
ROS	Reactive Oxygen Species
$^{\bullet}OH$	Hydroxyl
$^{\bullet}O_2^-$	Superoxide
VB	Valence Band
CB	Conduction Band
VLD	Visible-Light-Driven
2D	Two Dimensional
TMCs	Transition Metal Chalcogenides
CdS	Cadmium Sulfide
DFT	Density Functional Theroy
CBM	Conduction Band Minimum
VBM	Valence Band Minimum
NHE	Normal Hydrogen Electrode
PAW	Projector Augmented Wave
3D	Three Dimensional
ALD	Atomic Layer Deposition
1D	One Dimensional
$g\text{-}C_3N_4$	Graphitic Carbon Nitride

CdSe	Cadmium Selenide
ZnO	Zinc oxide
NaOH	Sodium hydroxide
BiOBr	Bismuth oxybromide
PXRD	Powder X-ray Diffraction
Cu	Copper
Λ	Wavelength of X-rays
FESEM	Field Emission Scanning Electron Microscopy
KeV	Kilo electron volt
EDS	Energy Dispersive Spectroscopy
TEM	Transmission Electron Microscopy
XPS	X-ray Photoelectron Spectroscopy
DRS	Diffuse Reflectance Spectroscopy
R	Reflectance
E_g	Bandgap
PL	Photoluminescence
HPLC	High Performance Liquid Chromatography
TOC	Total Organic Carbon
HER	Hydrogen Evolution Reaction
CO_2	Carbon dioxide
N_2	Nitrogen
BQ	1,4 Benzoquinone
IPA	Isopropanol
AO	Ammonium oxalate

$K_2Cr_2O_7$	Potassium dichromate
GGA	Generalized Gradient Approximation
LDA	Local Density Approximation
HSE	Heyd-Scuseria-Ernzerhof
HF	Hartree Fock
VASP	Vienna ab initio Simulation Package
PBE	Perdew-Burke-Ernzerhof
EG	Erioglaucine
VLR	Visible Light Responsive
EDA	Ethylenediamine
DI	Deionized
EIS	Electrochemical Impedance Spectroscopy
SAED	Selected Area Electron Diffraction
C_0	Initial concentration
C_t	Concentration at time t
k_{app}	Pseudo-first-order rate constant
MB	Methylene blue
Å	Angstrom
ϕ	Work function
E_F	Fermi energy
E_{vac}	Energy of stationary electron in vacuum
X	Electronegativity
E_g	Bandgap
CBO	Conduction band offset

VBO	Valence band offset
WO_3	Tungsten trioxide
MoS_2	Molybdenum disulfide

CHAPTER 1

PHOTOCATALYSIS: AN INTRODUCTION

This chapter gives a brief introduction to the major challenges of the 21st century and most pertinent way for solving the issues related to worldwide energy shortage and environmental remediation. The unique properties arising from the size confinement effects in nanostructured materials are explained followed by a discussion on the design and development of various visible-light-driven nanostructured semiconductor photocatalysts. On the basis of the first-principles calculation, the importance of the accurate positions of the band edges in the semiconductors are described. The scope of the present work and the objectives are stated in the following sections, focusing on transition metal chalcogenides-based semiconductors for environmental remediation and hydrogen generation.

Non-renewable energy resources such as coal, petroleum, and natural gas were instrumental in the industrial revolution and the technological advancements for creating easier ways for our living. However, the excessive usage of fossil fuels in the recent past is also the fundamental reason for the atmospheric pollution caused by the increased percentage of carbon dioxide in our environment leading to drastic climate change and global warming. On the other hand, recent statistical analysis indicates that fossil fuels are still being utilized for fulfilling more than 80% of the global energy demand without which there would be a serious energy crisis. Therefore, the largest technological and scientific challenge of this century is to find ways to replace the usage of fossil fuels with non-polluting sustainable energy resources.

Towards this end, it is well known that water and sunlight are the most promising renewable sources of energy. Their conversion to hydrogen is an ideal solution to counter the depletion and environmental issues related to fossil fuels. Photon-assisted splitting of water into hydrogen and oxygen using semiconductors as catalysts is an effective method for converting solar energy into clean and renewable hydrogen fuel. In addition to the production of clean energy, environmental remediation is another important challenge of the 21st century. According to a study (Parsons 2004), it was found that 11% of the total dyes produced (about 4,50,000 tonnes) are lost as effluents. Although the pigments and dyes are useful in many applications, their carcinogenic nature and high chemical stability (hindering bio-degradation) pose a serious threat to our environment. Furthermore, the usage of pesticides, detergents, pharmaceutical, and personal care products (PPCPs) in recent years has grown manifold. These organic compounds from steroids, antibiotics, pesticides, body lotions, fragrances, sunscreens, etc. are classified as emerging pollutants (EPs) and pose a serious threat even at very low concentrations as they tend to form carcinogenic by-products during chlorination at wastewater treatment plants (Snyder et al. 2003). EPs enter the ecosystem through the wastewater effluents from sewage treatment plants, hospitals, and industries (Kinney et al. 2006). A recent study conducted (Archer et al. 2017) at waste water treatment works (WWTW) in the Gauteng Province of South Africa detected nearly 55 EPs which represented of PPCPs, human indicators, illicit drugs, and metabolites. Urban cities of India might as well be facing a similar issue and therefore removal of

pharmaceutical compounds, along with other priority pollutants is imperative. In this context, advanced oxidation processes (AOPs) are considered a highly promising water treatment technology for the removal of some special organic compounds that are not treatable by conventional techniques due to their high chemical stability and low biodegradability (Pera-Titus et al. 2004). AOPs are defined as the oxidation processes involving the generation of reactive oxygen species (ROS, hydroxyl, and superoxide radicals) in sufficient quantity to affect water purification by the destruction of targeted pollutants (Comninellis et al. 2008). Among the different AOPs, semiconductor-based photocatalysis is considered to be the most feasible way for solving the issues related to worldwide energy shortage and environmental remediation since it requires only the inexhaustible solar light as the driving force and a suitable semiconductor as a photocatalyst to conduct catalytic reactions (Chen et al. 2010). Therefore, the design and development of novel photocatalysts that can be useful for both the generation of clean energy through solar water-splitting reaction and also towards the degradation of harmful organic pollutants present in water is critically important.

1.1 Size confinement effects: Bulk to nanostructured materials

Nanotechnology deals with controlling the size of matter on the nanometer scale (10^{-9} m). By manipulation of matter at the atomic and molecular level new properties emerge which depends on the change in their size and shape (Roduner 2006). Large surface to volume ratio and the quantum confinement effect are the two fundamental factors that are responsible for the unique properties exhibited by nanostructured materials in comparison to their bulk counterparts. The quantum confinement effect is the constrained motion of the electrons in a length scale that is either comparable or smaller than the length scale characterizing the electron motion in bulk semiconducting materials (Burda et al. 2005). As the particle size decreases below the exciton Bohr radius of a particular semiconductor, the electron becomes more confined in the particle that leads to an increase in the bandgap energy. Furthermore, the valence and conduction bands (VB and CB, respectively) break into quantized energy levels as illustrated in Figure 1.1 that enables the semiconductor nanostructures to exhibit unique photo-physical properties different from their bulk counterparts (El-Sayed 2004).
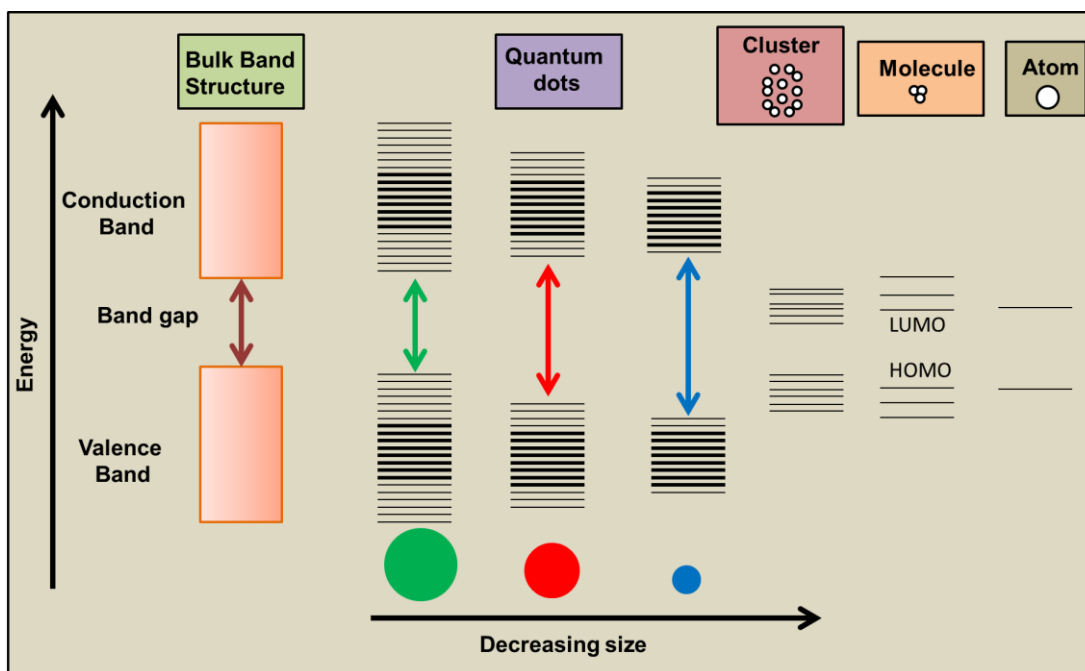
Figure 1.1: Schematic showing the splitting of energy levels due to quantum confinement effect and bandgap widening on decreasing particle size.

1.2 Design and development of visible-light-driven one-dimensionally confined transition metal chalcogenide photocatalysts

Research on semiconductor photocatalysis was initiated in 1972 by the pioneering work reported by Fujishima and Honda on TiO_2 electrodes for photoelectrochemical water splitting (Fujishima and Honda 1972). Since then, a huge number of research articles have been published on the development of highly efficient and stable semiconductor photocatalysts (Li et al. 2015b; Yu et al. 2010). However, a wide bandgap (3.2 eV) of TiO_2 limits its photoabsorption to only the UV region, which accounts for ~5% of the total solar spectrum (Hashimoto et al. 2005). Very recently, the design of visible light-responsive photocatalysts is vastly pursued by researchers for effective utilization of the solar spectrum, which comprises a large fraction of visible light (~43%) (Martin et al. 2014a; Wang et al. 2009a). In order to improve the efficiency of utilizing solar energy, an important strategy is to explore new photocatalysts with relatively narrower bandgap energy as well as higher quantum efficiency. Recently, two-dimensional (2D) semiconductor photocatalysts with their high surface-to-volume ratio and unprecedented electronic and optical characteristics have triggered a renaissance of

interest in the field of energy and environmental remediation applications (Bai et al. 2015; Deng et al. 2016). Among a large array of photocatalysts, research on transition metal chalcogenides (TMCs) has been flourishing in recent years. In this regard, this thesis majorly concentrates on the development of novel visible-light-driven (VLD) photocatalysts using 2D nanostructures such as transition metal chalcogenides (as the basic entity) by hybridization with other semiconductors for controlling their photo-physical parameters (like surface area, bandgap energy, etc.) and the recombination of photogenerated electron-hole pairs (Z-scheme model).

Earth-abundant transition metal chalcogenides (TMCs) are the semiconductors of the type MX, where M = Cd, Mo, W, etc. are transition metal atoms and X = S, Se, Te, are chalcogens. The intralayer M-X bonds are predominantly covalent in nature and the interlayers (sandwich layers) are coupled by weak van der Waals forces, allowing the crystal to readily cleave along the layer surface. The 2D morphology and ultrathin thickness of the TMCs feature an unusual physical, chemical and electronic properties compared to their bulk counterparts and therefore hold great promise for a variety of applications (Wang et al. 2012a). From the perspective of photocatalysis, they can be used as effective support for anchoring semiconductor nanoparticles, which could enhance mobility and provide active sites that are beneficial for increasing the activity of the photocatalyst (Zhang et al. 2014b). As the advanced novel nanostructured materials, cadmium sulfide (CdS) has manifested as an attractive semiconductor over the past decade because of its appropriate band positions, broader absorption in the visible light region, and promising photocatalytic activity under solar light (Sharma et al. 2021; Yuan et al. 2018). Herein, we have considered CdS-based photocatalysts as a basic entity and provided a panorama of their various physical, chemical, optical properties and moreover explained the photocatalytic mechanism involved in the degradation of organic pollutants and towards hydrogen generation.

1.3 Insights from first-principles calculations based on density functional theory

From the theoretical perspective, a semiconductor must possess a bandgap of 1.23 eV and the redox potentials of water must lie between the bandgap of photocatalysts. In particular, as shown in Figure 1.2, the conduction band minimum (CBM) must be more

negative than the reduction potential and the valence band maximum (VBM) must be more positive than the oxidation potential in normal hydrogen electrode (NHE) scale. Therefore, the knowledge of a semiconductor's VBM and CBM positions relative to the redox potentials is important for the design and development of various photocatalysts.
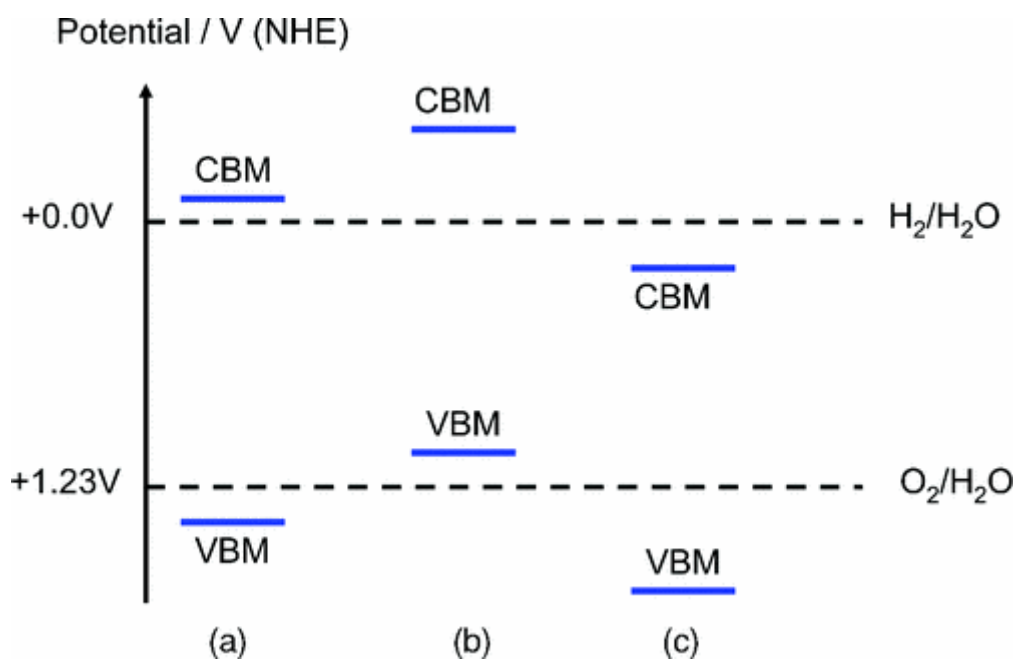
Figure 1.2: A schematic diagram of possible band level arrangements for water-splitting photocatalysts. (a) favorable band level arrangement; (b) unfavorable VBM position; (c) unfavorable CBM position.

Detailed *ab initio* studies of materials to obtain such band edge positions is important as it can be used as a scalable approach to investigate a large number of possible photocatalysts. To understand and design new photocatalyst materials, it is important to know their electronic structure. First-principles calculations allow researchers to explore the nature and origin of the structural, optical, and electronic properties of the photocatalyst materials. This approach makes use of quantum mechanics as the only basis to calculate electronic states from the atomic species and their positions, without relying on empirical parameters determined by experiment. Most of the first-principles studies on photocatalysis generally make use of the density functional theory (DFT) approach to interpret the electron density. The combination of DFT with projector

augmented wave (PAW) method using pseudopotential is the most widely used first-principles approach for electronic and optical properties calculations. Hence, computational simulation and design play a great role to assist experimental efforts in screening or identifying new potential photocatalysts.

1.4 The scope of the thesis

In order to meet the increasing energy demand in the near future we will be forced to seek environmentally clean alternative energy sources. Semiconductor-mediated photocatalysis has attracted world-wide attention for its potential in environmental and energy related applications. Although there has been much evolution in the basic research on the development of VLD photocatalysts for hydrogen evolution and photocatalytic degradation of organic pollutants, their industrial applications are rather scarce. Currently, it is still a challenge to design novel photocatalysts from abundantly available precursors that are stable and facile in fabrication besides exhibiting higher performance under visible light.

Novel synthesis methods: Numerous studies have reported the preparation of CdS nanostructures using various methods comprising of solution-based strategy, template-free technique, sonochemical technique, chemical bath deposition, and impregnation strategy (Kumar et al. 2020). For instance, CdS nanosheets of tunable thickness were synthesized by simple and low-cost oil bath method by adjusting the amount of sodium citrate in the reaction. These ultrathin sheets shortened the charge transport distance, boosted the surface-active site density, and provided sufficiently negative conduction band edge in CdS (Bie et al. 2018). In another study, CdS monodisperse spheres were synthesized in the sub-micron range using a simple hydrothermal method with cadmium acetate dehydrate and thiourea as primary precursors (Al Balushi et al. 2018). The synthesized CdS microspheres showed good performance towards the degradation of levofloxacin and acetaminophen under visible light irradiation. Literature reports suggest that photocatalytic activity of CdS is highly dependent on its morphology, crystal structure, crystallinity and particle size. These factors directly influence the bandgap and electron transfer processes, including charge separation, transport of the photogenerated carriers, and photochemical reactions. However, literature survey

7

indicated that morphology-to-photocatalytic activity relationship on CdS has been seldom reported. Therefore, the Chapter 3 of the thesis reports the photocatalytic activity of solvothermally synthesized 1D, 2D and 3D CdS photocatalysts obtained by adjusting the sulphur source and solvent.

Suppressing electron-hole pair recombination/Increase the lifetime: The higher lifetime of the photogenerated charge carriers is important in preventing their recombination. Therefore, strategic planning and execution are needed to minimize the recombination of photogenerated electron-hole pairs in the next generation photocatalysts such that they are transferred to the respective active surface sites and instantaneously get converted to radicals for enhanced photocatalytic activity. In this regard, building heterojunctions between two or more semiconductors having well-aligned band structures and possessing intimately contacted interfaces are propitious to the effective separation and transfer of photogenerated charges, bringing an excellent performance. On the other hand, coupling of p-type and n-type semiconductors are also believed to be helpful as an internal electric field is developed to redistribute the electrons and holes on the opposite sides of the junction that restricts their recombination and prolongs their lifetime resulting in an exceptionally high photocatalytic capability. As previously mentioned, CdS is a promising photocatalyst due to its excellent semiconductor properties and visible light absorption efficiency. Unfortunately, it has inevitable disadvantage and would easily suffer from photocorrosion from the self-oxidization of S^{2-} by the photogenerated holes in the valence band. On the other hand, the rate of recombination of electron-hole pairs in g-C_3N_4 has been reported to hinder its photocatalytic efficiency. Hence, the investigation for observing the improved photocatalytic activity of a heterojunction photocatalyst by coupling CdS and g-C_3N_4 is presented in Chapter 4.

Larger surface area: The photocatalytic efficiency of the catalysts is relatively low and still far from the level required for real applications owing to the smaller surface area. Therefore, it is very important to bring about modifications in the synthesis techniques for improving the porosity and obtain larger surface area photocatalysts. Semiconductor photocatalysts with larger specific areas provide ample access for the target pollutants to get adsorbed on their surface and exhibit an enhanced rate of

photodegradation. Thus, synthesizing larger surface area photocatalysts that could prove beneficial for promoting better performance is essential. For example, 3D hierarchical CdS mesoporous nanosheets were prepared via the facile hydrothermal method in the presence of soulcarboxymthyi chitosan. Owing to the large specific surface area of 3D CdS, the number of photocatalytic reaction sites increased thereby promoting the efficient electron-hole separation and hence showed excellent photocatalytic performance for the degradation of methyl orange dye molecules under visible light illumination (Wei et al. 2014).

Improving the visible light absorption efficiency: It is well-known that 40% of the solar photons are in the visible region and an efficient photocatalyst is expected to have the ability to absorb light in the visible region of the spectrum. Bandgap engineering is a promising technique to enhance the visible light absorption capacity of the semiconductors that can be achieved through doping with metals/non-metals, coupling with other semiconductors, or through morphological manipulations. Therefore, TMCs were chosen as narrow bandgap semiconductors that could act as potential sensitizers for enabling wide bandgap semiconductors to work under visible light. For instance, WO_3 is a widely investigated photocatalyst, but narrow visible light absorption range and the rapid recombination of photogenerated electron-hole pairs hinder its practical applicability. On the other hand, MoS_2 exhibits fascinating optical and electronic properties, which makes it an ideal photosensitizer. Therefore, the mechanism responsible for the enhanced photocatalytic activity of MoS_2/WO_3 heterojunction photocatalyst is presented in Chapter 6.

Excellent stability: The stability of the photocatalyst material during the photocatalytic reaction is an important parameter that needs to be studied such that the photocatalyst can be recycled and reused. For example, ZnO is an important II-IV compound semiconductor photocatalyst used for both the generation of clean energy and the degradation of organic pollutants in water. Although, the bandgap energies of ZnO and TiO_2 are similar, the former exhibits better photocatalytic activity than commercially available TiO_2 nanoparticles. However, in comparison to highly stable TiO_2, ZnO suffers from photocorrosion wherein the photogenerated holes destroy its structure during photocatalysis. In a recent study, a chemically stable TiO_2 shell layer was coated

on pre-synthesized ZnO nanoparticles by a particle atomic layer deposition technique in a specialized rotary reactor for enhancing the photostability of ZnO against photocorrosion (Sridharan et al. 2015b). Similarly, despite various advantages of CdS, the structural instability arising from the oxidation of sulphur prior to the reaction with the photogenerated holes leads to photocorrosion. Therefore, protecting the surface of CdS during the redox reactions is critical. Experimental studies conducted for testing and improving the photocorrosion stability of CdS nanostructures are discussed in Chapter 3.

Shape and size effects on the photocatalytic activity of semiconductor nanostructures: Controlling the size and morphology of the nanostructured materials by varying the reaction parameters such as concentration of precursors, time and temperature can influence the photocatalytic performance since size and shape effects play a determinant role in varying their physical and chemical properties. Towards this end, it is worthwhile to perform systematic modifications in the synthesis methods to obtain photocatalysts of different size and morphology and study their role in enhancement of the photocatalytic activity. Vaquero and co-workers discovered that solvents used in the solvothermal synthesis play an important role in the growth, structure and crystallinity of CdS (Vaquero et al. 2017). CdS with the highest crystallinity and surface area in the form of 1D nanorods were obtained using ethylenediamine as solvent. These 1D nanostructures exhibited enhanced photocatalytic activity in comparison to 2D nanosheets (obtained using diethylenetriamine solvent) and 3D microspheres (obtained using ethanol solvent), as the width of the 1D nanorods lying in close proximity to the exciton Bohr radius facilitated the delocalization of the charge carriers (electrons and holes) along their length, thereby reducing the recombination rate. Based on the literature surveyed, the effort was to design a new class of robust photocatalysts with an extended light absorption range for efficient carrier generation, accelerated charge separation and transportation, capable of strengthening the overall photocatalytic performance. Further, studying the structure-to-property relationship is interesting for understanding how structure/morphology changes can positively/negatively affect the photocatalytic

activity. Therefore, in chapter 3 we have presented the photocatalytic activity of CdS nanostructures of varying morphologies.

Theoretical approach: Generally, the features such as morphological architecture, the choice of semiconductor materials, and surface properties are considered when designing stable and efficient photocatalyst materials. From a theoretical perspective, the optical, electronic, and structural properties of the material have to be carefully investigated. Hence, to design more efficient semiconductor photocatalysts, first-principles approaches have been a useful tool in providing a deeper understanding of photocatalysis, explaining experimental data as well as predicting novel semiconductor photocatalyst materials with superior performance. Therefore, in-depth knowledge of the fundamental mechanism and understanding of the interfacial electron transfer process is useful to aid an experimentalist to design and fabricate novel photocatalysts to expand their applicability. For instance, the carrier separation, as well as the restrained recombination of electron-hole pairs in g-C_3N_4/CdS (110) interface calculated on the basis of hybrid density functional theory approach, proved that the heterojunction exhibited higher quantum efficiency under simulated visible light than the individual counterparts (Liu 2015). In another study, DFT calculations were carried out for predicting the structures of CdS monolayer sheets. Planar, distorted and buckled monolayer sheets of CdS were studied and found to be thermodynamically stable. Band edges were aligned with respect to water oxidation and reduction potentials and bandgap energy of these layers were determined (Garg et al. 2016). Thus, the proposed state-of-the-art theoretical calculations are promising towards the design of new photocatalysts for applications in photocatalysis and other electronic and optoelectronic devices. For instance, there are experimental reports in literature for CdS/CdSe heterojunction explaining their photocatalytic performance towards hydrogen evolution reaction. However, the mechanism of photocatalysis enhancement in CdS/CdSe heterojunction remains unclear, because the electronic properties of the CdS/CdSe heterojunction have not been fully investigated, including the band structure, charge transfer, and interface interaction employing density functional theory. Therefore, first principles calculations were employed to understand the mechanism of enhanced photocatalytic activity on the CdS/CdSe heterojunction.

1.5 Objectives of the thesis

- Synthesis of graphitic carbon nitride (g-C_3N_4) and transition metal chalcogenides (TMCs) based nanocomposites for photocatalytic splitting of water and photodegradation of organic dyes.

- Theoretical understanding of bandgap engineering of semiconductor nanostructures by the formation of heterojunctions and studying their photocatalytic activity.

- To study and analyze the structure-to-photocatalytic property relationship (size and shape effects) of semiconductor nanostructures.

1.6 Outline of the thesis

The present thesis comprises seven chapters, and each chapter is summarized below.

Chapter–1 already provided a brief introduction to the major challenges of the 21st century and most pertinent way for solving the issues related to worldwide energy shortage and environmental remediation. The unique properties arising from the size confinement effects in nanostructured materials are explained followed by a discussion on the design and development of various visible-light-driven nanostructured semiconductor photocatalysts. On the basis of the first-principles calculation, the importance of the accurate positions of the band edges in the semiconductors are described. The scope of the present work and the objectives are stated in the following sections, focusing on transition metal chalcogenides-based semiconductors for environmental remediation and hydrogen generation.

Chapter–2 describes experimental methods used for the synthesis of photocatalysts and the various characterization techniques for analyzing their properties. It also includes a detailed explanation of the computational methodology.

Chapter–3 explains the preparation of CdS nanostructures with 1D, 2D, and 3D morphology. The visible-light-driven photocatalytic activity of the as-prepared CdS photocatalysts was evaluated through the photocatalytic degradation of erioglaucine

molecules and towards hydrogen generation.

Chapter–4 describes the formation of g-C_3N_4-CdS heterojunction and their photocatalytic performance towards methylene blue degradation. The mechanism for the enhanced photocatalytic activity in the composite after the formation of heterojunction is discussed based on the results of charge separation and charge mobility that were tracked through photoluminescence spectroscopy.

Chapter–5 provides a theoretical understanding of the relationship of the interface and enhanced photocatalytic activity of CdS/CdSe heterostructures. The energy band structure and charge transfer at the heterojunction are systematically studied through the hybrid density functional theory approach. The valence and conduction band edge positions of the semiconductors were determined and the type of heterojunction formed based on the band alignment was discussed.

Chapter-6 is a combination of various experimental results and first-principles calculations with a new and interesting discussion to explain the photocatalytic activity of MoS_2/WO_3 heterojunction.

Chapter-7 summarizes the main results of the investigation presented in the thesis. Future work is also suggested.

CHAPTER 2

EXPERIMENTAL AND THEORETICAL METHODOLOGY AND CHARACTERIZATION TECHNIQUES

This chapter describes experimental methods used for the synthesis of photocatalysts and the various characterization techniques for analyzing their properties. It also includes a detailed explanation of the computational methodology.

2.1 Experimental methods

2.1.1 Pyrolysis: synthesis of graphitic carbon nitride

Pyrolysis (also known as thermolysis) involves the thermal deterioration of materials at higher temperatures without oxygen (case-explicit), including the concurrent change of chemical configuration and physical phase. Graphitic carbon nitride (g-C_3N_4) is typically synthesized through a pyrolysis approach. 10 g of melamine taken in a closed silica crucible is placed in a muffle furnace is ramped at a rate of 6 ^{o}C/min, and maintained at 550 ^{o}C for 2 h. After the pyrolysis reaction, the crucible is allowed to cool down naturally and the obtained lemon-yellow colored powders are crushed using mortar and pestle. The as-obtained powders are used as-is for further studies.

2.1.2 Hydrothermal/Solvothermal method: synthesis of cadmium sulfide

Hydrothermal/Solvothermal are liquid phase methods that involve a wet chemistry course that delivers sensible control over the growth by using ligands that act as growth confining agents. This strategy has exact control over the particle size, shape, and crystallinity. This technique exploits the solubility of practically all inorganic substances in water at higher temperatures and pressure and ensuing crystallization of the dissolved material from the fluid. The solvent isn't restricted to water however includes additionally other polar or nonpolar solvents like ethylene glycol, benzene, and so on and the process is called solvothermal synthesis in different solvents. A variety of nanostructured materials can be synthesized through the hydro/solvothermal method. In a typical process for the synthesis of CdS, cadmium nitrate and thiourea were dispersed in ethylene glycol. The well-mixed solution was immersed in a Teflon-lined stainless-steel autoclave and treated at 180 ^{o}C for 24 h. The resultant precipitates were collected by centrifugation and washed with DI water and ethanol several times. Lastly, the precipitates were dried at 100 ^{o}C overnight (Babu et al. 2020).

2.2 Characterization techniques

2.2.1 Powder X-ray Diffraction

Powder X-ray Diffraction (PXRD) is a non-destructive tool for the identification of crystal structure, phase and lattice constants of the powdered samples. X-ray beam of Cu-Kα radiation (1.54 Å) is incident over the sample and is diffracted by the crystalline phases in the particular direction according to Bragg's law: $2d\sin\theta = n\lambda$, where d is the spacing between the atomic planes in the crystalline phase and λ is the wavelength of x-rays. The intensity of the diffracted beam is measured as a function of the diffraction angle 2θ (Warren and Diffraction 1969). The crystalline phases of the samples can be identified by scanning in the range $2\theta = 5$-90° at a scan rate of 5 ^{o}/min and by indexing the obtained PXRD patterns.

2.2.2 Field Emission Scanning Electron Microscopy

Field Emission Scanning Electron Microscopy (FESEM) is an important tool for the investigation of morphological and surface characteristics of the samples. Electron beam having energy going from a few hundred eV to 50 KeV is rastered over the surface of the specimen by deflection coils. When the electrons strike the surface of the samples and penetrate them, the number of interactions happen that bring about the discharge of electrons and photons, and consequently, SEM images are produced by collecting the emitted electrons on the cathode ray tube. SEM can also provide the chemical composition of the samples near the surface along with the topographical information through energy-dispersive X-ray spectroscopy (EDS) (Cao 2004). The morphological investigations and EDS can be performed on Field Emission Scanning Electron Microscope.

2.2.3 Transmission Electron Microscopy

Transmission Electron Microscopy (TEM) is ideally suitable for investigating the samples at a very high resolution. It is a technique whereby a beam of electrons is transmitted through an ultra-thin specimen and interacts with it as it passes through. An image is

formed through the interaction of transmitted electrons through the specimen and focuses on to an imaging device. TEM can also be used to obtain the diffraction pattern of the specimen using which it is possible to find out the size dependent changes in the lattice parameters of the sample (Williams and Carter 1996) through selected area electron diffraction (SAED) studies. Further, it can also be used to study the chemical composition through EDS and for determining the lattice spacing in the sample of interest through high-resolution transmission electron microscopy (HRTEM).

2.2.4 X-ray photoelectron spectroscopy

X-ray photoelectron spectroscopy (XPS) is a surface sensitive quantitative technique that is utilized to measure the elemental composition, electronic and chemical states of the elements that exist in the material. Surface of the sample is irradiated with X-rays (commonly Al K_α and Mg K_α) in vacuum. When an x-ray photon hits and transfers its energy to a core-level electron, it is released from its initial state with a kinetic energy subject to the incident X-ray and binding energy of the atomic orbital from which it originated. The energy and intensity of the emitted photoelectrons are investigated to identify and regulate the concentrations of the components present (Hollander and Jolly 1970).

2.2.5 UV-Visible Diffuse Reflectance Spectroscopy

The bandgap is the distinctive feature of the material that decides its application potential. Diffuse reflectance spectroscopy is a basic, however powerful tool to estimate the bandgap of the powdered samples. When the powdered sample is illuminated with light, a portion of light is reflected from the sample surface and the remaining enters the powder and diffuses. As the light of specific wavelength is absorbed by the sample, the measurement of the diffuse reflected light at different wavelengths yields a spectrum called as the diffuse reflected spectrum (Murphy 2007). Kubelka-Munk function for reflectance F(R) is given as

$$F(R) = \frac{(1-R)^2}{2R} \qquad (2.1)$$

where R is the reflectance R = $R_{sample}/R_{reference}$. For the estimation of bandgap from UV-Vis DRS data, the absorbance can be calculated using equation (2.1). A Tauc's plot with hv along x-axis and $[F(R).hv]^2$ along y-axis is plotted. The energy bandgap (E_g) of the material is estimated by extrapolating the straight line in the graph onto the energy axis.

2.2.6 Photoluminescence Spectroscopy

Photoluminescence Spectroscopy (PL) spectroscopy is a contactless, non-destructive technique for investigating the electronic structure of materials. A phenomenon involving the absorption of light and subsequent emission of light is called luminescence. On account of photoexcitation, this luminescence is called photoluminescence. Photoexcitation causes electrons inside material to move into permissible excited states. When these electrons get back to their equilibrium states, the excess energy is released and may comprise the emission of light (a radiative process) or may not (a non-radiative process). The energy of the discharged light relates to the difference in energy levels between the two-electron states involved in the transition between the excited state and the equilibrium state. PL spectrum of nanostructured semiconductor photocatalyst can reveal a lot of information about the photocatalytic activity of the respective photocatalyst. Especially for the band-band PL spectrum, the weaker the spectrum higher is the separation between the charge carriers demonstrating a higher possibility for improvement in the photocatalytic activity (Liqiang et al. 2006).

2.2.7 UV-Visible Absorbance Spectroscopy

UV-Visible spectroscopy refers to absorption or reflectance spectroscopy in UV-visible spectral regions ranging from 200-800 nm. The absorption of radiation brings about the excitation of the electrons from the ground state to a higher energy state. The energy of the absorbed light is equivalent to the energy difference between the ground state and the excited energy states. The phenomenon depends on Beer-Lambert law, which states that

when a beam of monochromatic light is passed through a solution of an absorbing substance, the rate of decrease of intensity of radiation with the thickness of the absorbing solution is proportional to the incident radiation as well as the concentration of the solution (Calloway 1997).

2.2.8 Brunauer Emmet Teller surface area studies

Adsorption is characterized as the adhesion of atoms or molecules of gas to a surface. The quantity of gas adsorbed depends on the exposed surface as well as on the temperature, gas pressure, and strength of interaction between the gas and solid. In Brunauer Emmet Teller (BET) surface area analysis, nitrogen is typically used attributable to its accessibility in extremely pure form and furthermore its strong interaction with most solids. Since the interaction between gaseous and solid phases is usually weak, the surface is cooled utilizing N_2 to acquire detectable amounts of adsorption. Known quantities of nitrogen gas are then released into the sample cell. Relative pressures less than atmospheric pressure are achieved by creating conditions of partial vacuum. After the saturation pressure, no more adsorption happens regardless of any further increase in pressure. Extremely precise and accurate pressure transducers monitor the pressure changes due to the adsorption process. Once the adsorption layers are formed, the sample is removed from the nitrogen atmosphere and heated to cause the adsorbed nitrogen to be released from the material and quantified. The collected data is showed in the form of BET isotherm, which plots the amount of gas adsorbed as a function of the relative pressure (Bae et al. 2010).

2.2.9 High Performance Liquid Chromatography

High Performance Liquid Chromatography (HPLC) is a quick, exact and cost-effective technique for the detection of organic pollutants. HPLC can assist to determine the number of pollutants in a combination, how much each pollutant is present and the purity of the sample. The HPLC process includes the injection of a small amount (10 µl) of sample into the stream of solvent (the mobile phase) that flows through the column containing a bed of packing material (the stationary phase). The sample is then carried through the column by

the continuous flow of the mobile phase which is delivered by a precise pumping system. Depending upon the solvent and the column material, some components of the mixture will flow very gradually. Ideally the components are separated by the time they arise or elute from the column end. Depending upon the affinity of the sample components towards the packing material, some components are strongly attracted to the packing material and move very slowly whereas the other components with weaker affinity move very rapidly. Thus separation is achieved. As the separated components leave the liquid chromatography column, they are sensed by an appropriate detector. The detector transmits a signal to a recorder and the separation is recognized as a chart in the form of a sequence of peaks called chromatogram. Each discrete peak signifies a particular compound (Lynch and Weiner 1979).

2.3 Photocatalytic Studies

2.3.1 Photocatalysis

In the process of photocatalysis when the semiconductor catalyst is exposed to visible light having energy greater than the bandgap of the semiconductor it undergoes photoexcitation i.e. electrons are promoted from valence band (VB) to the conduction band (CB) leaving behind a hole in the valence band. Further, CB electrons and VB holes reach to the catalyst surface where they can react with other species already present and undergo redox reactions. As the valence band holes (h^+_{vb}) possess extremely high oxidation potential, it reacts with surface bound H_2O to produce hydroxyl ($^•OH$) radicals and on the other hand conduction band electrons (e^-_{cb}) reacts with O_2 to produce superoxide anion ($O_2^{•-}$) radicals. These active species can further react with target pollutants (organic dyes) present in the waste water and degrade them (Rauf and Ashraf 2009).

2.3.2 Photocatalytic hydrogen evolution reaction

Photocatalytic water splitting utilizing semiconductor photocatalysts is the most ideal path for the conversion of solar energy into chemical fuel (H_2). The principle thought behind the process of hydrogen evolution can be briefly described as (i) generation of electron-

20

hole pairs upon absorption of photons, (ii) charge separation and migration to the catalyst surface, and (iii) reduction of H_2O by electrons to produce H_2 on the surface of the catalyst. Here, the electrons and holes act as reducing and oxidizing agents to produce H_2 and O_2 respectively. Water splitting is an uphill reaction with standard Gibbs free energy of ΔG^o = 237 kJmol^{-1} or 1.23 eV. This implies that the bandgap of the material should be more than 1.23 eV and in the case of visible light, it should be less than 3.0 eV. The band edge potentials of CB and VB play an equally important role as compared to bandgaps. The both reduction and oxidation potentials of water should lie within the bandgap of the semiconductor photocatalyst. The bottom level of CB should be more negative than the reduction potential of H^+/H_2 (0 V vs normal hydrogen electrode (NHE)), whereas the top level of VB must be more positive than the oxidation potential of O_2/H_2O (1.23 V). (Chen et al. 2010) The schematic representation for photodegradation of organic pollutants and photocatalytic water splitting is shown in the Figure 2.1.
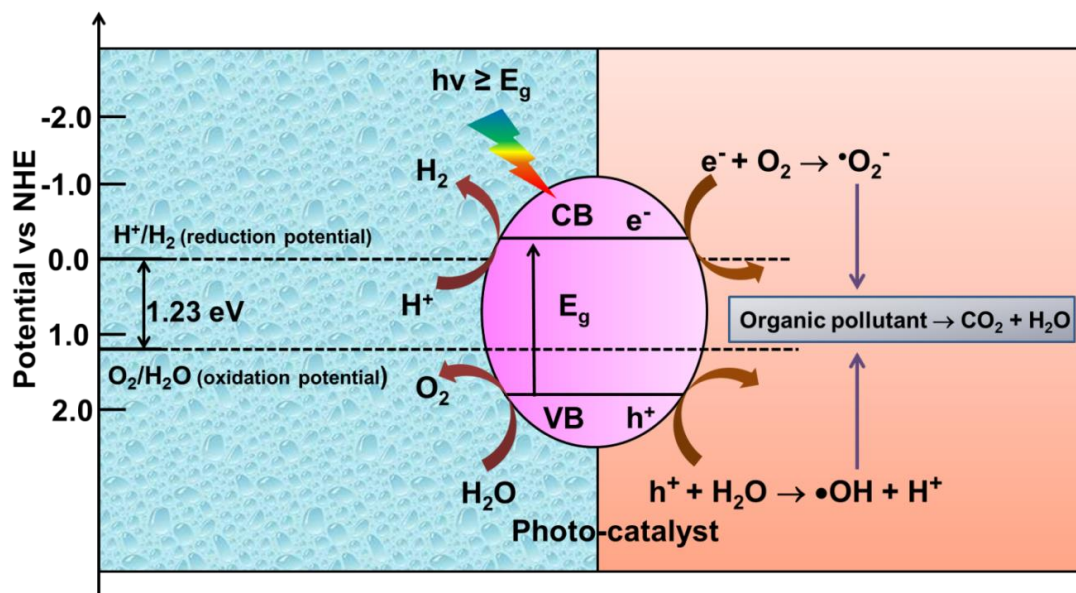
Figure 2.1: Schematic representation of photocatalytic water splitting and photodegradation by visible light driven photocatalysts

2.3.3 Visible light Photoreactor

The homemade visible light photoreactor consists of following parts:

- Mastercolour CDM-R 70 W/830 E27 PAR30L 40D 1CT Philips light (wavelength range: 400-750 nm)
- Motor-less magnetic stirrer
- Exhaust fan
- 300 ml wide crystallizing dish (Reactor) (*Duran*®)

Figure 2.2: Color photograph showing the different components of the home-made visible light photoreactor

2.3.4 Photodegradation of organic dyes

In a typical experiment, desired concentration of the photocatalyst (usually 1 g/L) is dispersed in an organic dye solution of known concentration in a reactor. It is kept in a dark place and is agitated for 30 min to ensure establishment of adsorption equilibrium between the pollutants on the catalyst surface. The solution is then placed under visible light source and the absorbance of the collected aliquots is measured at regular intervals of time using a UV-Vis spectrophotometer.

2.3.5 Photocatalytic hydrogen evolution (water splitting)

The water splitting experimentation (see Figure 2.3) is carried out by dispersing 10 mg of the certain photocatalyst in ethanol-aqueous solution (1:4 ratio) in a quartz photocatalytic cell wrapped with a rubber septum. The suspension is wisely purged with argon for 30 min and the quartz cell with dispersed sample is kept 20 cm away from the irradiating solar simulator. The generated hydrogen is measured at regular intervals of time by periodically withdrawing gas samples through the rubber septum followed by quantification using a gas chromatograph. Analyses were conducted using Agilent 7690 GC Chromatograph equipped with a thermal conductivity detector (TCD) and a 5 Å molecular sieve packed column with argon as the carrier gas. Using a gas tight syringe with a maximum volume of 50 mL, the amount of hydrogen produced was measured for 1 h intervals.
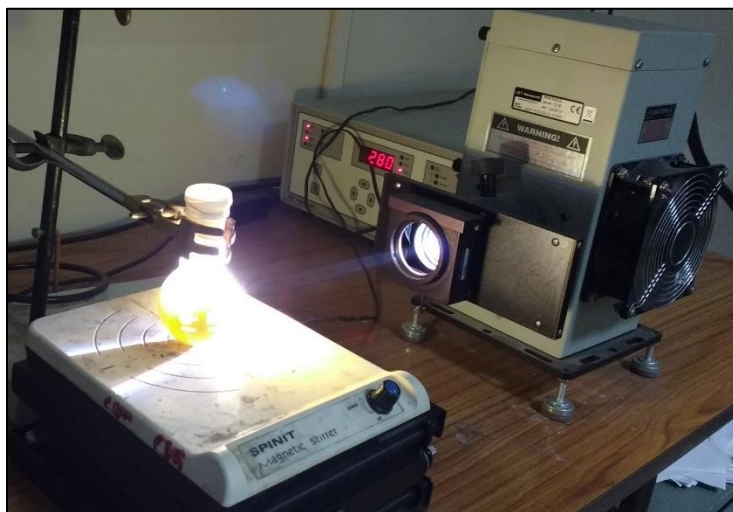
Figure 2.3: Color photograph showing the photocatalytic reactor setup for hydrogen evolution reaction

2.3.6 Role of reactive oxidative species

Radical species are the ions characterized by unpaired valence electrons. They are highly reactive in nature and have the ability to combine rapidly and non-selectively with electron

rich compounds. They have a very short life time of about nanoseconds and high oxidizing power. The detection process for reactive oxidative species is similar to the experimental photodegradation process. Various scavengers are added to the organic dye solution prior to the addition of the photocatalyst. In general, reactive species including hydroxyl radical ($^{\bullet}$OH), superoxide anion radical ($O_2^{\bullet-}$), electrons (e^-) and holes (h^+) are expected to be involved in the photocatalytic process. To investigate the role of these reactive species in the reaction, the effects of some radical scavengers can be studied as follows. Nitrogen (N_2) purging or addition of 1,4 benzoquinone (BQ) is conducted to scavenge $O_2^{\bullet-}$. Dramatic changes in the photocatalytic activity can be observed upon addition of scavengers, confirming that dissolved oxygen plays a prominent role in photodegradation process under visible light. Meanwhile similar changes can also be observed upon addition of isopropanol (IPA) or methanol as an $^{\bullet}$OH scavenger, ammonium oxalate (AO) as hole scavenger and potassium dichromate as electron scavenger.

2.4 First-principles method

Density functional theory is a computational quantum mechanical procedure used in every field to study essentially the ground state electronic structure of many-body frameworks, explicitly for crystals, and molecules. In this hypothesis, the full Hamiltonian as different components which are functions of electron density is expressed. The properties of a many-electron framework will be dictated by solving this Hamiltonian. Since electron density is a function of electron's positions, the overall energy becomes a function of another function, which is called the functionals. The utilization of functionals of the electron density leads to the name DFT. It is one of the first well-known and adaptable methods accessible in computational physical science, and chemistry (Gross and Dreizler 2013).

Kohn and Sham established the Kohn–Sham approach to account for the real systems with similar electronic density using an imaginary system of the electrons to account for the noninteracting orbitals. In   this   approach, exchange-correlation (XC) functional was

employed to account for the energy induced by the electron interaction (Kohn and Sham 1965). Among the several forms of XC functional that have been used in photocatalysis, the generalized gradient approximation (GGA) and the local density approximation (LDA) are the most common ones (Perdew and Zunger 1981). LDA strongly overestimates adsorption energies and bond strengths, while GGA functional agree well with experimental data. Moreover, both GGA and LDA fail to describe defect states and typically underestimate the bandgap of semiconductor photocatalyst materials. However, the performance of GGA and LDA functionals are generally good for structure calculation (Azadi and Kühne 2012).

To account for the bandgap underestimation, several approaches, such as the DFT + U, hybrid functionals, quasiparticle GW approximation (GWA) and other methods have been developed. The Heyd–Scuseria–Ernzerhof (HSE) hybrid functional have successfully overcome the bandgap underestimation issues by mixing the PBE functional with the Hartree–Fock (HF) wave function (Paier et al. 2006). The PBE and PW91, as well as hybrid functionals, such as HSE06 and PBE0, are the most popular for materials calculations (Hafner 2008). The HSE03 and HSE06 functionals were designed to address the expansive HF calculations, where the short-range interaction was described by the HF exchange. The percentage of HF wave function in the HSE functional is not a constant and the optimum value depends on the nature of the system (Krukau et al. 2006).

The most commonly used calculation programs for materials calculations are the Vienna *ab initio* Simulation Package (VASP). VASP is a computer program for atomic scale materials modeling for electronic structure calculations using a plane wave basis set with PAW method to describe the electron–core interaction (Kresse and Furthmüller 1996b). VASP computes an approximate solution to the many-body Schrödinger equation, with DFT to solve the Kohn–Sham equations. The basic method is DFT, however, the VASP code utilized post-DFT corrections, such as HF exchange, many-body perturbation theory, hybrid functionals and dynamical electronic correlations within the random phase approximation. VASP code is applied in phase and structure stability, dynamical and

mechanical properties, semiconductors and insulators, interfaces, surfaces, and thin films, chemical reactions as well as photocatalysis.

2.4.1 Computational methodology

Density functional theory calculation using the projector augment wave (PAW) method implemented in Vienna ab initio simulation package (VASP) to determine the accurate geometric and electronic structure of the photocatalysts (Blöchl 1994a; Kresse and Furthmüller 1996a; Perdew and Wang 1992) were employed. The generalized gradient approximation (GGA) of Perdew–Burke–Ernzerhof (PBE) scheme to describe the exchange and correlation potential, and used the empirical correction method proposed by Grimme (DFT-D3), which was proved to be a good description for long range vdW interactions, to depict vdW interaction. A very high wave function cutoff energy of 500 eV was used in each calculation to obtain accurate result. The structure relaxation was performed in each case setting the convergence criteria 1×10^{-5} eV for energy and 0.01 eVÅ^{-1} for force. Since PBE functional underestimates the bandgap due to the presence of artificial self-interaction, hybrid-DFT calculation using Heyd–Scuseria–Ernzerhof (HSE06) hybrid functional, with 25% Hartree–Fock exchange energy contribution to accurately determine the band edge positions was performed (Heyd et al. 2003).

2.5 Summary

This chapter provides a description of the various synthesis methods, characterization techniques and computational methodology reported in the thesis.

CHAPTER 3

CADMIUM SULFIDE NANOSTRUCTURES: INFLUENCE OF MORPHOLOGY ON PHOTOCATALYTIC ACTIVITY

This chapter explains the preparation of CdS nanostructures with 1D, 2D, and 3D morphology. The visible-light-driven photocatalytic activity of these as-prepared CdS photocatalysts was evaluated through the photocatalytic degradation of erioglaucine molecules and towards hydrogen generation.

3.1 Introduction

In recent years, the usage of organic dyes and pesticides has grown manifold. Erioglaucine (EG, also known as Acid blue 9, (Mol. Wt. 792.85 g/mol, $C_{37}H_{34}Na_2N_2O_9S_3$ see Figure 3.1) is one among the various other pollutants that are widely employed in textile dyeing, pharmaceuticals, and ink industries. Although EG is useful in many applications, its carcinogenic nature and high chemical stability (hindering bio-degradation) pose serious threat to our environment (Daneshvar et al. 2006). EG and other non-biodegradable organic pollutants when mixed in water at variable concentrations make the conventional physicochemical and biological processes inadequate for their effective removal (Devipriya and Yesodharan 2005), (Kabra et al. 2004). However surprisingly, almost all studies reported on the photocatalytic degradation of EG till date were conducted under ultraviolet light irradiation primarily employing titanium dioxide (TiO_2) as the photocatalyst (Daneshvar et al. 2006), (Sridharan et al. 2013a), (Sridharan and Park 2013). Though the degradation of many different organic pollutants has been reported using visible-light-responsive (VLR) TiO_2 photocatalysts, it is interesting to note that there are no reports yet on the photodegradation of EG employing any VLR photocatalyst (including VLR TiO_2) (Jank et al. 1998), (Khataee and Khataee 2008), (Khataee et al. 2009), (Caudillo-Flores et al. 2018). Cadmium sulfide (CdS) nanostructures are one among the most reported VLR semiconductor photocatalysts that are attractive towards the degradation of organic pollutants and generation of hydrogen owing to positive features such as hexagonal crystal structure, large surface area and good crystallinity (Cheng et al. 2018), (Li et al. 2015a), (Zhang et al. 2016). Furthermore, the bandgap of 2.4 eV matching well with the visible light region of the solar spectrum enables efficient absorption. Though there are many reports on the photocatalytic degradation of organic pollutants employing engineered VLR semiconductor nanostructures, to the best of the knowledge, there are no reports yet on the photocatalytic degradation of EG molecules employing any VLR photocatalyst. Further, a study on the relationship between the photocatalytic activity and the variation in the morphology of CdS nanostructures towards the photodegradation of EG is also not reported yet. In this context, for the first time the visible light driven

photocatalytic degradation of EG in the presence of 1D, 2D and 3D CdS nanostructures as photocatalysts are reported. Results indicated that the photocatalytic activity varied with respect to the change in the morphology of CdS nanostructures. Interestingly, simple sonication of the reaction slurry for 5 min before light irradiation led to a four-fold increase in the photocatalytic activity of 3D CdS in comparison to 1D and 2D CdS photocatalysts. Similarly, 3D CdS exhibited higher photocatalytic activity in the generation of hydrogen, which was significantly larger than those generated using 1D and 2D CdS photocatalysts.
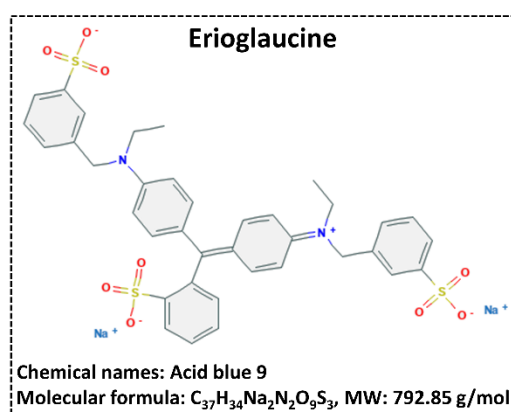
Figure 3.1: Molecular structure of erioglaucine

3.2 Experimental methods

3.2.1 Synthesis of 1D CdS

In a typical synthesis, 4 mM cadmium nitrate tetrahydrate Cd $(NO_3)_2 \cdot 4H_2O$ (AR) and 8 mM CH_4N_2S were dispersed in 100 ml ethylenediamine (EDA) solvent under constant magnetic stirring. The uniformly stirred solution was then transferred to a Teflon-lined stainless-steel autoclave of 150 ml capacity. The sealed autoclave was placed in an electric oven and the solvothermal reaction was carried out at 180 °C for 24 h. After the autoclave was cooled down naturally, the resulting yellow-colored sediments were collected and washed thoroughly with distilled (DI) water and absolute ethanol for three times. The sediments obtained were dried in an oven at 60 °C for 12 h.

3.2.2 Synthesis of 2D CdS

2D CdS nanosheets were synthesized by following a two-step procedure reported elsewhere (Zhao et al. 2014). Cadmium hydroxide ($Cd(OH)_2$) precursor was first synthesized by the drop-wise addition of 5.625 ml triethylamine to 5.625 mM $Cd(NO_3)_2 \cdot 4H_2O$ (AR) solution (225 ml DI water) under magnetic stirring. Total volume of the above solution was made to 240 ml by adding 9.375 ml of DI water after which it was transferred to two Teflon-lined stainless-steel autoclaves (150 ml capacity). The sealed autoclaves were placed in an oven at 180 °C for 24 h and the white Cd $(OH)_2$ sediments obtained after the reaction were collected, washed three times with DI water and ethanol, and then dried at 60 °C overnight. Next, for synthesizing 2D CdS nanosheets, 4 mM Cd $(OH)_2$ precursor dispersed in 120 ml of ethylene glycol under constant magnetic stirring was added with 20 mM thiourea. Stirred suspension transferred to a Teflon-lined stainless-steel autoclave was sealed and placed in an electric oven for 12 h at 200 °C. Orange-yellow colored precipitate obtained after the solvothermal reaction was washed well with ethanol before drying at 60 °C for 12 h.

3.2.3 Synthesis of 3D CdS

In a typical process, a suspension containing 4 mM Cd $(NO_3)_2 \cdot 4H_2O$ and 8 mM L-cysteine dispersed in 100 ml EDA under constant magnetic stirring was transferred to a 150 ml Teflon-lined stainless-steel autoclave. The sealed autoclave was placed in an electric oven at 180 °C for 24 h after which it was allowed to cool down before collecting the yellow precipitates. The precipitate was washed thoroughly with DI water and absolute ethanol before drying at 60 °C for 12 h.

3.2.4 Materials characterization

The crystalline nature of the obtained products was ascertained through powder X-ray diffraction (XRD) analysis and the patterns were recorded on a *Rigaku miniflex 600* X-ray diffractometer using Cu Kα radiation ($\lambda = 1.5518$ Å) in the range 2θ of $10^o - 80^o$ at a scan rate of 5° min^{-1}. The data was analyzed by matching with the JCPDS database. The

morphology of the synthesized products was analyzed by field emission scanning electron microscopy (FESEM) using a *Hitachi S-4800* microscope at an acceleration voltage of 15 kV. Low and high-resolution transmission electron microscopy (TEM) and compositional analysis was performed on a *JEOL 2010F* field emission TEM operating at an acceleration voltage of 200 kV equipped with an energy dispersive X-ray spectrometer (EDS, *Oxford INCA 30 mm ATW detector*). Samples for TEM analysis were prepared by dropping the ethanolic solution containing the dispersed product on a carbon-coated copper grid followed by solvent evaporation in vacuum. UV-visible diffuse reflectance spectra (DRS) of the solid samples were recorded on a *Varian Cary 5000* UV-visible spectrophotometer equipped with an integrating sphere calibrated using barium sulfate ($BaSO_4$) as the reference standard. A high throuput Brunauer–Emmett–Teller (BET) surface area and pore size analyzer (*Quantachrome Nova-1000*) was used for analyzing the surface area and pore size of the photocatalysts at room temperature (77 K). Photoluminescence (PL) spectra of the photocatalysts were measured using a *Fluoromax-4 TCSPC spectrophotometer (Horiba Jobin Yvon)* at an excitation wavelength of 350 nm. The electrochemical impedance spectroscopy (EIS) was carried out at the open circuit potential using an electrochemical workstation (*CHI 660D*) with 1 M Na_2SO_4, saturated Ag/AgCl and platinum wire as the electrolyte, reference electrode and counter electrode, respectively.

3.2.5 Photocatalytic degradation of erioglaucine

The photocatalytic activity of the prepared CdS nanostructured photocatalysts were assessed by observing the degradation of erioglaucine (EG) dye molecules under visible light ($\lambda > 400$ nm) irradiation. Home-made photocatalytic reactor was constructed by employing a 70W CDM-R lamp (*830 PAR30L 40D*, *Philips*, 4600 lumen) as the visible light source. Reaction slurry in crystallizing dish (*Duran®*) of 300 ml capacity was prepared by suspending 200 mg of the photocatalyst in an aqueous solution containing 200 ml EG dye (10-50 ppm). Crystallizing dish containing the slurry was placed 8 cm away from the CDM-R lamp on top of a magnetic stirrer housed inside of the home-made photoreactor and was stirred under dark condition for 30 min to ensure the adsorption of

EG dye molecules on the surface of the photocatalysts. During the photocatalytic reaction, aliquots (5 ml) of the reaction slurry were withdrawn at regular intervals of time, centrifuged for separating the photocatalyst and stored in amber glass vials. For consistency all experiments were conducted in triplicate. For determining the role of reactive species involved in the photodegradation of EG, chemicals such as potassium dichromate ($K_2Cr_2O_7$), ammonium oxalate (AO), isopropanol (IPA) and benzoquinone (BQ) were introduced as scavengers of electrons (e^-), holes (h^+), hydroxyl radicals ($^\bullet OH$) and superoxide radicals ($^\bullet O_2^-$), respectively. Reaction slurry for scavenger study experiments were prepared by adding the chemical scavengers first to the EG dye solution before the addition of the photocatalyst, while photocatalytic reaction, aliquot collection and storage was the same as aforementioned.

The rate of photocatalytic degradation of EG was determined from the absorption spectra of the centrifuged aliquots that were measured using a UV-Vis Spectrophotometer (*Ocean Optics*, SD 2000) and were compared with those of the original dye and centrifuged aliquot collected before irradiation (dark condition). Decrease in the absorbance of EG with respect to irradiation time was used to determine the efficiency of the photocatalysts that were calculated using the equation,

$$\text{Efficiency} \ (\%) = \frac{C_0 - C}{C_0} \ \text{x} \ 100 \qquad (3.1)$$

where, C_0 is the initial concentration and C is the concentration of the dye after light irradiation. Cyclic photocatalytic degradation experiments were also conducted to understand the stability of the photocatalysts. Photocatalysts recovered from the dye slurry after each photodegradation cycle through centrifugation were introduced to a fresh EG dye solution and this process was repeated for three continuous cycles. The percentage of photodegradation of EG measured through UV-Visible absorption spectroscopy was plotted against cycle number for understanding the stability of the photocatalysts.

3.2.6 Photocatalytic hydrogen generation

The photocatalytic hydrogen (H_2) evolution experiment was carried out on a suspension comprising of 20 mg of the as-synthesized CdS photocatalysts dispersed in 40 ml DI water containing 0.25 M Na_2S and 0.35 M Na_2SO_3 in a quartz round bottom flask of 50 ml capacity sealed with a rubber septum. The suspension was sonicated for 20 min and was carefully purged with argon gas for 30 min before being placed 20 cm away from the solar simulator (equipped with 300W Xenon arc lamp and AM 1.5 cut-off filter, Newport) with one sun irradiation condition. The photocatalytically generated H_2 gas was withdrawn every hour using a glass syringe and was injected into gas chromatograph (GC, Agilent 7690) for quantifying the volume.

3.3 Results and discussion

3.3.1 Morphological, chemical and structural characterization

The crystalline structure of the prepared CdS nanostructures was analyzed by X-ray diffraction. XRD patterns of 1D, 2D and 3D CdS nanostrucutres are shown in Figure 3.2 and the corresponding color images depict their physical appearance. The diffraction patterns of CdS are consistent with the hexagonal phase with lattice constants of a = b = 0.414 nm, c = 0.672 nm as reported in literature (JCPDS card # 41-1049) (Yu et al. 2014; Zhao et al. 2014). However, the relative intensity of the XRD peak corresponding to (002) plane of 3D CdS varied significantly in comparison to those of 1D and 2D CdS nanostructures, which could be attributed to the different growth tropism of the crystal, indicating the growth along the c-axis that usually lies parallel to the experimental plane during XRD measurements (Xiong et al. 2007; Xu and Zhang 2015). On the other hand, the extra peaks (at $2\theta = 30^{\circ}$, marked with # symbol) in the XRD pattern of 2D CdS corresponds to $Cd(OH)_2$, owing to the incomplete chemical transformation of $Cd(OH)_2$ into CdS (Zhao et al. 2014). Dark color of the 2D CdS in comparison to other photocatalysts (1D CdS and 3D CdS) could be owing to its larger particle size, since the longer duration

of the hydrothermal reaction at a higher temperature favors the oriented attachment growth process (Sridharan et al. 2014b).
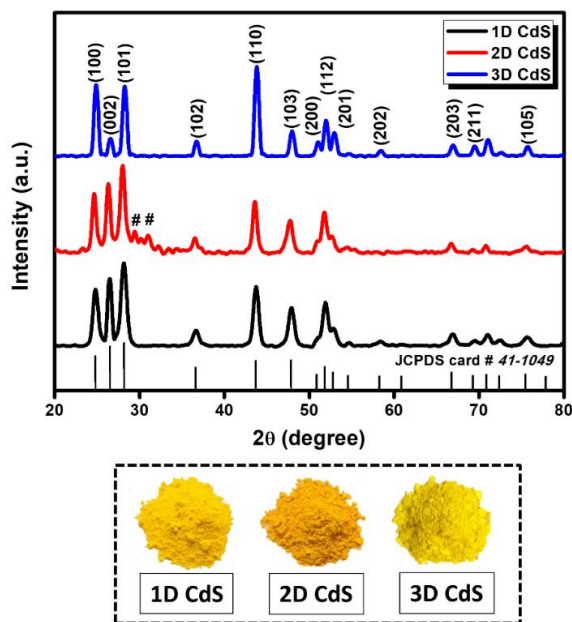
Figure 3.2: X-ray diffraction patterns of 1D CdS, 2D CdS and 3D CdS nanostructures. The color photographs seen at the bottom depicts the physical appearance of the as-synthesized CdS photocatalysts. The peak indexed with # symbol in 2D CdS correspond to Cd (OH)$_2$ precursor.

FESEM micrographs of the 1D CdS obtained at two different magnifications are displayed in Figure 3.3a and 3.3b. An overview of the uniformly assembled 1D CdS structures is evident from Figure 3.2a, while the enlarged view shown in Figure 3.3b confirm the rod-like morphology with diameters in the range of 15-30 nm and lengths between 100-400 nm. During the hydrothermal synthesis, the cadmium ions and ethylenediamine are reported to form a relatively stable symmetric bidentate ligand complex [Cd (en)$_2$]$^{2+}$ (Li et al. 1999). The slow and steady release of sulfur (S^{2-}) ions from thiourea facilitated its effective chelation with Cd^{2+} ions for the growth of 1D CdS nanorods oriented along the c-axis (Li et al. 2009). TEM analysis presented in Figure 3.3c reveal the well-defined formation of 1D CdS nanorods and are in good agreement with the FESEM observations. Typical high resolution TEM image on a piece of the nanorod shown in Figure 3.3d reveals

the lattice resolved fine structures. The nearly parallel atomic planes with a fringe spacing of 3.16 Å is in good agreement with the spacing of (101) plane of hexagonal CdS and are consistent with the XRD results. EDS spectrum shown in Figure 3.3e recorded from the boxed area marked in the dark-field TEM image (inset of Figure 3.3e) suggests that the product was essentially pure CdS.
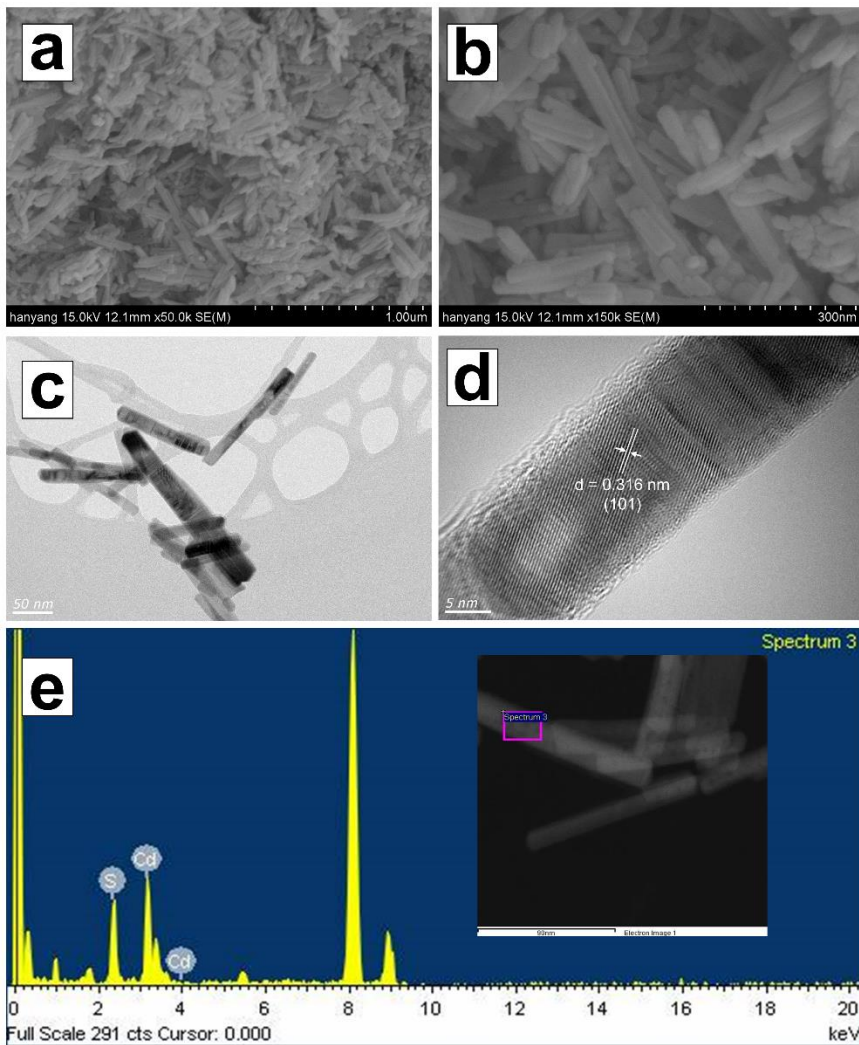
Figure 3.3: FESEM micrographs of 1D CdS nanorods at (a) lower and (b) higher magnification. (c) TEM image clearly indicating the formation of 1D CdS rod-like nanostructure, (d) lattice resolved HRTEM image revealing the fringe spacing of 3.16 Å corresponding to the (101) plane of hexagonal CdS and (e) EDS spectrum obtained by scanning the area marked on the TEM image shown in the inset.

Figure 3.4a and 3.4b represent the FESEM micrographs of the 2D CdS obtained through solvothermal method. The 2D CdS nanosheets are formed by the anion-exchange reaction between the S^{2-} anions released from thiourea and OH^- anions present in the Cd $(OH)_2$ precursor, as reported elsewhere (Zhao et al. 2014). FESEM analysis under both low and high magnifications were not able to identify the 2D sheet-like structures of CdS which could be owing to their agglomeration into particles having diameters in the range of 100-150 nm. Nonetheless, as shown in Figure 3.4c, the sheet-like morphology of 2D CdS was revealed through TEM analysis, wherein many nanosheets are found to be stacked over each other and the nearly transparent features on the edges indicates their ultrathin thickness. Lattice resolved fine structures in various areas of the high-resolution TEM image in Figure 3.4d displayed fringe spacing values of 3.56 Å, 3.16 Å and 2.05 Å, respectively corresponding to the (100), (101) and (110) planes of hexagonal CdS planes that are in good agreement with the XRD results. EDS spectrum in Figure 3.4e obtained by scanning the boxed area of the TEM image (inset of Figure 3.4e) confirms the purity of the synthesized 2D CdS.
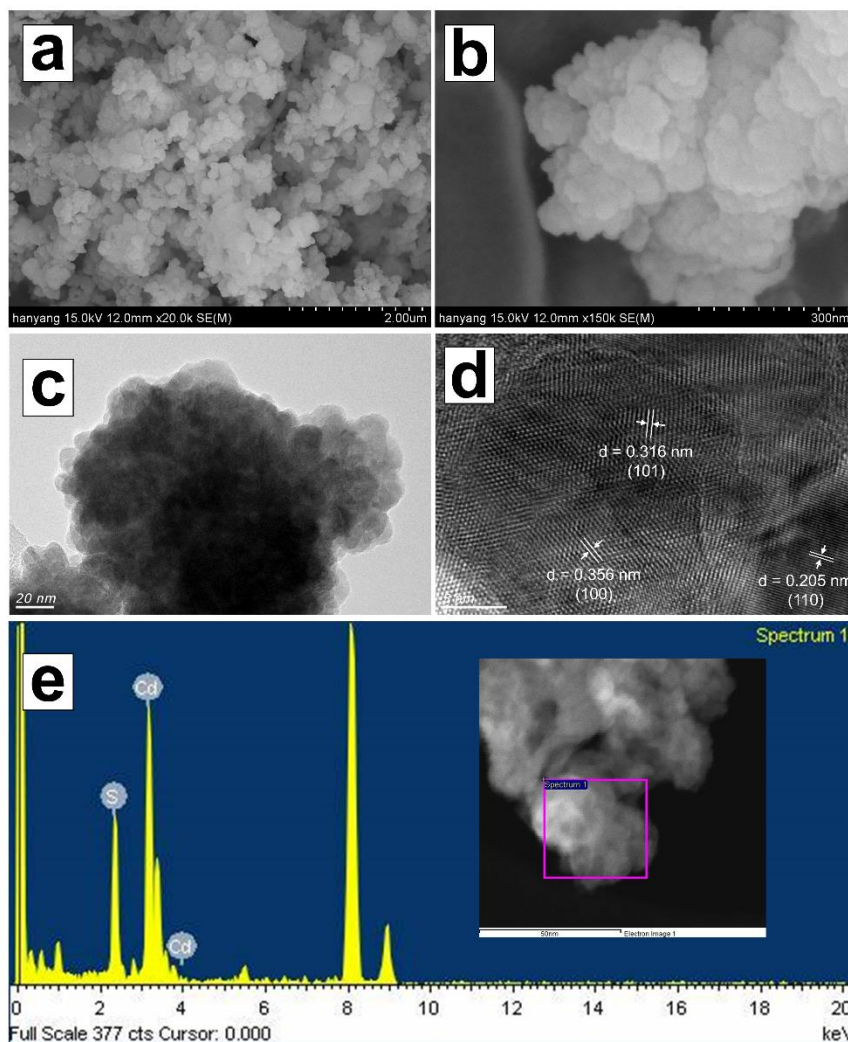
Figure 3.4: FESEM micrographs of 2D CdS at (a) lower and (b) higher magnification, (c) TEM image of 2D CdS indicating the sheet-like morphology, (d) lattice resolved high-resolution TEM image revealing the fringe spacing corresponding to various planes of hexagonal CdS and (e) EDS spectrum obtained from area marked in TEM image presented in the inset.

Low magnification FESEM micrograph presented in Figure 3.5a reveal the formation of micro-sized 3D hierarchical structures. Magnified image of a single 3D hierarchical structure shown in Figure 3.5b reveals the stacked array of 1D nanowires as subunits. Hierarchical 3D CdS nanostructures were reported to be formed through a two-step growth

37

process, wherein CdS nuclei first grew into primary 1D nanowires by the reaction between L-cysteine and cadmium nitrate in the presence of ethylenediamine. Later, these primary 1D nanowires aggregated into microspheres and resulted in the formation of 3D hierarchical CdS structures through oriented attachment growth process (Gao et al. 2012). Morphological analysis through TEM shown in Figure 3.5c clearly revealed the 1D nanowires stacked together in the form of 3D hierarchical structure. Figure 3.5c also revealed that the 1D nanowire subunits had diameters in the range of 20-40 nm and lengths between 2-4 µm. Morphology of 3D CdS with large size in range of 5-10 m measured through FESEM (Figure 3.5a) was consistent with TEM analysis (Figure 3.6a and 3.6b). Lattice resolved high-resolution TEM image in Figure 6d explicitly illustrates the nearly parallel atomic planes with fringe spacing of 3.16 Å and 2.05 Å, respectively. These fringes spacing correspond to the (101) and (110) planes of hexagonal CdS are consistent with the XRD results and indicate that the 1D nanowire subunits in the 3D hierarchical structure preferentially grow along the c-axis. Further, the appearance of spot diffraction pattern (Figure 3.11) in the selected area electron diffraction (SAED) through TEM analysis confirms the single crystalline nature of the 3D CdS photocatalysts. EDS spectrum (Figure 3.5e) with peaks corresponding to Cd and S obtained from the area marked in dark-field TEM image (inset of Figure 3.5e) confirms the purity of the as-synthesized 3D CdS photocatalysts.
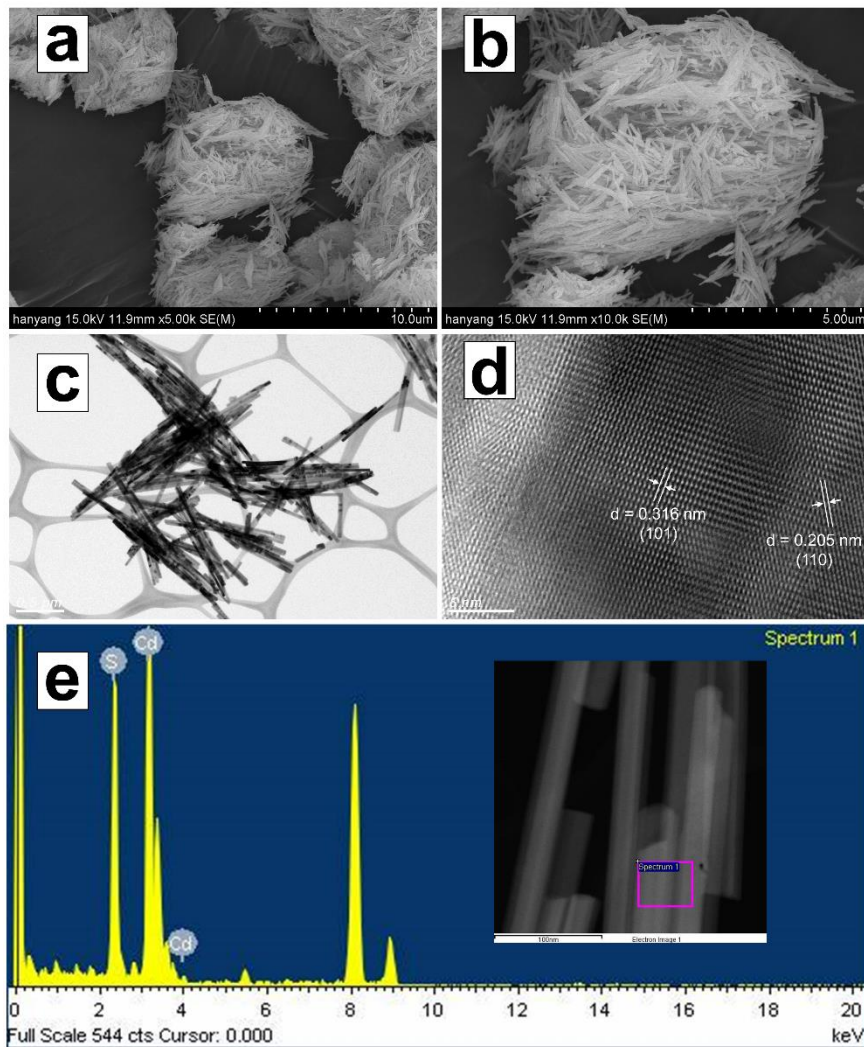
Figure 3.5: FESEM micrographs of 3D CdS at (a) lower and (b) higher magnifications clearly revealing the hierarchical 3D structure formed by uniformly stacked nanowires, (c) TEM image of the 3D CdS hierarchical structure, (d) high-resolution TEM image indicating the lattice fringes corresponding to hexagonal CdS and (e) EDS spectrum obtained by scanning the boxed area of the TEM image shown in the inset.
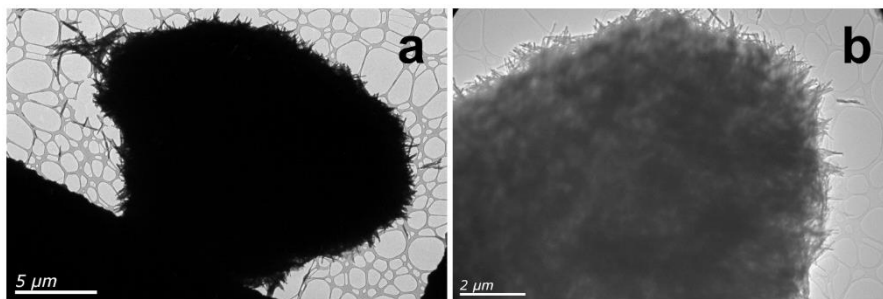
Figure 3.6: TEM image of 3D CdS at (a) very low and (b) low magnifications indicating the hierarchical 3D structure stacked with nanowires.

3.3.2 Surface area analysis, diffuse reflectance spectroscopy and photoluminescence spectroscopy

The nitrogen (N_2) adsorption-desorption isotherms and Barrett-Joyner-Halenda (BJH) pore size distribution plots analyzed through multi-point BET method for the synthesized CdS photocatalysts are shown in Figure 3.7. The values corresponding to the surface area (S_{BET}), pore volume and pore size of the photocatalysts are presented in Table 3.1. As observed from Table 3.1, the S_{BET} value of 3D CdS (20.58 m^2g^{-1}) was marginally higher in comparison to 1D CdS and 2D CdS photocatalysts. On the other hand, the pore diameter of 3D CdS (2.56 nm) photocatalyst obtained from the BJH pore size distribution plot was more than 1.5 times higher than 1D CdS and 2D CdS (1.56 nm), respectively.
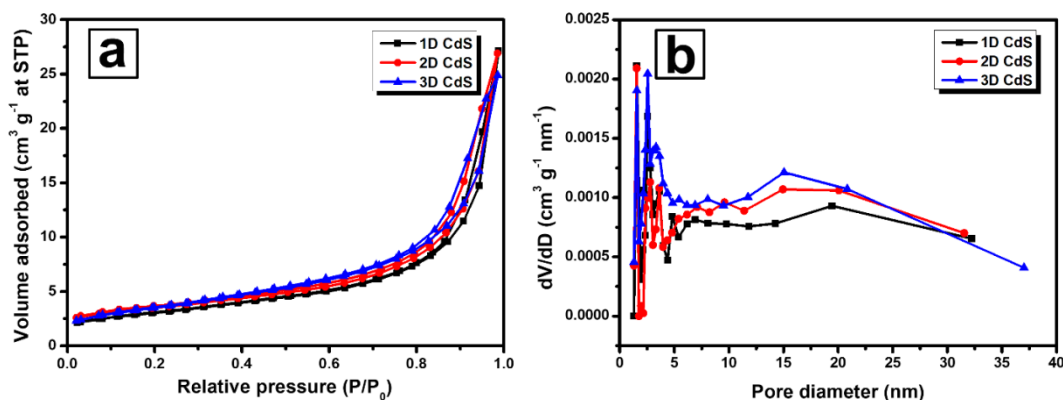
Figure 3.7: (a) N_2 adsorption-desorption isotherms of 1D CdS, 2D CdS and 3D CdS photocatalysts and (b) their corresponding pore size distribution.

Table 3.1 Energy bandgap, BET surface area, pore volume, pore diameter and rate constant values of the as-synthesized CdS photocatalysts

Photocatalyst	E_g (eV)	S_{BET} (m²g⁻¹)	Pore volume (cm³g⁻¹)	Pore diameter (nm)	k_{app} (min⁻¹)	
					With sonication	Without sonication
1D CdS	2.18	18.6	0.030	1.56	1.05×10^{-1}	2.78×10^{-1}
2D CdS	2.05	19.9	0.033	1.56	2.14×10^{-1}	1.25×10^{-1}
3D CdS	2.30	20.5	0.035	2.56	3.96×10^{-1}	3.46×10^{-1}

UV-Vis DRS is widely employed in analyzing the optical properties and bandgap energy of photocatalysts. Diffuse reflectance is related to the absorption coefficient by the Kubelka-Munk (K-M) function F(R) given by the Equation (3.2)

$$F (R) = \frac{(1-R)^2}{2R} \qquad (3.2)$$

where reflectance R = R_{sample}/$R_{reference}$ (Sridharan et al. 2013b). The UV-Vis DRS of the CdS photocatalysts are presented in Figure 3.8a, while the $[F(R)hv]^{1/2}$ versus hv plots in Figure 3.7b were used for deducing their corresponding bandgap energy by extrapolating the linear portion of the graph to $(F(R)hv)^{1/2}$ = 0. As observed from Figure 3.8a, the absorption peaks for all the CdS photocatalysts around 500 nm is consistent with that of bulk CdS. The values of the bandgap energy (Eg) deduced for the CdS photocatalysts are listed in Table 3.1, wherein the Eg value of 3D CdS (2.3 eV) was found to match well with the previous report (Yu et al. 2014). On the other hand, the decrease in the Eg value of 2D CdS to 2.05 eV could be attributed to its larger crystallite size, as evidenced from the red-shift in the absorption peak (Kumar et al. 2015), (Ahmed et al. 2016). Further, the larger crystallite size of the 2D CdS is observed from the FESEM images (Figure 3.4a, 3.4b) and

its darker physical appearance (Figure 3.2) can be attributed to the red-shift in the absorption peak leading to decrease in the Eg value.
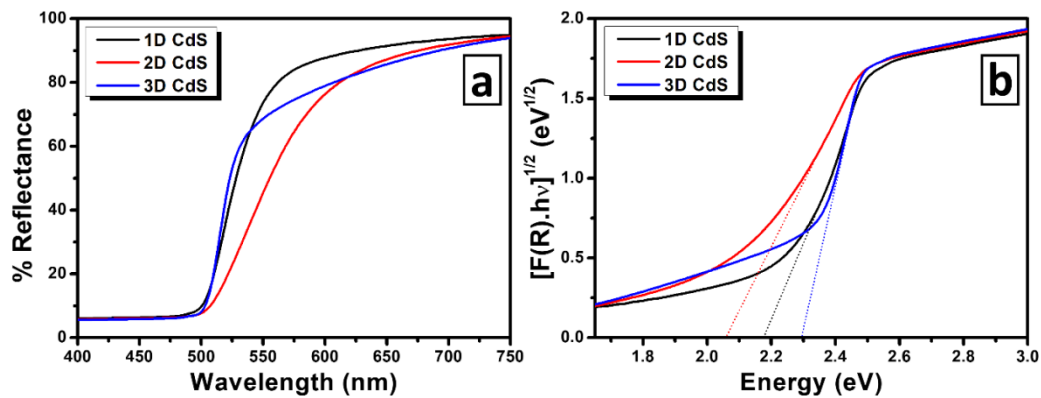
Figure 3.8: (a) UV-vis diffuse reflectance spectra of the prepared CdS (1D, 2D and 3D) photocatalysts and (b) their corresponding Tauc's plots ($[F(R)h\nu]^{1/2}$ vs hν plot). The effective bandgap of the photocatalysts is estimated from the intercept on the x-axis (extrapolated dashed lines).

Photoluminescence (PL) spectra of the synthesized CdS nanostructures were recorded for analyzing the separation efficiency of the photogenerated exciton (electron-hole pair). Generally, a lower value of intensity in the PL spectrum is indicative of the efficient separation of photogenerated excitons, while the higher intensity is attributed to their rapid recombination (Chai et al. 2018), (Sridharan et al. 2015a). CdS photocatalysts were excited at a wavelength of 350 nm and the emission recorded between 450-600 nm has been plotted in Figure 3.9. As observed from Figure 3.9, a broad emission band with a peak at ~570 nm is observed for all CdS photocatalyst. The emission intensity of 3D CdS was the lowest among the three photocatalysts and it was an order of magnitude lower in comparison to 2D CdS. This result is indicative of the lower rate of electron-hole (e-h) pair recombination and longer charge carrier lifetime in 3D CdS photocatalyst in comparison to its counterparts (1D CdS and 2D CdS) (Vaquero et al. 2017).
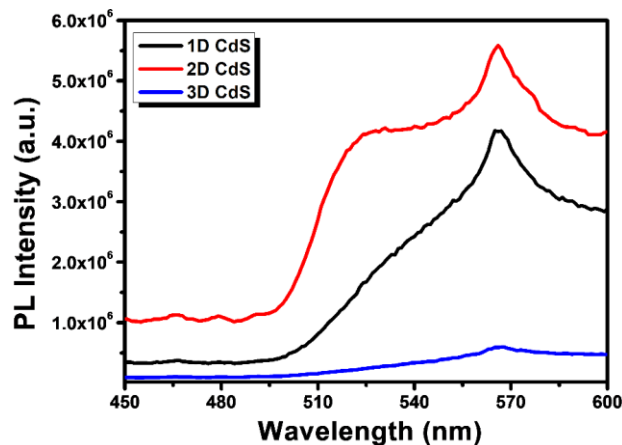
Figure 3.9: Photoluminescence spectra of the nanostructured CdS (1D, 2D and 3D) photocatalysts.

3.3.3 Visible light driven photocatalytic degradation of erioglaucine

The visible light driven photocatalytic activity of the as-prepared CdS (1D, 2D and 3D) photocatalysts were evaluated through the photocatalytic degradation of EG molecules in water. The plot showing the photocatalytic degradation of EG with respect to irradiation time is presented in Figure 3.10a. As seen in Figure 3.10a, the photodegradation of EG was negligible under visible light irradiation while no photocatalysts were added, indicating no photolysis occurred. Addition of the photocatalysts to EG under dark conditions (see Figure 3.10a) revealed its adsorption over the surface of the photocatalysts, wherein the adsorption efficiency was maximum with 36% for 1D CdS and minimum with just 5% for 2D CdS and 3D CdS. UV-Visible absorption spectra corresponding to the VLD photocatalytic degradation of EG in the presence of 1D CdS and 3D CdS are presented in Figure 3.9b and 3.9c, respectively, wherein the consistent reduction in the intensity of the characteristic absorption peak of EG dye at λ_{max} = 625 nm is indicative of the reduction in its concentration. As observed from the UV-Vis absorption spectra, the absorption peak of EG decreased to 70% of its initial value for EG in case of 1D CdS (Figure 3.10b) indicating the excellent adsorption of EG dye over the surface of the photocatalyst under dark conditions. Next, under visible light irradiation over 90% of EG was degraded (see Figure 3.10a) in 120 min, which could be attributed to the enhanced light-harvesting capability of

43

the 1D CdS nanostructures with rod-like morphology exhibiting good light absorption and scattering properties (Xiong et al. 2014). Also, the small diameter of 1D CdS nanorods is likely to enable easy migration of the photogenerated excitons to the surface-active sites towards the degradation of the pre-adsorbed species (Yu et al. 2014). On the other hand, as seen from Figure 3.10c, the adsorption of EG over 3D CdS photocatalyst under dark condition was poor by a factor of six in comparison to 1D CdS. However, 3D CdS photocatalyst surprisingly degraded over 96% of EG (see Figure 3.10a) during the same visible light irradiation time period of 120 min. The enhanced photocatalytic efficiency of 3D CdS could be attributed to its hierarchical 3D morphology containing several dozen nanowires connected to each other wherein more coordination sites on the unsaturated surface get exposed to the dye molecules thereby enabling efficient transport of the reactive species for enhanced photocatalytic activity (Xiao and Zhang 2010). Further, the enhanced photocatalytic activity of 3D CdS could be related to its single crystalline nature with higher crystallinity as evidenced from the SAED pattern (Figure 3.11), its lower emission intensity observed from the PL spectrum (Figure 3.9) indicating enhanced charge separation and its large pore diameter (Table 3.1). Photocatalytic degradation of EG in the presence of 2D CdS photocatalyst was the poorest as seen from the plot in Figure 3.10a. Poor performance of 2D CdS as a photocatalyst could be attributed to the higher degree of agglomeration of the nanosheets (see Figure 3.4b) that could have hindered the migration of the photogenerated excitons to the active surface leading to their recombination. The higher rate of recombination of the photogenerated excitons in 2D CdS is evident from its high emission intensity (Figure 3.9).
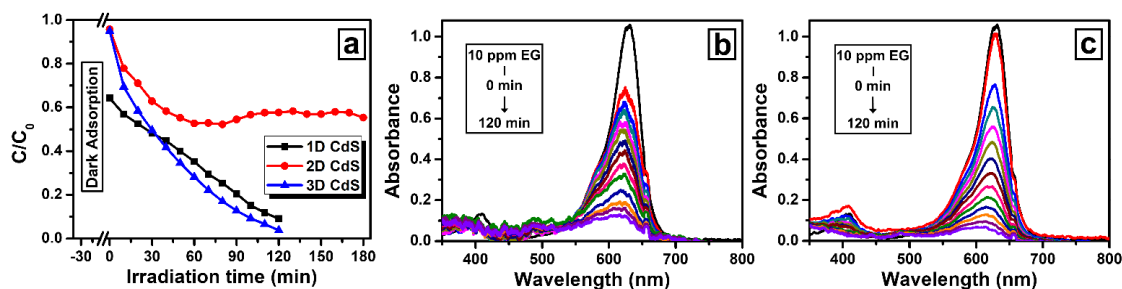
Figure 3.10: (a) Plot showing time-dependent photocatalytic degradation of 10 ppm erioglaucine under visible light irradiation in the presence of the prepared CdS nanostructures as photocatalyst. UV-Visible absorption spectra depicting the visible light induced photocatalytic degradation of erioglaucine in the presence of (b) 1D CdS and (c) 3D CdS.

Figure 3.11: Selected area electron diffraction (SAED) pattern of 3D CdS obtained through transmission electron microscopy.

An attempt was made to understand the effect of sonication on the photocatalytic activity of the photocatalyst. Sonication was carried out by placing the crystallizing dish containing the reaction slurry in an ultrasonic bath at a frequency of 100 kHz for 5 min before it was stirred for 30 min under dark condition. In comparison to sonophotocatalysis described elsewhere, (Joseph et al. 2009) herein the usage of sonication was restricted to just 5 min before the commencement of the photocatalysis reaction. Interestingly, sonication was found to have a detrimental effect on the performance of 3D CdS photocatalyst as observed

from the UV-Vis absorption spectra presented in Figure 3.12a. After sonication the adsorption of EG over the surface of 3D CdS photocatalyst increased by a factor of six and over 97% of EG was degraded within 50 min of visible light irradiation (see Figure 3.12b). Sonication therefore increased the photocatalytic efficiency of the 3D CdS photocatalyst by a factor of two. Enhanced photocatalytic activity of 3D CdS after sonication of the reaction slurry could be attributed to better adsorption of the EG molecules over the photocatalyst surface due to agitation induced dispersion and the partial split-up of the 3D hierarchical structure into 1D CdS nanowires, which in turn facilitated faster migration of the photogenerated excitons to the surface-active sites towards the degradation of the pre-adsorbed EG species. Further, the large pore diameter (2.56 nm) and the lower emission intensity (Figure 3.9) from PL spectrum of 3D CdS can be attributed to the enhanced photocatalytic activity in the degradation of EG. As observed from Figure 3.12b, the photocatalytic activity of 2D CdS after sonication increased to 98% in 180 min of light irradiation, which can obviously be accounted to the reduction in the agglomeration that led to the generation of active redox species on the exposed catalyst surface owing to the increase in the surface area per unit solution volume (Panchangam et al. 2009; Saien et al. 2010 p.). On the other hand, in comparison to 2D and 3D CdS nanostructures the photocatalytic activity of 1D CdS decreased significantly after sonication (see Figure 3.12b). Significant changes in the physical and chemical properties of 1D nanomaterials resulting from ultrasonic deformation and even fracture under the influence of sonication was reported recently (Dai et al. 2016). Herein, the drastic reduction in the rate of adsorption of EG in the zero-minute aliquot in the presence of 1D CdS (see Figure 3.12b) from 36% (without sonication) to 1.5% (with sonication) could be attributed to the ultrasonic breakdown/deformation of the nanorods. Further, the recombination of the photogenerated excitons due to their slow migration over the deformed CdS nanorod fragments could have led to the poor photocatalytic efficiency.
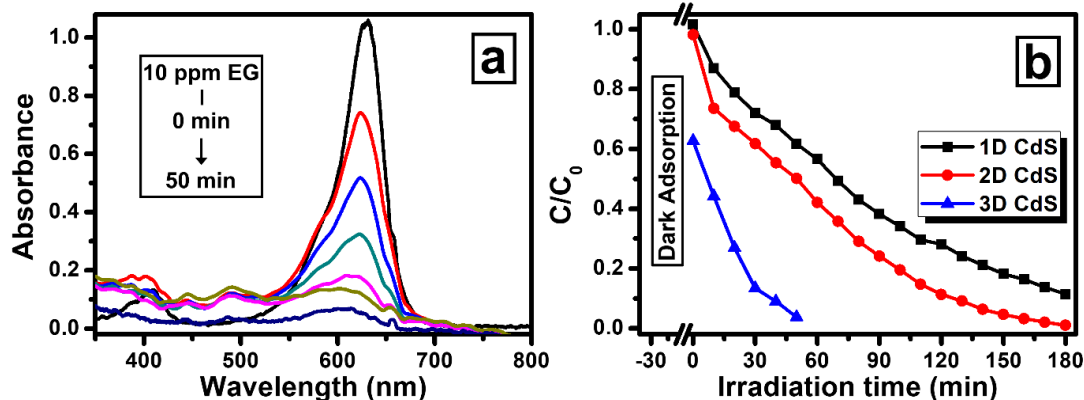
Figure 3.12: (a) UV-Vis absorption spectra showing the sonication-assisted photocatalytic degradation of 10 ppm erioglaucine under visible light in the presence of 3D CdS nanostructures as photocatalyst and (b) Plot showing time-dependent sonication-assisted photocatalytic degradation of 10 ppm erioglaucine under visible light irradiation in the presence of the prepared CdS (1D, 2D and 3D) nanostructures as photocatalyst.

For understanding the kinetics of the photocatalytic reaction, the degradation rates were computed using the pseudo-first-order kinetics given by the equation,

$$\ln (C_0/C_t) = k_{app}\, t \qquad (3.3)$$

where C_0, C_t and k_{app} correspond to the initial concentration, the concentration at time t and the apparent pseudo-first-order rate constant (k_{app}, min^{-1}), respectively (Saikia et al. 2015), (Wang et al. 2013). Plots of the pseudo-first-order reaction kinetics for the photodegradation of EG in the presence of the synthesized CdS photocatalysts with and without sonication are presented in Figure 3.13. k_{app} for the photodegradation of EG that were determined from the experimental data (represented in the inset of Figure 3.13a and 3.13b) is presented in Table 3.1. It is observed that the values of degradation efficiency for the nanostructured CdS photocatalysts are consistent with the kinetic data.

47
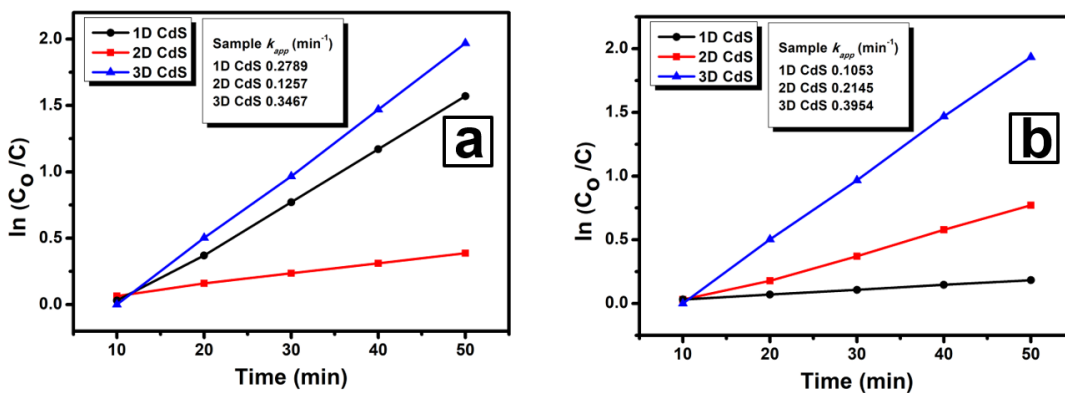
Figure 3.13: Pseudo first-order reaction kinetic plots for the photodegradation of erioglaucine in the presence of nanostructured CdS (1D, 2D and 3D) photocatalysts (a) without sonication and (b) with sonication. The apparent rate constants (k_{app}) determined from the plots are mentioned in the insets.

In order to study the photocatalytic activity of the best performing 3D CdS photocatalyst in the degradation of EG at higher concentrations, sonication-assisted photocatalysis experiments under visible light by increasing the concentration of EG from 20-50 ppm were conducted. UV-Visible absorption spectra displaying the time-dependent photocatalytic degradation of EG at various concentrations in the presence of 3D CdS as photocatalyst is presented in Figure 3.14. As observed from the results, complete photodegradation was achieved within 100 min of light irradiation in case of EG solution of 20 ppm, while all other EG solutions with higher concentrations (30, 40 and 50 ppm) were degraded within 140 min. Excellent photocatalytic activity of the 3D CdS photocatalyst can be attributed to the favorable 3D hierarchical structure, excellent crystallinity and the sonication-effect, which enable more active sites towards the generation of reactive oxygen species as discussed earlier (Chen and Smirniotis 2002). Therefore, sonication-assisted photocatalysis is an effective method towards the photocatalytic degradation of highly stable organic pollutants such as EG.
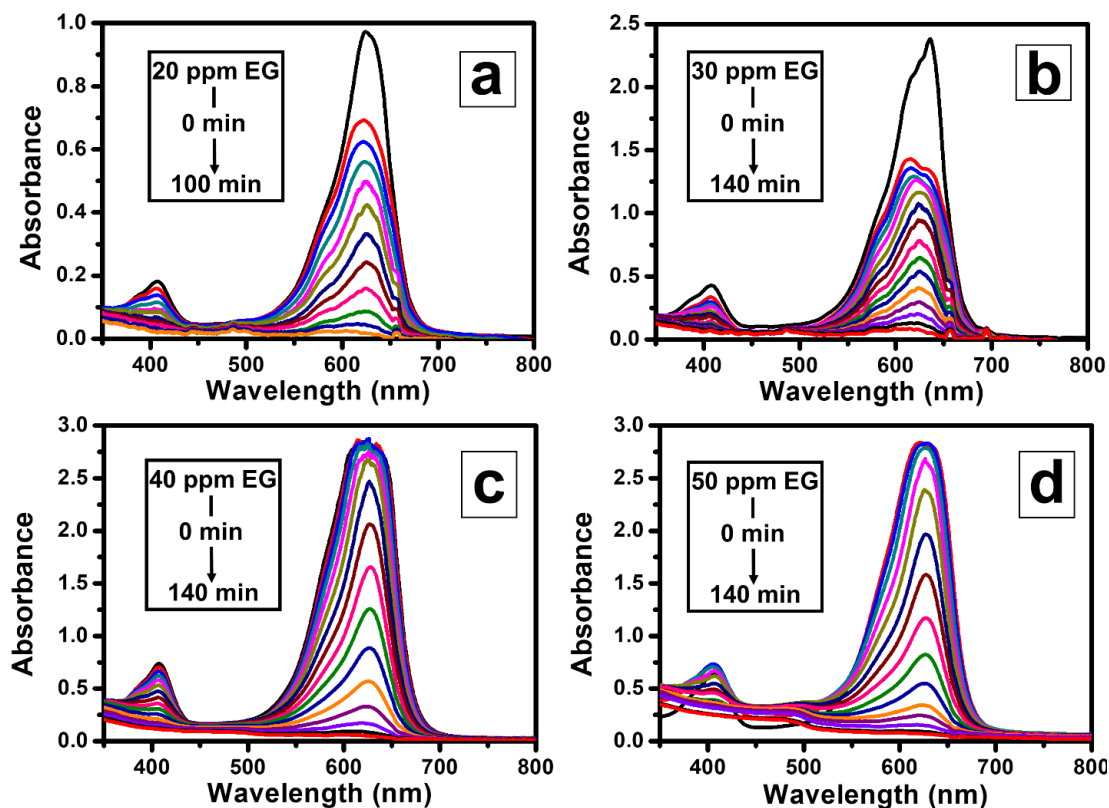
Figure 3.14: UV-Vis absorption spectra showing the time-dependent visible light driven photodegradation of erioglaucine molecules of concentration (a) 20 ppm, (b) 30 ppm, (c) 40 ppm and (d) 50 ppm in the presence of 3D CdS as the photocatalyst.

3.3.4 Charge carrier separation, role of reactive species and photocatalyst stability

Performance of a series of photocatalysts can be analyzed through EIS, wherein the photocatalyst with the lowest value of impedance at the solid-liquid interface is determined as the best (Yu et al. 2018). The results of the EIS measurements on the CdS photocatalysts are presented as Nyquist plots in Figure 3.15. As observed from Figure 3.15, 1D CdS and 2D CdS photocatalysts exhibit a large sized semicircle in the Nyquist plots that corresponds to higher impedance values. Thus, the charge-carrier transfer at the solid-liquid interface in 1D and 2D CdS photocatalysts will be poor, which leads to higher rate of recombination of the photogenerated excitons. On the other hand, the smaller size of the semicircle in the Nyquist plot of 3D CdS photocatalyst indicates a lower value of impedance. Therefore, 3D

CdS photocatalyst exhibits efficient charge transfer at the solid-liquid interface, which effectively suppresses the recombination of the photogenerated excitons (Chen et al. 2015; Zheng et al. 2015).
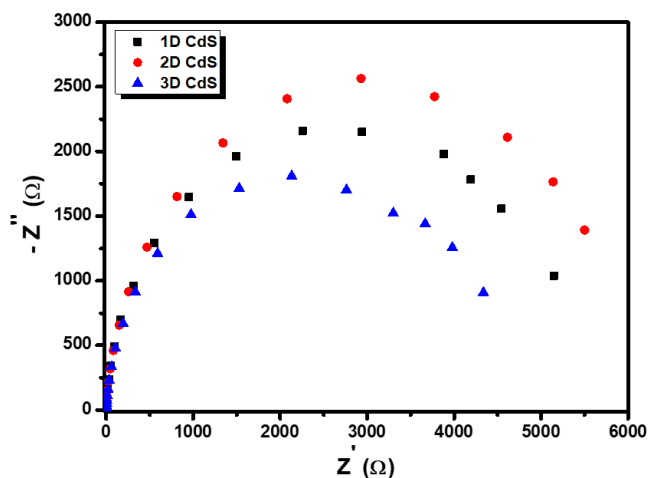
Figure 3.15: Nyquist EIS plots of the nanostructured CdS (1D, 2D and 3D) photocatalysts in 1 M aqueous solution of Na_2SO_4.

It is well known that, the activity of photocatalyst depends on the separation and transfer of photogenerated electron-hole pairs that induce the formation of hydroxyl ($^{\bullet}OH$) and superoxide ($\bullet O_2^-$) radicals, which in turn facilitates the degradation of the organic pollutants adhered onto the photocatalyst surface. For CdS, the valence band (VB) and conduction band (CB) positions are 1.78 eV and -0.42 eV, respectively (Yue et al. 2016). CdS exposed to visible light directly absorbs photons and generates electron-hole pairs. Holes (h^+) formed in VB and electrons (e^-) in CB reach CdS surface to readily react with water and dissolved oxygen molecules to produce $^{\bullet}OH$ and $^{\bullet}O_2^-$, respectively.

The reactive species (RSs) generated during the photocatalytic degradation of EG in the presence of the photocatalyst tend to play a vital role. For understanding the contribution of the RSs involved during the photodegradation of 10 ppm EG, different chemicals were employed as scavengers for quenching specific RSs. As mentioned in the experimental section, potassium dichromate ($K_2Cr_2O_7$) for e^-, ammonium oxalate (AO) for h^+, isopropanol (IPA) for $^{\bullet}OH$ and benzoquinone (BQ) for $^{\bullet}O_2^-$ were introduced as scavengers

in the reaction slurry before light irradiation. Complete sonication-assisted photodegradation of 10 ppm EG was achieved within 40 min when no scavengers were added. The plot in Figure 3.16 shows the time-dependent photocatalytic degradation of EG in the presence of scavengers. It can be observed that the e^- formed in the CB of CdS plays a very important role, as it inhibited the degradation of EG under visible light after the addition of $K_2Cr_2O_7$. On the other hand, while h^+ were scavenged with the addition of AO, there was a noticeable enhancement in the degradation, which confirmed the importance of e^- in the photocatalytic degradation of EG. Noticeable inhibition in the degradation of EG with the addition of IPA for scavenging $^\bullet OH$ radicals indicated its favorable assistance in the abatement of EG. Very high inhibition in the degradation of EG with the addition of BQ confirmed the major involvement of the $^\bullet O_2^-$ radical species. Therefore, the action of the RSs towards the photocatalytic degradation of EG from scavenger studies is in the order $^\bullet O_2^-$ radicals $> e^- > {}^\bullet OH$ radicals.
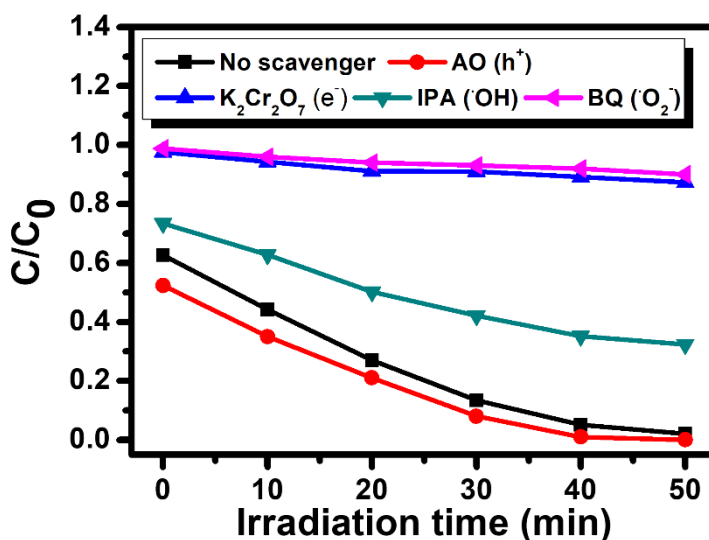
Figure 3.16: Plot showing the time-dependent visible light photocatalytic degradation of 10 ppm erioglaucine in the presence of 3D CdS as photocatalyst after the addition of various scavengers.

In addition to higher photocatalytic efficiency its stability against photocorrosion is an important factor that is usually considered for deciding its employability for industrial applications. Photocorrosion has been the inherent drawback for ZnO and CdS based photocatalysts, wherein the sulfide ion in CdS is highly prone to oxidation by the photogenerated holes (Hu et al. 2013). Further, the toxicity of the Cd^{2+} ions leached after photocorrosion is also a matter of serious concern. Therefore, for studying the effect of photocorrosion on the 3D CdS nanostructures, the photocatalytic degradation of EG were performed repeatedly for three continuous cycles by reusing the catalyst after its separation from the residual slurry through centrifugation. The results of the cyclic photodegradation of EG by consecutively recycling the 3D CdS photocatalyst is plotted in Figure 3.17. Results indicate only an insignificant loss in the photodegradation efficiency, which could be attributed to the reduction in the mass of the photocatalyst during each round of centrifugation and rinsing.
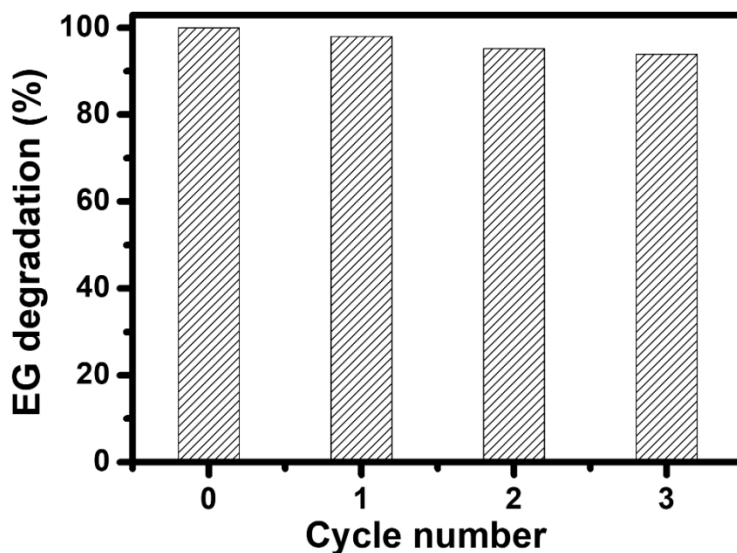
Figure 3.17: Plot showing cyclic visible light driven photodegradation of erioglaucine in the presence of 3D CdS photocatalyst.

3.3.5 Photocatalytic hydrogen evolution

Photocatalytic H_2-evolution were carried out with CdS nanostructures as photocatalysts under one sun conditions (AM1.5) in an aqueous suspension containing 0.25 M Na_2S and 0.35 M Na_2SO_3. In comparison to other conventional H_2 evolution studies reported elsewhere, (Sridharan et al. 2015a) we did not load Pt onto to the surface of the photocatalyst. Results presented in Figure 3.18 indicate that the amount of H_2 generated after 4 h of light irradiation using 3D CdS (0.767 mmolg^{-1}) was the highest, while it was disproportionately lower for both 1D CdS (0.0311 mmolg^{-1}) and 2D CdS (0.002 mmolg^{-1}). Light irradiated on a completely deoxygenated (to avoid electron scavengers) suspension containing the photocatalyst with hole scavengers (Na_2S and Na_2SO_3), facilitated the free flow of photogenerated e$^-$ that spontaneously converted the protons (H$^+$) to H_2. Further, the production of photogenerated e$^-$ in the CB of 3D CdS as one of the most important reactive species were clearly revealed through scavenger studies. Under these conditions, 3D CdS exhibited excellent photocatalytic activity in the generation of H_2 that can be attributed to its hexagonal crystal structure with high crystallinity (single crystalline nature, Figure 3.11), large pore diameter (Table 3.1), lower emission intensity (Figure 3.9) and lower value of impedance (Figure 3.15), confirms the enhanced charge separation. Also, most importantly the hierarchical structure of 3D CdS piled with many thin nanowires possessing numerous photocatalytically active sites facilitated the e$^-$ transport for reacting with water molecules adsorbed on their surface. Moreover, literature report shows that 3D CdS nanospheres synthesized by hydrothermal approach exhibit photocatalytic activities ranging from 1.2-1.4 mmolg^{-1} which are almost consistent with the values obtained in the present study (Abbood et al. 2020, Chai et al. 2018). On the other hand, the poor activity exhibited by 1D and 2D CdS photocatalyst could be owing to the weaker interaction of SO_3^{2-} ions with the CdS surface resulting in the poor hole transfer efficiency, thereby increasing the e-h pair recombination. Further, the higher intensity in the emission spectra (Figure 3.9) and higher value of impedance from EIS results (Figure 3.15) of 1D and 2D photocatalysts can be attributed to their poor performance in the photocatalytic H_2-evolution reaction (Bao et al. 2008; Low et al. 2019).
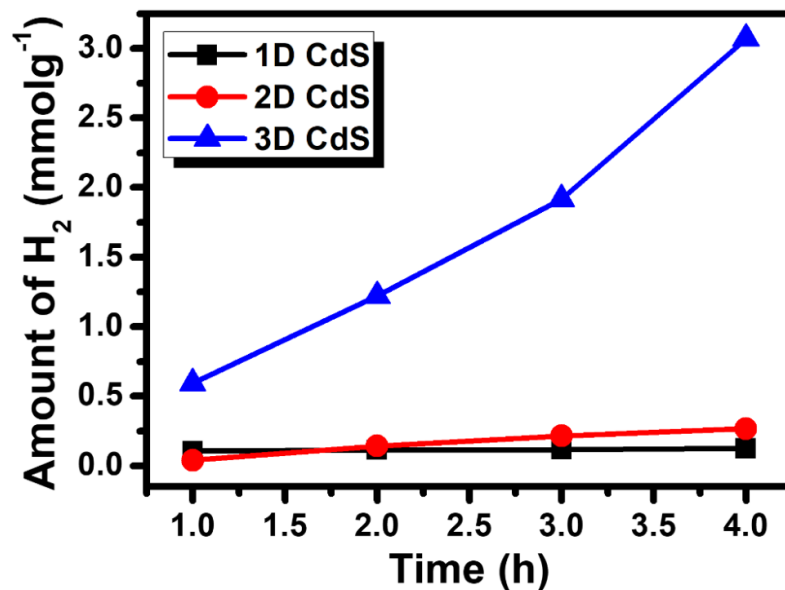
Figure 3.18: Plot showing the amount of hydrogen generated in a 0.25 M Na₂S/0.35 M Na₂SO₃ aqueous suspension in the presence of 1D, 2D and 3D CdS nanostructures under solar light irradiation (AM1.5).

3.4 Summary

In conclusion, CdS nanostructures with 1D, 2D and 3D morphology as VLR photocatalysts and verified the influence of morphology on the photocatalytic activity towards the degradation of erioglaucine and generation of hydrogen under visible light irradiation were successfully synthesized. Structure, morphology and chemical composition of the as-prepared photocatalysts analyzed using XRD, FESEM, HRTEM and EDS confirmed the formation of CdS nanostructures with different morphologies. Surface area, energy bandgap and emission intensity of the photocatalysts were measured using BET, UV–vis diffuse reflectance and photoluminescence spectroscopy for understanding the surface characteristics, energy bandgap and charge carrier characteristics. Among the synthesized photocatalysts, 3D CdS exhibited enhanced photocatalytic efficiency in the photodegradation of erioglaucine as well as for hydrogen generation. Major factors

responsible for the enhanced photocatalytic efficiency of 3D CdS were, (i) hexagonal crystal structure, (ii) high crystallinity with single crystalline nature that hindered bulk electron-hole pair recombination and (iii) hierarchical 3D structure assembled with many thin nanowires containing numerous photocatalytically active sites that facilitated the mobility of photogenerated charge carriers for the reaction with surface adsorbed molecules. Role of scavengers and cyclic photodegradation studies for understanding the stability of 3D CdS against photocorrosion were discussed. Furthermore, the surprising effect of sonication in the enhancement of the photocatalytic activity has been illustrated. Rational design of visible light active nanoscale semiconductors exhibiting unique physical and chemical properties thereby offers promising scope and widespread practical applications in environmental remediation and solar fuel production.

CHAPTER 4

CADMIUM SULFIDE-GRAPHITIC CARBON NITRIDE COMPOSITE PHOTOCATALYST

This chapter describes the formation of g-C$_3$N$_4$-CdS heterojunction and their photocatalytic performance towards methylene blue degradation. The mechanism for the enhanced photocatalytic activity in the composite after the formation of heterojunction is discussed based on the results of charge separation and charge mobility that were tracked through photoluminescence spectroscopy.

4.1 Introduction

As a fascinating conjugated metal free polymer, graphitic carbon nitride (g-C_3N_4) has been the hotspot in the field of photocatalysis and is regarded to be the most stable allotrope among C_xN_y, owing to its layered structure that is analogous to graphene (Sridharan et al. 2013b; Wang et al. 2009b). It exhibits numerous interesting properties, including visible light absorption (with an energy bandgap of 2.7 eV), chemical and thermal stability due to its tri-s-triazine structure, and a high degree of condensation (Liu et al. 2016; Ma et al. 2016; Tian et al. 2018). Furthermore, the ease of fabrication of g-C_3N_4 through thermal condensation utilizing the abundantly available nitrogen rich precursors such as urea, melamine and thiourea makes it even more attractive (Li et al. 2013; Su et al. 2010; Wang et al. 2012b). Nevertheless, the pristine g-C_3N_4 has weak photocatalytic effectiveness that can be ascribed to several aspects such as high excitation energy, lower charge mobility, low specific surface area and poor absorption at longer wavelengths (Mamba and Mishra 2016; Zhang et al. 2011). Combining g-C_3N_4 with inorganic semiconductors is a promising strategy to achieve spatial separation of charge carriers and enhanced photocatalytic performance (Dong et al. 2020; Sridharan et al. 2014a, 2015a; Yuan et al. 2019). Recently, combination of g-C_3N_4 with cadmium sulphide (CdS) – an attractive semiconductor sensitive to visible light (with bandgap of 2.4 eV), has been regarded as a promising route to achieve enhanced photocatalytic performance towards the degradation of organic pollutants as well as hydrogen generation (Xu and Zhang 2015). Also, it is observed that the formation of a heterojunction by the embedment of CdS over a highly stable polymeric g-C_3N_4 layer could protect them from photocorrosion (Fan et al. 2016a; Zheng et al. 2015). In order to realize this synergistic effect, the fabrication of a composite g-C_3N_4/CdS heterojunction photocatalyst through the hydrothermal approach towards the photodegradation of methylene blue (MB) dye molecules under visible light irradiation were reported. Efficient visible light absorption of CdS together with the efficient electron transfer from g-C_3N_4 to CdS is attributed to the enhanced photocatalytic activity of the as-synthesized g-C_3N_4-CdS composite in comparison to the pristine individual counterparts.

4.2 Experimental methods

4.2.1 Synthesis of g-C$_3$N$_4$

g-C$_3$N$_4$ was synthesized thermally by heating melamine (10 g) at 550 ^{o}C for 2 h with a heating rate of 5 ^{o}C min^{-1} under ambient pressure in air. Then, the as-obtained yellowish powder solid was collected and grinded to get the final sample.

4.2.2 Synthesis of CdS and g-C$_3$N$_4$/CdS photocatalysts

The g-C$_3$N$_4$/CdS heterojunction was synthesized *via* simple hydrothermal method reported elsewhere (Yue et al. 2016). In a typical synthesis, 4 mM Cd (NO$_3$)$_2$. 4H$_2$O and 8 mM CH$_4$N$_2$S were dispersed in 100 ml water under constant magnetic stirring. 0.5 g of g-C$_3$N$_4$ was added to the above solution and stirred for 15 min. The uniformly stirred solution was then transferred to a Teflon-lined stainless-steel autoclave of 150 ml capacity. The sealed autoclave was placed in an electric oven and the reaction was carried out at 180 ^{0}C for 12 h. After the autoclave was cooled down naturally, the resulting orangish yellow sediments were collected and washed thoroughly with DI water and absolute ethanol for three times. The sediments obtained were dried in an oven at 60 ^{0}C for 12 h. Pristine CdS was also prepared using an identical procedure without adding g-C$_3$N$_4$ for comparison.

4.2.3 Characterization

The crystalline nature of the obtained products was ascertained through powder X-ray diffraction (XRD) analysis and the patterns were recorded on a *Rigaku miniflex 600* X-ray diffractometer using Cu Kα radiation (λ = 1.5518 Å) in the range 2θ of 10° – 80° at a scan rate of 5° min^{-1}. The morphology of the synthesized products was analysed by field emission scanning electron microscopy (FESEM) using a *ZEISS Sigma* microscope at an acceleration voltage of 5 kV. UV-visible diffuse reflectance spectra (DRS) of the solid samples were recorded on a *Varian Cary 5000* UV-visible spectrophotometer equipped with an integrating sphere calibrated using barium sulfate (BaSO$_4$) as the reference standard. Photoluminescence (PL) spectra of the photocatalysts were measured using a

Fluoromax-4 TCSPC spectrophotometer (Horiba Jobin Yvon) at an excitation wavelength of 360 nm.

4.2.4 Photocatalytic degradation of methylene blue

The photocatalytic activity of the prepared g-C$_3$N$_4$/CdS nanostructured photocatalysts were assessed by observing the degradation of MB dye molecules under visible light (λ > 400 nm) irradiation. Home-made photocatalytic reactor was constructed by employing a 70W CDM-R lamp (*830 PAR30L 40D*, *Philips*, 4600 lumen) as the visible light source. Reaction slurry in a crystallizing dish (*Duran*®) of 300 ml capacity was prepared by suspending 200 mg of the photocatalyst in an aqueous solution containing 200 ml MB dye (20 ppm). Crystallizing dish containing the slurry was placed 8 cm away from the CDM-R lamp on top of a magnetic stirrer housed inside of the home-made photoreactor and was stirred under dark condition for 30 min to ensure the adsorption of MB dye molecules on the surface of the photocatalysts. During the photocatalytic reaction, aliquots (5 ml) of the reaction slurry were withdrawn at regular intervals of time, centrifuged for separating the photocatalyst and stored in amber glass vials. For consistency all experiments were conducted in triplicate.

The rate of photocatalytic degradation of MB was determined from the absorption spectra of the centrifuged aliquots that were measured using a UV-Vis Spectrophotometer (*Ocean Optics, SD 2000*) and were compared with those of the original dye and centrifuged aliquot collected before irradiation (dark condition). Decrease in the absorbance of MB with respect to irradiation time was used to determine the efficiency of the photocatalysts that were calculated using the equation,

$$Efficiency\left(\%\right)=\frac{C_0-C}{C_0}\times100 \quad (4.1)$$

where, C$_o$ is the initial concentration and C is the concentration of the dye after light irradiation.

4.3 Results and discussion

4.3.1 Morphological and structural characterization

Figure 4.1 shows the XRD pattern of the obtained layered structures of g-C_3N_4 with two distinct diffraction peaks, the weak diffraction peak (100) centred at 13.2° (marked by * mark) was attributed to in-planar structural packing motif with a separation of 0.669 nm, and the strong peak at 27.7o corresponds to the (002) peak of the interlayer d-spacing of 0.3216 nm (Chang et al. 2013; Wang et al. 2009b). The CdS exhibited hexagonal wurtzite structure and is in accordance with JCPDS No. 65-3414 (Yan et al. 2016). The composite sample exhibited diffraction peaks corresponding to both g-C3N4 and CdS, reflecting the presence of two phases, which could be distinctly observed.
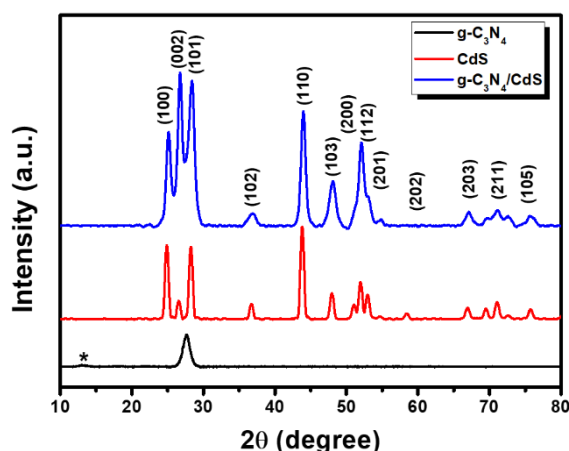
Figure 4.1: X-ray diffraction patterns of g-C_3N_4, CdS and g-C_3N_4/CdS photocatalysts.

The morphology of the obtained samples was investigated by field emission scanning electron microscopy (FESEM). As observed in Figure 4.2a, the low magnification image of pristine g-C_3N_4 exhibits the morphology of irregular and aggregated two-dimensional layers stacked over each other. The high magnification image of g-C_3N_4 presented in Figure 4.2b, indicates the aggregation of the 2D layers as spherical structures. The low magnification image of CdS in Figure 4.2c indicates the presence of uniformly spread particles with a size ranging between 30-80 nm as confirmed from the high magnification image presented in Figure 4.2d. Low magnification image shown in Figure 4.2e indicates the largely porous surface of the g-C_3N_4 layer enriched with a lot of CdS particles. The

high magnification image shown in Figure 4.2f clearly indicates the embedment of uniformly sized CdS particles on the surface of the g-C$_3$N$_4$ layer.
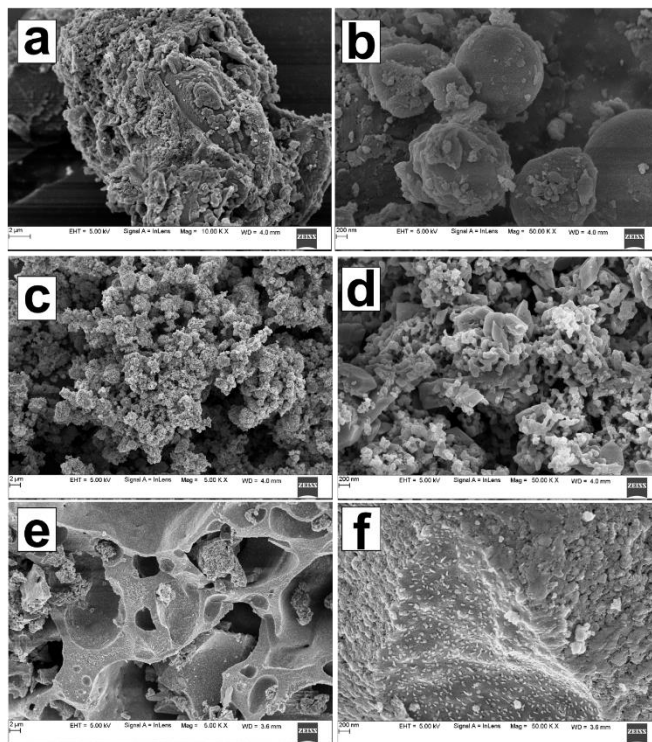
Figure 4.2: Morphological characterization of the as-synthesized g-C$_3$N$_4$, CdS and g-C$_3$N$_4$/CdS photocatalysts. FESEM micrographs under low and high magnifications corresponding to g-C$_3$N$_4$ (a, b), CdS (c, d) and g-C$_3$N$_4$/CdS (e, f).

4.3.2 X-ray Photoelectron Spectroscopy

XPS was performed to precisely confirm the formation of g-C$_3$N$_4$/CdS heterojunction and the peaks corresponding to C, N, Cd and S observed from the survey spectrum shown in Figure 4.3 can be considered as a substantial proof. As shown in Figure 4.3, the typical C and N peaks observed in the XPS spectrum of g-C$_3$N$_4$ are consistent with previous reports (Chang et al. 2015). O presumably is originated from the surface absorbed H$_2$O/CO$_2$ molecules when melamine is thermally treated at high temperature (Cao et al. 2014).
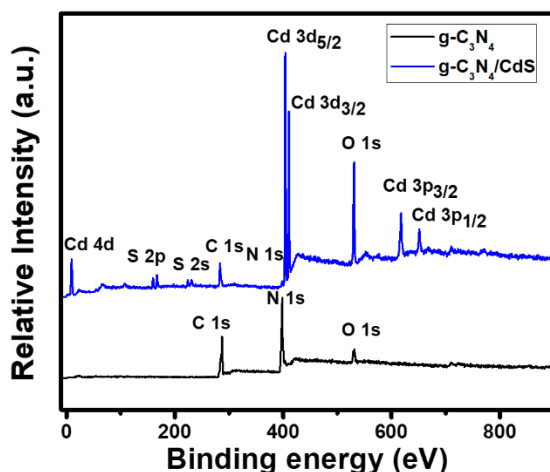
Figure 4.3: X-ray photoelectron survey spectrum of the as-synthesized g-C₃N₄ and g-C₃N₄/CdS photocatalysts.

Figure 4.4a indicates the peaks emanating at 290.6 and 292.3 corresponding to C 1s that can be attributed to the formation of C-N-C bond. As seen from Figure 4.4b the N 1s spectra can be fitted to three separate peaks at binding energy of 399.3, 399.7 and 399.9 eV, respectively. The strong peak centring at 399.7 eV in Figure 4.4b is identified as the sp2-hybridized N involved in triazine rings (C-N=C) and the peak at 399.9 eV regarded as the tertiary nitrogen N-(C)$_3$ groups. The peak at 399.3 eV indicates the presence of amino functional groups (C-N-H) (Ge and Han 2012; Yan et al. 2016). The high-resolution Cd 3d spectra of g-C₃N₄/CdS (see Figure 4.4c), reveals the peaks of Cd 3d$_{5/2}$ and Cd 3d$_{3/2}$ located at 406.1 and 412.0 eV, which correspond to the Cd^{2+} state. Figure 4.4d shows the XPS signals of S 2p observed at 159.8 and 166.4 eV, as is expected for S^{2-} in CdS (Pawar et al. 2014).
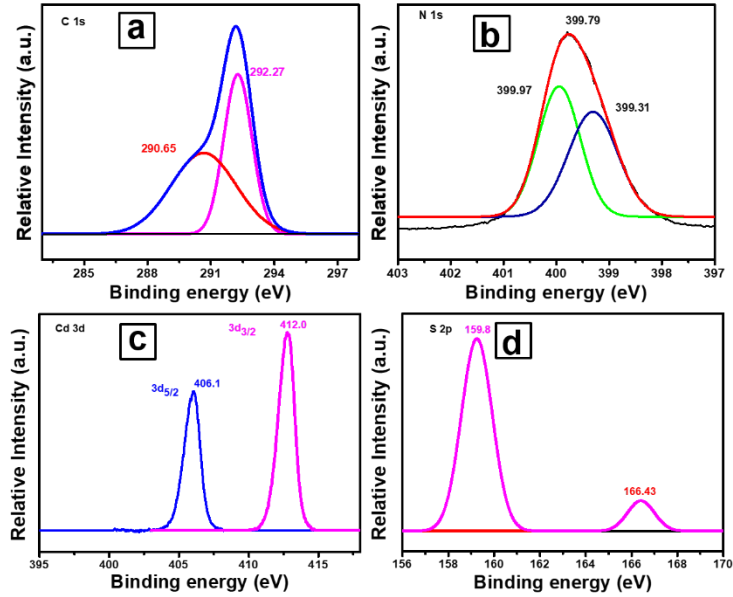
Figure 4.4: X-ray photoelectron spectra of g-C$_3$N$_4$/CdS photocatalyst for (a) C 1s (b) N 1s (c) Cd 3d and (d) S 2p.

4.3.3 Optical properties

The optical properties were investigated through UV-vis DRS for understanding the visible light absorption capability of the as-synthesized photocatalysts and for estimating their energy bandgap. DRS is related to the absorption coefficient by the Kubelka-Munk (K-M) function F(R) given by the Eq. (4.2)

$$F(R) = \frac{(1-R)^2}{2R} \qquad (4.2)$$

where reflectance R = R$_{sample}$/R$_{reference}$ (Shenoy and Sridharan 2020). The UV-vis DRS of the as-synthesized photocatalysts are presented in Figure 4.5a, while [F(R)hv]$^{1/2}$ versus hv plots in Figure 4.5b were used for deducing their corresponding bandgap energy by extrapolating the linear portion of the graph to (F(R)hv)$^{1/2}$ = 0. The absorption edges of pure g-C$_3$N$_4$ and CdS are located at 470 and 590 nm, which corresponds to the bandgaps of 2.63 and 2.08 eV, respectively. After of the embedment of CdS nanoparticles on g-C$_3$N$_4$, the absorption edge arised at ~500 nm with a corresponding energy bandgap of 2.13 eV.
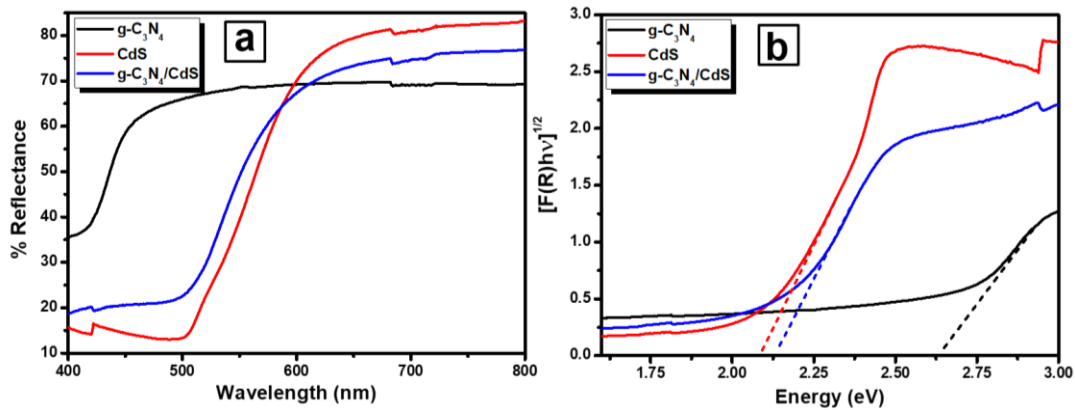
Figure 4.5: (a) UV-vis diffuse reflectance spectra of the as-synthesized g-C$_3$N$_4$, CdS and g-C$_3$N$_4$/CdS photocatalysts and (b) their corresponding Tauc's plots ([F(R)hυ]$^{1/2}$ vs hυ plot). The effective bandgap of the photocatalysts are estimated from the intercept on the x-axis (extrapolated dashed lines).

Figure 4.6 shows the PL spectra of g-C$_3$N$_4$, CdS and g-C$_3$N$_4$/CdS obtained by exciting at 360 nm. A strong PL emission peak is observed for g-C$_3$N$_4$, which can be attributed to the recombination of photogenerated electron-hole pairs (Yue et al. 2016; Zou et al. 2018). Although intensity of PL emission peak in CdS is comparatively weaker than g-C$_3$N$_4$, there is recombination of charge carriers occurring in them as well. In contrast, the PL emission peak intensity of g-C$_3$N$_4$/CdS is almost negligible than the individual counterparts, which confirms the high separation efficiency of the photogenerated charge carriers and makes it ideal to function as a photocatalyst.
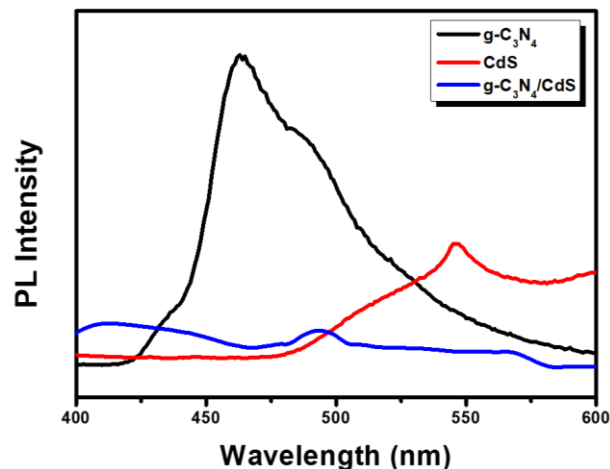
Figure 4.6: Photoluminescence spectra of g-C$_3$N$_4$, CdS and g-C$_3$N$_4$/CdS photocatalysts.

4.3.4. Visible light driven photocatalytic degradation of methylene blue

The photocatalytic activity of pristine g-C$_3$N$_4$, CdS and composite of g-C$_3$N$_4$ with CdS, was assessed by photodegradation of methylene blue under visible light irradiation. UV-Vis absorption spectra presented in Figure 4.7a-c exhibiting the steady and gradual decrease in the absorption peak of MB centered at ~665 nm with respect to the increase in the visible light irradiation time is indicative of the reduction in its concentration. Plot depicting the variation in the concentration of MB with respect to the visible light irradiation time in the presence of various photocatalysts is presented in Figure 4.7d. As observed from Figure 4.7d, the negligible photodegradation of MB in the absence of any photocatalyst indicates its high chemical stability. The concentration of MB decreased to 5% and over 95% photodegradation was achieved in 100 min in the presence of g-C$_3$N$_4$/CdS under visible light irradiation. Photodegradation of MB in the presence of pristine g-C$_3$N$_4$ and CdS was limited to just 88% and 84%, respectively even after 240 min and 180 min of visible light irradiation.
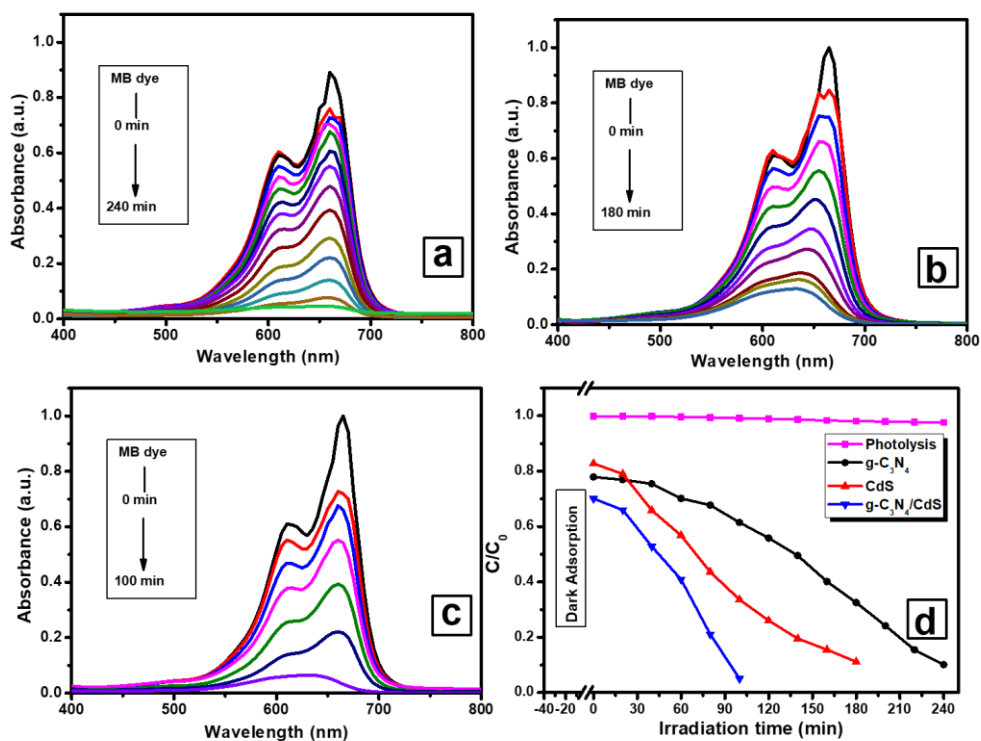
Figure 4.7: UV-vis absorption spectra depicting the visible light induced photodegradation of methylene blue in the presence of (a) pristine g-C$_3$N$_4$, (b) CdS and (c) g-C$_3$N$_4$/CdS photocatalyst. (d) Plot showing time-dependent photodegradation of 20 ppm MB under visible light irradiation in the presence of g-C$_3$N$_4$, CdS and g-C$_3$N$_4$/CdS as photocatalysts.

Figure 4.8 depicts a schematic diagram of the photocatalytic degradation of MB over g-C$_3$N$_4$/CdS composite. Activity of a photocatalyst is majorly dependent on the separation and transfer of photogenerated charge carriers. Under the visible light irradiation both g-C$_3$N$_4$ and CdS can absorb visible light to generate photoinduced electron-hole pairs. The appropriate band potentials of the individual semiconductors favour the spontaneous transfer of the photogenerated charge carriers, wherein electrons from g-C$_3$N$_4$ moves to the surface of CdS while the holes from CdS move to g-C$_3$N$_4$. Since the photogenerated charge carriers move in opposite directions the recombination probability is greatly reduced thereby enhancing the charge separation efficiency (Pawar et al. 2014; Yan et al. 2016; Yue et al. 2016). Holes accumulated in VB of g-C$_3$N$_4$ and electrons in the CB of CdS react

66

with hydroxyl ions and dissolved oxygen molecules in water to produce hydroxyl radicals ($^{•}OH$) and superoxide anion radical ($^{•}O_2^{-}$), respectively. The reactive species generated during the photocatalytic reactions initiate the photodegradation reactions. In this way, the efficient separation of photoinduced charge carriers leads to a significant enhancement in the photocatalytic activity which was consistent with the PL quenching observations (see Figure 4.4).
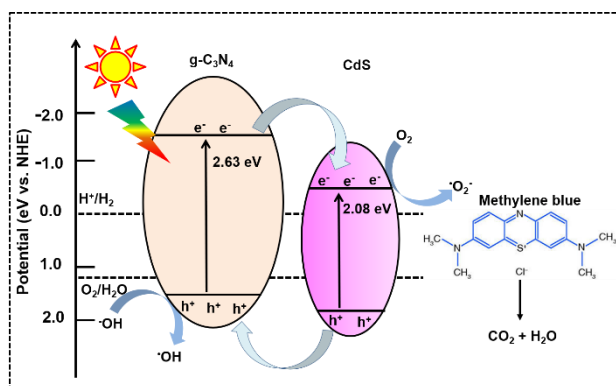
Figure 4.8: Schematic diagram of the separation and transfer of photogenerated electron-hole pairs over g-C_3N_4/CdS composite under visible light irradiation.

4.4 Summary

In summary, g-C_3N_4/CdS heterojunction were synthesized through hydrothermal method and were employed as photocatalysts in the degradation of methylene blue dye molecules under visible light irradiation. Structure and morphology of the as-prepared photocatalysts analysed using XRD and FESEM confirmed the formation of g-C_3N_4/CdS heterojunction. UV–Vis DRS and photoluminescence spectroscopy were carried out for understanding the energy bandgap and charge carrier characteristics. Among the synthesized photocatalysts, g-C_3N_4/CdS heterojunction showed enhanced photocatalytic efficiency for the degradation of 20 ppm MB. The superior photocatalytic performance of g-C_3N_4/CdS was attributed to the reduced rate of recombination of the photogenerated electron-hole pairs, as well as increased visible light absorption with the addition of CdS.

CHAPTER 5

FIRST PRINCIPLES ELECTRONIC STRUCTURE CALCULATIONS: CdS/CdSe HETEROSTRUCTURE

This chapter provides a theoretical understanding of the relationship of the interface and enhanced photocatalytic activity of CdS/CdSe heterostructures. The energy band structure and charge transfer at the heterojunction are systematically studied through the hybrid density functional theory approach. The valence and conduction band edge positions of the semiconductors were determined and the type of heterojunction formed based on the band alignment was discussed.

5.1 Introduction

Efficient generation of charge carriers, charge separation and migration to the catalytic surface are the determining factors that affects the photocatalytic performance of a given semiconductor (Cheng et al. 2018). In photocatalytic reaction such as water splitting or photodegradation of organic pollutants, the redox reactions on the semiconductor's surface must be thermodynamically favorable. A photocatalytic reaction can only take place when the band edges of semiconductor are appropriately placed relative to the redox reaction potentials. In particular, the position of the valence band maximum (VBM) and conduction band minimum (CBM) must lie lower and higher in energy relative to the oxidation and reduction potentials respectively. In case of CdS, the photogenerated electrons in the conduction band have a good reducing ability for hydrogen evolution. However, the photogenerated holes in the valence band are prone to self-oxidation, results to severe photocorrosion in the system that significantly reduces its photocatalytic efficiency. To overcome this drawback, suitable band engineering is very essential which in turn help to separate the electron–hole pairs generated under visible light irradiation, decrease the rate of recombination and photocorrosion. Heterojunction formation of CdS with some other efficient photocatalyst could be a suitable strategy for further improvement of the photocatalytic efficiency and its durability. Cadmium selenide (CdSe) is one among the many other narrow bandgap semiconductors having a direct bandgap of 1.7 eV, capable of absorbing more of visible light spectrum, would be a good choice for making the heterostructure (Bera et al. 2018; Chauhan et al. 2016). Experimental studies shows that combination of CdS/CdSe heterostructure could be a suitable candidate for water splitting and photovoltaic applications, owing to its internal charge separation at the interface (Bera et al. 2018; Bridewell et al. 2015). Although an extensive experimental investigation has been carried out for CdS/CdSe heterostructures towards its photocatalytic applications, proper theoretical knowledge such as the detail electronic structure, accurate position and character of the band edges are still lacking, which are very essential for a better understanding of catalytic mechanism such as light induced charge separation, electron and hole pair recombination etc. In this work, hybrid density functional theory calculations

were used obtain an accurate electronic band structure of CdS (110) and CdSe (110) surfaces as well as CdS/CdSe heterojunction and subsequently investigated the possible improvement of photocatalytic activity with the help of their proper band alignment with respect to the reduction and oxidation potential.

5.2 Computational details

Density functional theory calculation using the projector augmented wave (PAW) method implemented in Vienna *ab initio* Simulation Package (VASP) to determine the accurate geometric and electronic structure of the CdS, CdSe surfaces and CdS/CdSe heterostructure (Kresse and Furthmüller 1996a; Perdew and Wang 1992) were employed. The generalized gradient approximation (GGA) of Perdew-Burke-ern-zerhof (PBE) scheme to describe the exchange and correlation potential and used the empirical correction method proposed by Grimme (DFT-D3), which was proved to be a good description for long-range vdW interactions, to depict vdW interaction. A very high wave function cutoff energy of 500 eV was used in each calculation to obtain an accurate result. The structure relaxation was performed in each case setting the convergence criteria 1×10^{-5} eV for energy and 0.01 eV˚A^{-1} for force. Since PBE functional underestimates the band-gap due to the presence of artificial self-interaction, hybrid-DFT calculation using Heyd-Scuseria-Ernzerhof (HSE06) hybrid functional, with 25% Hartree-Fock exchange energy contribution to accurately determine the band edge positions were performed (Heyd et al. 2003).

5.3 Results and discussion

5.3.1 Structural and electronic properties

Before exploring the properties of CdS/CdSe heterostructure, the crystal structure of their bulk counterparts were investigated. Both CdS and CdSe belong to the cubic sphalerite structure with an F-*43m* space group. The optimized lattice parameters a = b = c = 5.82 Å for CdS and a =b = c = 6.07 Å for CdSe are in good agreement with the experimental values (Wei and Zhang 2000). Next, CdS (110) and CdSe (110) surface, using optimized bulk

geometry were modeled. A vacuum region of 10 Å thickness perpendicular to the surface is used in the unit cell, to avoid the interactions between neighboring slabs. The unit cell of an eight-layer CdS (110) and CdSe (110) slabs are illustrated in Figure 5.1a and 5.1b. Finally, the heterojunction was modeled by placing CdSe (110) slab over CdS (110) as shown in Figure 5.1c considering average values for in-plane lattice parameters, with a lattice mismatch less than 2.0%. All the atoms in the modeled surfaces and heterostructures to get the appropriate electronic structure information were relaxed. The optimum separation between the surfaces is 4.74 Å is a little higher than the interlayer distances of CdS (110) and CdSe (110) which are 4.11 Å and 4.15 Å respectively.
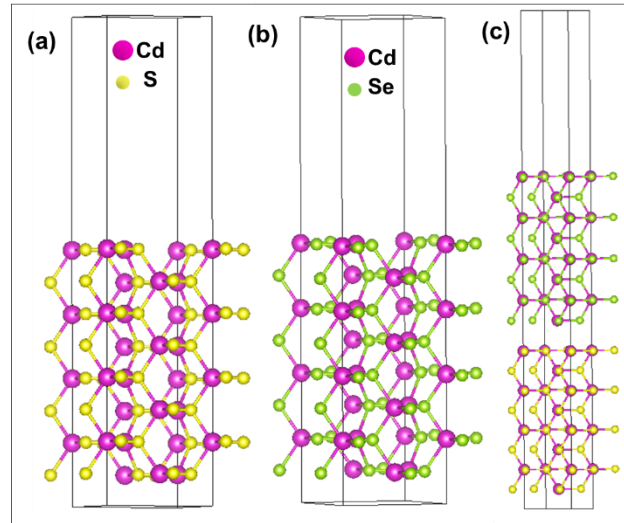
Figure 5.1: Optimized geometric structures of (a) CdS (110) surface, (b) CdSe (110) surface and (c) CdS/CdSe heterostructure. Here pink, yellow and green spheres represent Cd, S, and Se atoms respectively.

The bulk CdS and bulk CdSe are direct bandgap semiconductors in which both the VBM and CBM are located at Γ point. The calculated bandgaps are 2.37 eV and 1.80 eV respectively, which are consistent with the values reported in the literature (Mo et al. 2017). In the case of CdS (110) and CdSe (110) surfaces, both the surfaces have a direct bandgap of 2.58 eV and 2.14 eV respectively at the Γ point. The calculation shows that the CdS/CdSe heterostructure is also a direct gap system with bandgap 1.66 eV at Γ point.

Band structures of CdS (110), CdSe (110), and the CdS/CdSe heterostructure are shown in Figure 5.2a-c. To understand the orbital character of band edges, the atom projected DOS for each system were plotted as shown in Figure 5.2a-c. From the atom projected DOS of CdS (110), it is evident that the VBM consists of S 3p states, whereas Cd 3d states are contributed to the CBM. In the case of the CdSe (110) surface, Se 4p is contributing to the VBM, whereas Cd 4p states are contributing to the CBM. In CdS/CdSe heterojunction, VBM is dominated by S 3s and Se 4p states whereas CBM is composed of Cd 3d character. To investigate the catalytic activity of these materials, the relative band position of the heterostructure concerning the reduction and oxidation potential of water is very essential.
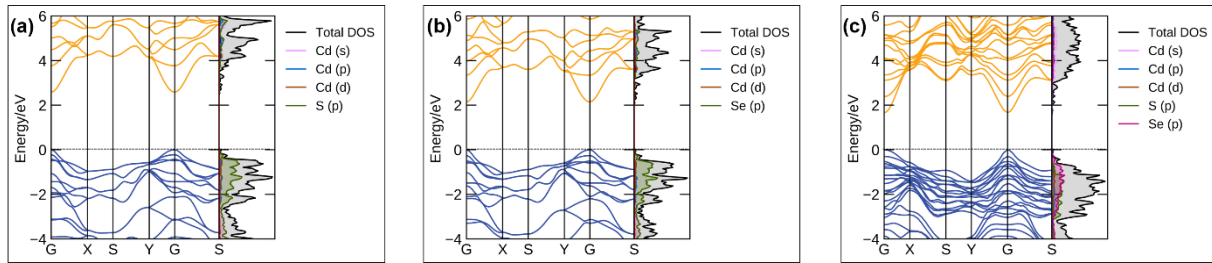
Figure 5.2: Calculated band structures and atom projected density of state plots of (a) CdS (110) surface (b) CdSe (110) surface and (c) CdS/CdSe heterostructure using a hybrid-DFT calculation.

5.3.2 Work function analysis and charge density difference

The work function (Φ) of material, in this case, is a crucial parameter, commonly used as an intrinsic reference for band alignment (Liu 2015). This is the minimum energy required for an electron to reach the vacuum level from the Fermi level (E_F). One can estimate the material-specific work function from the following equation:

$$\Phi = E_{vac} - E_F \qquad (5.1)$$

where E_F is the Fermi energy. E_{vac} is the energy of a stationary electron in the vacuum nearby the surface. This can be estimated from the average electrostatic potential plot for a surface calculation, considering a sufficient amount of vacuum in the unit cell. Calculated electrostatic potential for CdS (110), CdSe (110) and CdS/CdSe heterostructure are plotted

in Figure 5.3a-c. On the basis of equation (4), the calculated work functions for CdS (110), CdSe (110) and CdS/CdSe heterostructure are 4.99 eV, 4.60 eV and 4.72 eV respectively.
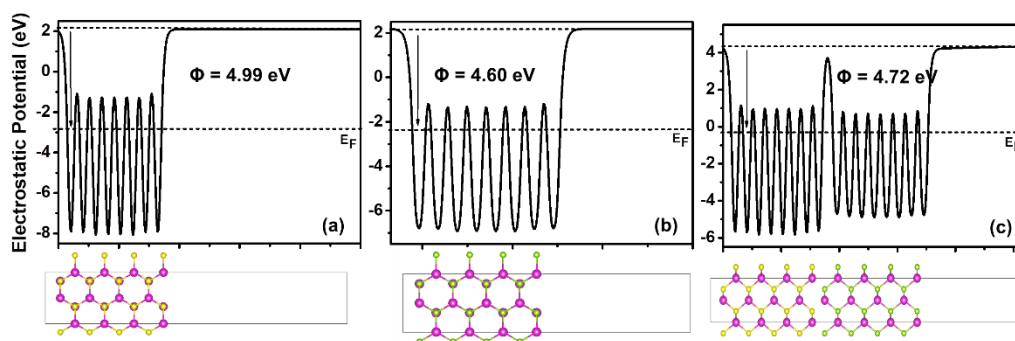
Figure 5.3: Average electrostatic potential plots for (a) CdS (110) surface, (b) CdSe (110) surface and (c) CdS/CdSe heterostructure. Calculated work functions for CdS (110), CdSe (110) and CdS/CdSe heterostructure are 4.99 eV, 4.60 eV and 4.72 eV respectively.

The redox potential of a semiconductor is assessed by the positions of its valence and conduction band edges concerning the normal hydrogen electrode (NHE) potential. Generally, a positive valence band maximum of a semiconductor for the NHE potential indicates that the photogenerated holes have stronger oxidation ability, while the negative conduction band minimum to the NHE potential shows a strong reducing ability of the photogenerated electrons. Therefore, accurate band edge position for NHE will provide detailed information about the photocatalytic efficiency of a semiconductor. The edge positions of VB and CB for all three systems considering the Mulliken electronegativity rules (Liu 2015), where the energetic position of the CBM and VBM is determined through the following equations:

$$E_{VB} = \chi - E_e + 1/2\ E_g \qquad (5.2)$$

$$E_{CB} = E_{VB} - E_g \qquad (5.3)$$

here E_g represents the bandgap of the system, E_e is the energy of free electrons in the hydrogen scale (4.5 eV), $E_{VB,}$ and E_{CB} are the VB and CB edge potentials, respectively (Guo et al. 2017). χ in equation (5.2) is the Mulliken electronegativity of the semiconductor which can be obtained by taking the geometric mean of the Mulliken electronegativity of constituent atoms in the semiconductor. The χ of an atom is the arithmetic mean of its electron affinity and the first ionization energy. The calculated values of χ for CdS and CdSe are 5.18 and 5.14 eV respectively. Using the calculated bandgap values for CdS (110) and CdSe (110) along with equations (5.2) and (5.3), the band edge positions of CB and VB of CdS concerning NHE as -0.62 V and 1.96 V respectively and the band edge positions of CB and VB of CdSe are -0.43 V and 1.71 V respectively. The results are illustrated in Figure 5.4.
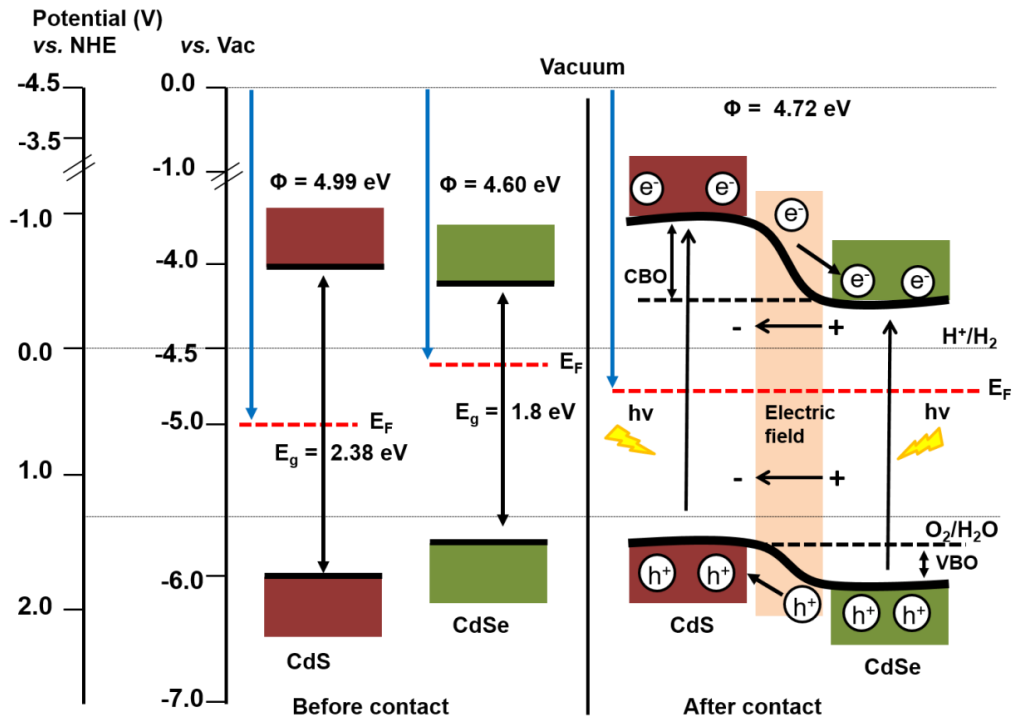
Figure 5.4: Diagram of band edge positions of CdS (110) and CdSe (110) surfaces before and after the formation of heterojunction for the vacuum level.

In the case of CdS/CdSe heterostructure, the relative positions of CB and VB of both the semiconductors are expected to change significantly because of the change in the Fermi energy. Since the work function of CdS (4.99 eV) is higher than CdSe (4.60 eV), electrons will flow from CdSe to CdS while forming the heterojunction, until the Fermi level of both the semiconductors is aligned. The calculation shows that the work function of the CdS/CdSe heterojunction is 4.72 eV, which is lying in between that of their semiconductors. Therefore, at equilibrium, the CB and VB of CdS shift upwards by 0.49 eV, while CB and VB of CdSe shifted downwards by 0.1 eV due to the change of Fermi level in the heterojunction. This led to the generation of large band offset both in the valence band and conduction band. Internal charge separation is expected due to this band offsets. To confirm the charge separation at the interface of CdS/CdSe heterojunction, the charge density difference was calculated using the following equation

75

$$\Delta\rho = \rho_{CdS/CdSe} - \rho_{CdS\ (110)} - \rho_{CdSe\ (110)} \qquad (5.4)$$

here $\rho_{CdS/CdSe}$, $\rho_{CdS\ (110)}$ and $\rho_{CdSe\ (110)}$ represent the charge densities of CdS/CdSe heterostructure, the CdS (110) and the CdSe (110) surfaces respectively. The result is shown in Figure 5.5b, which indicates that the charge density is redistributed by the formation of hole-rich and electron-rich regions near the semiconductor interface. The accumulation of electrons in CdS is indicated by yellow isosurface, and electron depletion in the CdSe side is shown as cyan isosurface in Figure 5.5a. Note that the charge redistribution is confined in a small region close to the CdS/CdSe interface. There is no significant change is visible in the region farther away from the interface. This is because of the strong build-up potential due to the separated charges, which acts against the diffusion process of the separated electron/holes. The planar-averaged electron density difference along the z-direction for the heterojunction is plotted in Figure 5.5a indicates that the edge of CdS in the junction is populated with a negative charge carrier, while the CdSe edge is composed of a positive charge carrier. This signifies that the charge separation leads to the formation of a built-in electric field at the interface in the direction from CdSe to CdS during the formation of CdS/CdSe heterojunction which will help to separate the photogenerated charge carriers spatially across the heterojunction in opposite direction, thereby enhancing the possibility of higher photocatalytic performance. The calculated values of the valence band offset (VBO) and conduction band offset (CBO) for CdS/CdSe heterostructure are 0.14 eV and 0.58 eV respectively.
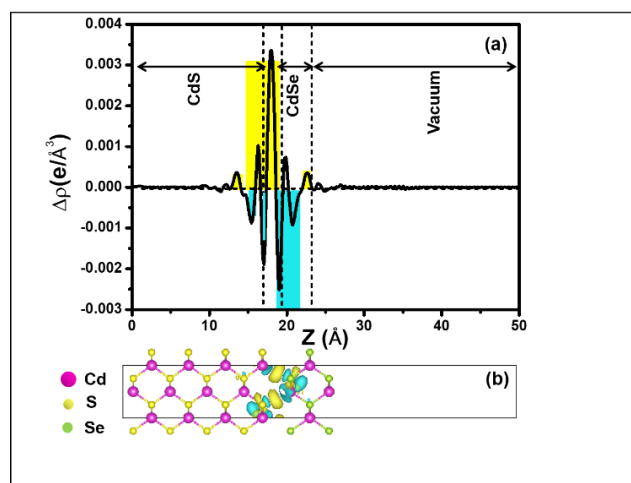
Figure 5.5: (a) Planar-averaged electron density difference $\Delta\rho(z)$ for CdS/CdSe heterostructure. The cyan and yellow region represent electron depletion and electron accumulation respectively. (b) Charge density difference plot for CdS/CdSe heterostructure.

Under visible light irradiation, when the electron transition takes place from the VB to the CB of the heterostructure, owing to the existence of CBO, the electrons will start moving from CdS to CdSe. On the other hand, the VBO induces the simultaneous movement of holes created in the VB from CdSe to CdS. As a result, negative charges get accumulated over CdSe and conversely positive charges on CdS. Thus, photoexcited electrons and holes are effectively separated and will participate in the photocatalytic reaction. The photoexcited electrons of the CdS/CdSe heterostructure accumulated in the CB which is mainly contributed from CdSe. Since the CB edge potential is -0.53 V with respect to NHE, which is more negative than that of H^+/H_2O (0 V), can reduce the H^+ to H_2; while the photogenerated holes accumulated at VB which is from CdS portion of the heterojunction has edge potential of 1.61 V for NHE, is more positive than that of O_2/H_2O (1.23 V), has very good oxidation ability to produce superoxide anion radicals and degrade the organic pollutants. Therefore, CdS/CdSe becomes a type II heterojunction in which band edge positions are favorable for simultaneous oxidation and reduction reactions. The mobility of charge carriers in a semiconductor photocatalyst has a greater influence on its

photocatalytic activity. The higher the mobility better is the performance of the photocatalyst. The mobility of charge carrier can be estimated from the band effective masses of a semiconductor as the mobility of the charge carriers is inversely proportional to the effective mass. Therefore, a lower value of effective mass promotes efficient migration of charge carriers and suppresses their recombination rate. The effective masses of electrons and holes by fitting the parabolic portions to the CBM and VBM were investigated using the following equation:

$$m_x{}^* = \hbar^2 \left(\frac{d^2E}{dk^2}\right)^{-1} \qquad (5.5)$$

where $m_x{}^*$ (x = e, h) represents the effective mass of x-type charge carrier, E is the band edge energy as a function of the wave vector k and $\hbar$ is the reduced Planck constant. A large difference in $m_e{}^*$ and $m_h{}^*$ i.e. larger value of $m_h{}^*/ m_e{}^*$ in a semiconductor will suppress the charge carrier recombination (Li et al. 2019). Calculated effective masses are tabulated in Table 5.1. Interestingly, the calculation shows that the value of $m_h{}^*/ m_e{}^*$ is greater in heterostructure than that of individual semiconductor counterpart, indicating a larger lifetime of photogenerated charge carriers in the heterostructure that will further improve the photocatalytic activity.

Table 5.1 The effective mass of charge carriers in CdS (110), CdSe (110) surface and CdS/CdSe heterostructure.

System	$m_e{}^*$ (in e⁻ mass)	$m_h{}^*$ (in e⁻ mass)	$m_h{}^*/ m_e{}^*$
CS (110)	0.272	-1.183	4.349
CdSe (110)	0.223	-1.060	4.75
CdS/CdSe heterostructure	0.210	-1.230	5.857

5.4 Summary

In summary, the electronic structures of the CdS (110), CdSe (110) and CdS/CdSe heterostructure were investigated on the basis of hybrid-DFT method. Calculated band structure and atom projected DOS confirm that the CdS/CdSe forms a type-II heterostructure. The proper band edge positions and their alignment with respect to the NHE were determined from the calculated bandgap and work function for each surface. The band edge positions of both the semiconductors are changed with the Fermi level while formation of heterostructure and a large band offset both in valence and conduction band was observed. Therefore, under the influence of visible light irradiation, the photogenerated electrons and holes could move from CB of CdS to that of CdSe and from VB of CdSe to that of CdS respectively. The existence of an internal electric field near the interface due to large band offsets will facilitate the charge separation across the CdS/CdSe interface, which in turn reduce the recombination of electron–hole pairs. The charge carrier mobility is also improved in the heterostructure and the band alignment of the system is such that both photoreduction and photooxidation processes associated with water splitting are energetically feasible. The results indicate that the CdS/CdSe heterojunction may have wide application in photocatalysis for pollutant degradation and water splitting.

CHAPTER 6

Z-SCHEME WO$_3$/MoS$_2$ HETEROJUNCTION: EXPERIMENTAL AND THEORETICAL INSIGHTS

This chapter is a combination of various experimental results and first-principles calculations with a new and interesting discussion to explain the photocatalytic activity of WO$_3$/MoS$_2$ heterojunction.

6.1 Introduction

Hydrogen, as a clean and highly efficient renewable energy resource, has been extensively investigated as an alternative to the diminishing fossil fuel (Zhu et al. 2019). On that prospect, electrocatalytic water splitting with zero emission of CO_2 serves as the major technology to generate hydrogen (Dai et al. 2017). In general, the hydrogen adsorption free energy (ΔG_H) at the surface of catalyst explains the difficulty of hydrogen desorption and adsorption (Voiry et al. 2016). In accordance with the Sabatier mechanism, the interactions between reactants and catalyst should neither be too strong nor too weak, for the reaction to proceed efficiently and thus ΔG_H close to zero enables excellent hydrogen evolution reaction (HER) performance (Hinnemann et al. 2005). It is desirable to explore the low-cost nonnoble earth-abundant metal catalysts as a highly efficient HER materials. Tungsten trioxide (WO_3), an important n-type semiconductor, have recently been given added attention owing to its non-toxicity and unique optical properties (Durán-Álvarez et al. 2020; Rani et al. 2019). Furthermore, it has exciting merits such as inexpensive, ease of synthesis, good stability both under acidic and basic conditions, excellent electron transport, and photo corrosion resistance (Omrani and Nezamzadeh-Ejhieh 2020; Shang et al. 2017). However, WO_3 has lower photocatalytic activity and cannot satisfy the practical requirements when it is applied singly. Also, the photocatalytic activity of pure WO_3 is limited owing to its narrowed light absorption range and the rapid recombination of photogenerated electron-hole pairs (Isari et al. 2020). Compared with a single photocatalyst, Z-scheme heterojunction photocatalysts have the advantage of speeding up the separation of photogenerated charges, keeping the reduction and the oxidation reactions at two different materials and effectively promoting HER (Yu et al. 2017). Thus, we have constructed WO_3/MoS_2 heterojunction and studied their photocatalytic activity towards both the degradation of organic pollutants and for hydrogen generation reaction employing density functional theory.

6.2 Experimental details

6.2.1 Synthesis of WO₃

WO_3 was prepared via the hydrothermal method reported elsewhere (Zhang et al. 2014a) with NaCl as a capping agent. In a typical synthesis, 3.30 g of $Na_2WO_4.2H_2O$ and 1.16 g of NaCl was dissolved in 75 ml of DI water, and the pH of the solution was adjusted to 2.5 using 3 mol L^{-1} HCl aqueous solution. The above solution was transferred into a Teflon-lined stainless-steel autoclave which was placed in an electric oven at 180 °C for 24 h after which it was allowed to cool down before the white precipitates were collected. The final precipitate was washed thoroughly with DI water and absolute ethanol and dried in an oven at 80 °C for 12 h and the product was named as WO_3.

6.2.2 Synthesis of WO₃/MoS₂ nanocomposites

In a typical synthesis, the as-prepared WO_3 (0.1 g) was dispersed in 40 ml (0.5 M) glucose solution under ultra- sonication for 10 min. Then 0.4 g of sodium molybdate and 0.8 g of thiourea were added to the above solution and magnetically stirred for an hour. The obtained solution was transferred into a Teflon-lined stainless-steel autoclave which was placed in an electric oven at 200 °C for 10 h after which it was allowed to cool down to room temperature. The final precipitate was washed thoroughly with DI water and absolute ethanol and dried in an oven at 80 °C for 12 h and the product was named as WO_3/MoS_2. For comparison, the pure MoS_2 was synthesized under the same experimental conditions (Zeng et al. 2019a).

6.2.3 Characterization

Powder X-ray diffraction (XRD) was employed to ascertain the crystalline nature of the as-synthesized semiconductor photocatalysts. XRD patterns were recorded on a *Rigaku miniflex 600 X-ray diffractometer* using Cu Kα radiation (λ = 1.5518 Å) in the range 2θ of 10° -80° at a scan rate of 5° min^{-1} and the data was analyzed by matching with the JCPDS

database. Morphology and the compositional analysis were conducted using a field emission scanning electron microscope (*ZIESS, Sigma*) fitted with an energy dispersive X-ray spectrometer (EDS). Optical properties of the as-synthesized photocatalysts were studied by recording the UV-visible diffuse reflectance (DRS).

6.2.4 Photocatalytic degradation of methylene blue

Photocatalytic activity of as-synthesized photocatalysts was accessed by monitoring the degradation of MB under visible light (λ=400 nm) irradiation. A photocatalytic reactor was constructed in-house by employing a 70W CDM-R lamp (*830 PAR30L 40D, Philips,* 4600 lumen) as the visible light source. Crystallizing dish (*Duran*) of 300 ml capacity was used for preparing the reaction slurry by suspending 200 mg of the photocatalyst in an aqueous solution containing 200 ml MB (10 ppm). Reaction slurry in the crystallizing dish was placed 8 cm away from the CDM-R lamp on top of a magnetic stirrer housed inside of the home-made photoreactor and was stirred under dark condition for 30 min to ensure the adsorption of MB on the surface of the photocatalysts. Aliquots (5 ml) of the reaction slurry were withdrawn at regular intervals of time, centrifuged for separating the photocatalyst and their absorption spectrum were recorded using a UV-Vis spectrophotometer (*SD 2000, Ocean Optics*). For consistency all experiments were conducted in triplicate. The efficiency of the photocatalysts were determined by comparing the absorption spectrum of the centrifuged aliquots with that of the original 10 ppm MB solution. Decrease in the absorbance of MB with respect to irradiation time was used to determine the efficiency of the photocatalysts that were calculated using the equation,

$$Efficiency\left(\%\right) = \frac{C_0 - C}{C_0} \times 100 \quad (6.1)$$

where, C_o is the initial concentration and C is the concentration of the dye after light irradiation.

6.2.5 Computational methodology

The crystal and electronic structures of pristine and functionalized semiconductors were determined by density functional theory (DFT) calculations using the Vienna *ab initio*

simulation package (VASP), where the ion- electron interactions are described by the projected augmented wave (PAW) method. The exchange-correlation for electrons is represented by the generalized gradient approximation (GGA) functional based on the Perdew-Burke-Ernzerhof (PBE) form (Blöchl 1994b; Perdew and Wang 1992). Owing to the fact that the dispersive forces are not well defined in the standard DFT and a non-local term needs to be added to account for these dispersive forces, the latest dispersion correction (D3) of Grimme throughout the calculations to correctly describe the adsorption energy and long range vdW interactions were employed (Grimme 2004). A kinetic energy cut-off of 500 eV for the plane-wave basis set was applied, with an energy convergence of 1.0×10^{-5} eV. For structural optimization, 0.02 eVÅ was taken as the force convergence criterion. A vacuum region of at least 10 Å was exploited to avoid the interaction between the adjacent layers. For the isolated MoS_2 monolayer, the first Brillouin zone integration was performed with Γ-centered 12 x 12 x 1 grid. As for the pristine WO_3 and WO_3/MoS_2 heterojunction, Γ-center 8 x 8 x 1 and 9 x 9 x 1 for geometry optimization and electronic structure calculations were used. In order to obtain accurate electronic structures, hybrid density functional calculations within the HSE06 approximation were performed. The contribution of exchange included the short-range part and long-range part in the HSE06 hybrid functional (Heyd et al. 2003). The short-range part of PBE exchange was weighted by 25 % Hartree-Fock exchange. To calculate the adsorption energy of H atom on various functionalized surfaces, a 3 x 3 x 1 supercell of MoS_2 and 2 x 2 x 1 supercell of WO_3 respectively were used. All calculations were performed using spin polarization.

6.3 Results and discussion

6.3.1 Morphological, chemical and structural characterization

XRD analysis was carried out to confirm the crystalline structure and composition of the as-synthesized photocatalysts. The clear and intense XRD patterns of pristine WO_3, MoS_2 and WO_3/MoS_2 nanocomposite are shown in Figure 6.1. The diffraction patterns of WO_3 are consistent with the hexagonal phase with lattice constants of a

= b = 7.30 Å, c = 3.90 Å as reported in literature (JCPDS card # 33-1387) (Zhang et al. 2014a). While the diffraction peaks of pristine MoS_2 were consistent with the hexagonal phase (JCPDS card # 37-1492) as reported in literature (Zeng et al. 2019a). In the case of WO_3/MoS_2 nanocomposite, the presence of diffraction peaks of both WO_3 and MoS_2 confirms that they are successfully produced.
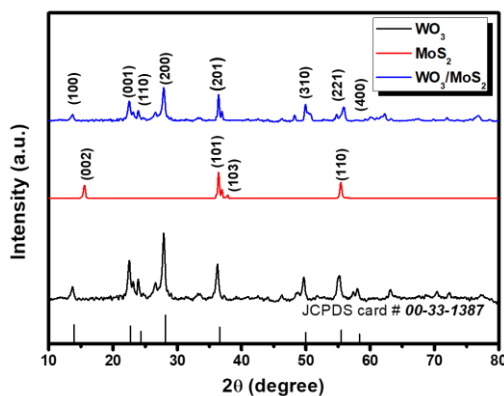
Figure 6.1: X-ray diffraction patterns of pristine WO_3, MoS_2 and WO_3/MoS_2 heterojunction photocatalysts.

FESEM micrographs of WO_3 obtained at two different magnifications are displayed in Figure 6.2a and 6.2b. An overview of the WO_3 particles spread uniformly with block-like morphology is evident from low magnification FESEM micrograph presented in Figure 6.2a. The magnified FESEM micrograph shown in Figure 6.2b confirms the formation of 2D WO_3 nanoblocks with widths of 0.8 - 1 μm and thicknesses of 60-100 nm. The absence of X-ray peaks of elements other than those corresponding to W and O in the EDS spectrum shown in Figure 6.2c indicates the purity of the as-synthesized WO_3 nanoblocks. On the other hand, Figure 6.2d and 6.2e represent the FESEM micrographs of the 2D MoS_2 obtained through hydrothermal method. FESEM analysis under both low and high magnifications shows the formation of 2D sheet-like structures of MoS_2 agglomerated into particles having diameters in the range of 100-150 nm. The absence of X-ray peaks of elements other than those corresponding to Mo and S in the EDS spectrum shown in Figure

6.2f indicates the purity of the as-synthesized MoS$_2$ nanosheets. FESEM micrographs of WO$_3$/MoS$_2$ nanocomposite presented in Figure 6.2g and 6.2h indicates a mixed morphology with MoS$_2$ nanosheets embedded over nanoblocks of WO$_3$. Magnified FESEM micrograph in Figure 6.2h clearly depicts the presence of MoS$_2$ nanosheets interconnected with WO$_3$ nanoblocks. EDS spectrum of WO$_3$/MoS$_2$ nanocomposite shown in Figure 6.2i, reveals the presence of elemental peaks corresponding to only W, O, Mo and S indicates the purity of the sample.
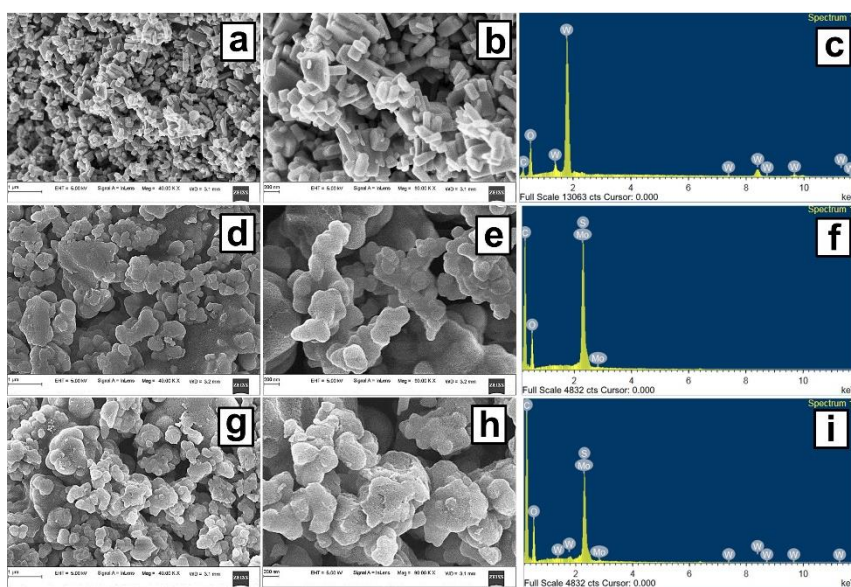
Figure 6.2: Morphological and chemical characterization of the as-synthesized WO$_3$, MoS$_2$ and WO$_3$/MoS$_2$ photocatalysts. FESEM micrographs under two different magnifications corresponding to (a, b) WO$_3$, (d, e) MoS$_2$ and (g, h) WO$_3$/MoS$_2$ photocatalysts. EDS spectrum corresponding to (c) WO$_3$, (f) MoS$_2$ and WO$_3$/MoS$_2$ composite

6.3.2 Optical properties

The optical properties were investigated through UV-Vis DRS for understanding the visible light absorption capability of the as-synthesized photocatalysts and for estimating their energy bandgap. DRS is related to the absorption coefficient by the Kubelka-Munk (K-M) function F(R) given by the Eq. (6.2)

86

$$F(R) = \frac{(1-R)^2}{2R} \qquad (6.2)$$

where reflectance $R = R_{sample}/R_{reference}$. MoS_2 physically appears as a black powder and has an absorption in the visible light region owing to its narrow bandgap. The DRS presented in Figure 6.3a indicates an absorption edge around 650 nm for MoS_2. On the other, pristine WO_3 shows an absorption edge at 440 nm. Figure 6.3b showing the plot of $[F(R)h\nu]^{1/2}$ versus $h\nu$ was used for deducing the corresponding bandgap energy of the as-synthesized photocatalysts by extrapolating the linear portion of the graph to $[F(R)h\nu]^{1/2} = 0$. As confirmed from the DRS data presented in Figure 6.4a, the energy bandgap of WO_3 decreased from 2.8 eV to 2.4 eV with the loading of MoS_2, indicating the improved visible light absorption capability of WO_3/MoS_2 composite photocatalyst.
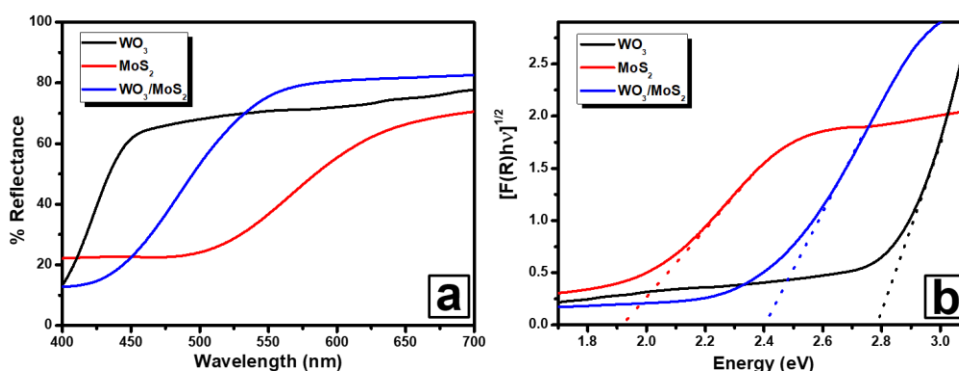
Figure 6.3: (a) UV-vis diffuse reflectance spectra of the as-synthesized WO_3, MoS_2 and WO_3/MoS_2 composite photocatalysts.

6.3.3 Geometry, structure and stability

Before analyzing the electronic properties of pristine MoS_2 and WO_3, full geometry relaxation of the atomic coordinates and lattice parameters are achieved. Both WO_3 and MoS_2 belong to hexagonal structures with P 6/mmm and P 6_3/mmc space groups respectively. The optimized lattice parameters and the bandgap of the relaxed monolayers calculated by HSE06 functional are summarized in Table 6.1 and agree well with the reported experimental and theoretical values (Zhang et al. 2019a; b). As for the structural

properties of isolated WO_3 and MoS_2 monolayers, the optimized Mo-S distance in MoS_2 monolayer is ca. 2.408 Å and W-O distance in WO_3 is ca. 1.93 Å respectively. Figure 6.4a and 6.4b show top views of monolayer MoS_2 and monolayer WO_3 with 3 x 3 lateral periodicity respectively. Figure 6.4c illustrates the geometric structure of WO_3/MoS_2 heterojunction where the lattice mismatch is not more than 1.3%. To further investigate the adsorption interaction between WO_3 and MoS_2 surface at the interface, the interfacial cohesive energy was obtained according to the following equation:

$$E_{Coh} = E_{WO3/MoS2} - E_{WO3} - E_{MoS2} \quad (6.3)$$

where $E_{WO3/MoS2}$, E_{WO3} and E_{MoS2} represent the total energy of the relaxed $E_{WO3/MoS2}$ heterojunction, isolated WO_3 and isolated MoS_2 respectively. The calculated cohesive energy was -0.81 eV for the entire model interface. The negative cohesive energy indicated that the WO_3/MoS_2 composite could form a stable interface and is energetically feasible.
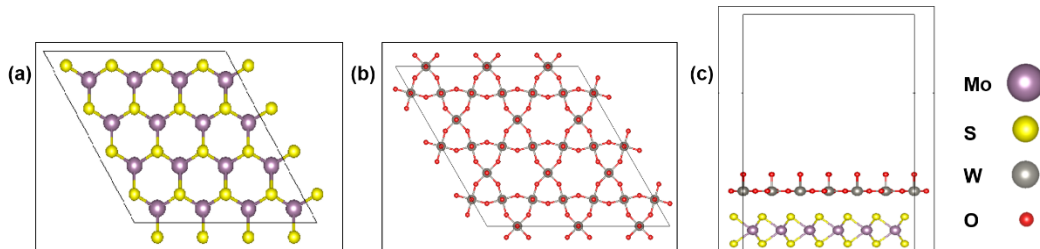
Figure 6.4: Optimized geometric structures of (a) MoS_2, (b) WO_3 and (c) WO_3/MoS_2 heterojunction.

Table 6.1 Optimized lattice parameters, calculated bandgaps, work functions and band edge positions of WO_3 and MoS_2 respectively.

System	Lattice parameter (Å)			Bandgap E_g (eV)	Work function ϕ (eV)	E_{VB} (eV)	E_{CB} (eV)
	a	b	c				
WO_3	7.298	7.298	3.899	3.0	6.13	3.59	0.59
MoS_2	3.16	3.16	12.29	1.75	4.76	1.69	-0.1

6.3.4 Band structure and density of states

To describe the interaction in the heterojunction more clearly, band structures and partial density of states (PDOS) for WO_3, MoS_2 and WO_3/MoS_2 heterojunction are simulated based on HSE06 functional and are illustrated in Figure 6.5a-c. Monolayer MoS_2 has a direct bandgap of 1.75 eV where the valence band maximum (VBM) and conduction band minimum (CBM) are located at K point. The simulated bandgap of WO_3 is direct with E_g of 3.0 eV at K point. The WO_3/MoS_2 heterojunction has a direct gap of 2.0 eV, with VBM and CBM also at K point. Therefore, heterojunction shows a direct bandgap that makes it beneficial for easier transfer of electrons from the VBM to the CBM. To explore the distribution of electrons and charge carrier migration path at the interface of heterojunction, the partial density of states of WO_3, MoS_2 and WO_3/MoS_2 heterojunction are plotted. Figure 6.5a illustrates how VBM of WO_3 is constructed by O (p) orbitals, while its CBM is comprised of W (d) orbital. From Figure 6.6b it is clear that both VB and CB of MoS_2 are almost equally occupied by the Mo (d) and S (p) orbitals respectively. For the heterojunction (see Figure 6.5c), the VBM is dominated by the Mo (d) and S (p) orbitals, while the CBM is composed of W (d) and O (p) orbitals. Under visible light irradiation, it is possible for the electrons in MoS_2 to be easily transferred into WO_3. Therefore, the introduction of MoS_2 monolayer is expected to improve the visible light photocatalytic performance of WO_3. This suggests that MoS_2 acts as a visible light sensitizer in the

heterojunction to successfully separate photogenerated electron-hole pairs *via* the interface charge transfer.
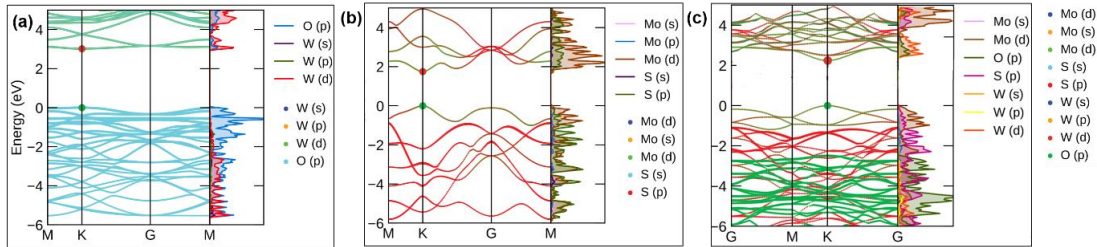
Figure 6.5: Calculated band structures and atom projected density of state plots of (a) WO₃ monolayer (b) MoS₂ monolayer and (c) WO₃/MoS₂ heterojunction within the hybrid HSE06 functional.

6.3.5 Work function analysis and charge density difference

The interaction of the MoS_2 and WO_3 layers indicates a significant charge transfer between them. To explore the charge, transfer process in the WO_3/MoS_2 heterojunction, three-dimensional charge density difference is plotted with an isosurface value of 0.0046 e/Å^3. yellow and cyan isosurfaces denote the charge accumulation and depletion, respectively. As seen from Figure 6.6a and 6.6b a high charge depletion occurred on the MoS_2 surface, resulting in hole-rich sites, while strong charge accumulation on the WO_3 surface, gave rise to electron-rich sites. Thus, holes accumulate in the MoS_2 region, and electrons accumulate in the region close to WO_3; therefore, electrons are expected to be excited from the MoS_2 to the surface of WO_3. Additionally, MoS_2 behaves as electron acceptor and actively take part in the transport of electrons participating in the oxidation-reduction reactions. This study revealed that the interaction at the semiconductor interface causes not only strong charge distribution in each component, but also significant interfacial charge transfers and separation of WO_3/MoS_2 heterojunction, which determine the mechanism of the enhanced photocatalytic performance.
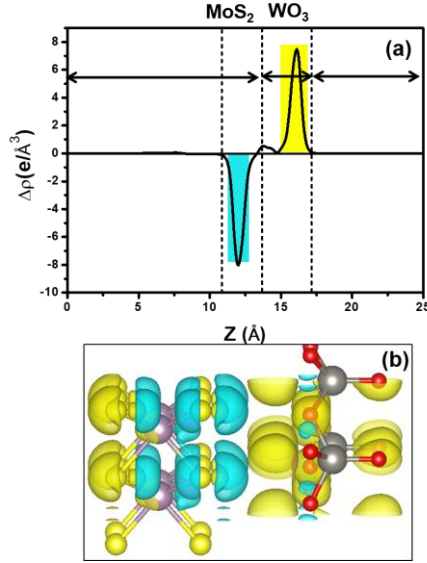
Figure 6.6: Charge density difference of WO_3/MoS_2 heterojunction within the hybrid HSE06 functional.

The difference in work function (Φ) between two semiconductors is necessary for inducing charge redistribution and forming a built-in electric field at the interface, which affects the photogenerated charge transfer process. Generally, work function can be defined as follows:

$$\Phi = E_{vac} - E_F \qquad (6.4)$$

where E_F is the Fermi energy, E_{vac} is the energy of a stationary electron in the vacuum nearby the surface. The vacuum energy is the averaged potential across the plane parallel to the WO_3/MoS_2 hetero-structure, which is 10 Å away from the nearest atomic layers of the hetero-structure in the supercell. The planar averaged electrostatic potential plots of MoS_2, WO_3 and WO_3/MoS_2 heterojunction along the Z-direction are displayed in Figure 6.7a-c with simulated work functions being 4.76 eV, 6.13 eV and 5.25 eV respectively. The Fermi level of MoS_2 is higher than that of WO_3 as displayed in Figure 6.8a and 6.8b. In the present case, when WO_3 comes in contact with MoS_2, owing to lower work function of MoS_2 in comparison to WO_3, the electrons of MoS_2 transfer to WO_3 until the Fermi levels of these

semiconductors are aligned. Owing to the electron transfer, a built-in electric field directed from MoS_2 to WO_3 surface will be established when an equalized E_F is reached by the two individual components. Therefore, the existence of interfacial built-in potential is beneficial to enhance the separation of photogenerated electron-hole pairs, thereby inhibiting their recombination rate to improve the photocatalytic activity of the heterojunction. Thus, the occurrence of built-in potential at the WO_3/MoS_2 heterojunction interface may be one of the main reasons behind the enhancement of the photocatalytic performance in the heterostrcture.
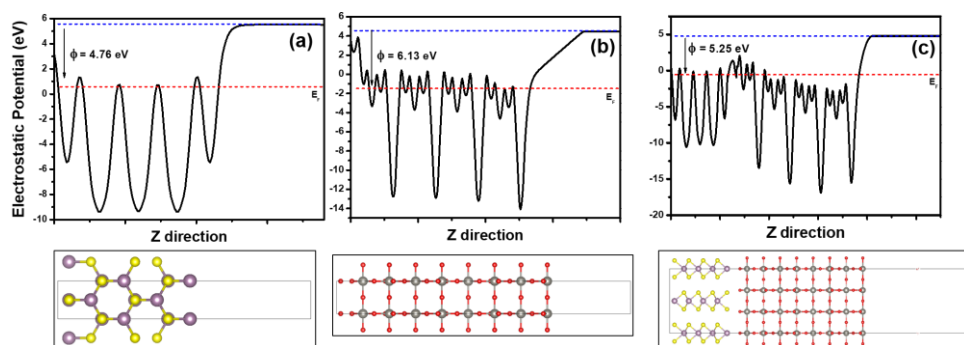
Figure 6.7: The work function of (a) MoS_2, (b) WO_3 and (c) WO_3/MoS_2 heterojunction. The red and blue lines denote the Fermi level and the vacuum energy level respectively.

6.3.6 Visible light driven photocatalytic degradation of methylene blue

The photocatalytic activity of the as-prepared samples evaluated by their capability in degrading MB under visible light irradiation is presented in Figure 6.8a and 6.8b. UV-Visible absorption spectra presented in Figure 6.8a exhibiting the steady and gradual decrease in the absorption peak of MB centered at 665 nm with respect to the increase in the visible light irradiation time is indicative of the reduction in its concentration. A plot depicting the variation in the concentration of MB with respect to the visible light irradiation time in the presence of various photocatalysts is presented in Figure 6.8b. As observed from Figure 6.8b, the negligible photodegradation of MB in the absence of any photocatalyst indicates its high chemical stability. In pristine WO_3 the degradation of MB was limited to just 85% even after 120 min of visible light irradiation owing to their large bandgap energy. In

contrast, the photodegradation of MB under the same conditions in the presence of pristine MoS_2 improved by little with its concentration dropping to 12% after 100 min of visible light irradiation. Subsequently, the concentration of MB decreased to 10% and over 90% photodegradation was achieved in just 60 min in the presence of WO_3/MoS_2 nanocomposite under visible light irradiation.
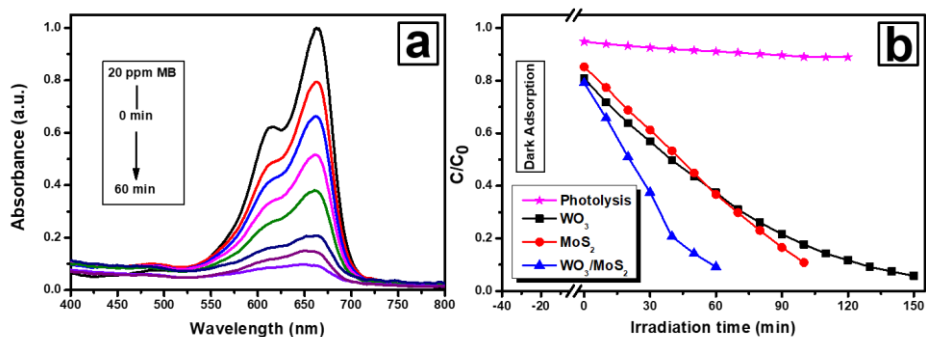
Figure 6.8: (a) UV-vis absorption spectra depicting the visible light induced photodegradation of methylene blue in the presence of WO_3/MoS_2 photocatalyst (b) Plot depicting the time dependent photodegradation of methylene blue under visible light irradiation in the presence of as-synthesized WO_3, MoS_2 and WO_3/MoS_2 as photocatalysts.

The rate of photodegradation of MB were computed using the pseudo-first-order kinetics given by the equation,

$$\ln (C_0/C_t) = k_{app}\, t \qquad (6.5)$$

where C_0, C_t and k_{app} correspond to the initial concentration, the concentration at time t and the apparent pseudo-first-order rate constant (k_{app}, min^{-1}), respectively (Wang et al. 2013). Plots of the pseudo-first-order reaction kinetics corresponding to as-synthesized photocatalysts are presented in Figure 6.9. Rate constant for the photodegradation of MB that were determined from the experimental data are 0.0909, 0.3281 and 0.7635 min^{-1} for WO_3, MoS_2 and WO_3/MoS_2 composite respectively. It is observed that the values of degradation efficiency for the as-synthesized photocatalysts are consistent with the kinetic

data.
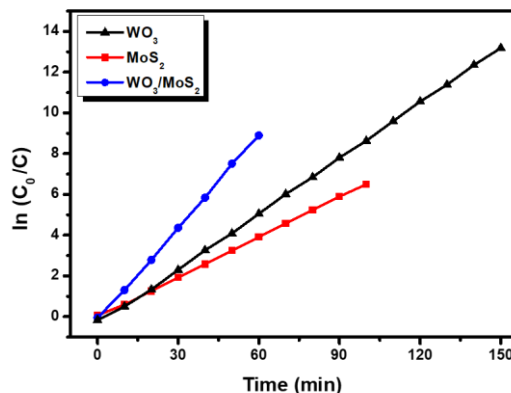
Figure 6.9: Pseudo first-order reaction kinetics plot of methylene blue photodegradation using WO_3, MoS_2 and WO_3/MoS_2 as photocatalysts.

6.3.7 Hydrogen evolution reaction

The photocatalytic water splitting can be divided into two half-cell reactions: Hydrogen evolution reaction (HER) and oxygen evolution reaction (OER). The two mechanisms namely the Volmer-Tafel and Volmer-Heyrovsky are needed to achieve HER (Benck et al. 2014). In the Volmer reaction, surface adsorbed hydrogen is formed through reduction of protons, *viz.* $H^+ + e^- \rightarrow H_{ads}$. Volmer step is subsequently followed by Tafel or Heyrovsky step to complete the HER. In Volmer-Tafel reaction mechanism, a hydrogen molecule (H_2) is formed when two adjacent adsorbed hydrogen atoms combine over the electrode surface $H_{ads} + H_{ads} \rightarrow H_2$. While in Volmer-Heyrovsky reaction, a proton present in water reacts with surface adsorbed hydrogen to generate H_2 *viz.* $H_{ads} + H^+_{(aq)} + e^- \rightarrow H_2$ (Tsai et al. 2015). Thus, both the reaction mechanisms reveal that the adsorption energy of the hydrogen atom plays a critical role in determining the catalytic activity over the surface of the catalyst (Koper 2011; Nørskov et al. 2005). Also, H_{ads} is related to the adsorption free energy (ΔG_H) by the following equation:

$$\Delta G_H = \Delta E_{ads} + \Delta E_{ZPE} + T\Delta S_H \qquad (6.6)$$

where E_{ads} is the adsorption energy, ΔE_{ZPE} is the zero-point energy difference of H_2 in the adsorbed and gas phase state with its values ranging from 0.01-0.04 eV. T is the temperature in K, ΔS_H is the change in the entropy between hydrogen in the adsorbed and gas phase and $\Delta S_H = \frac{1}{2}\Delta S^0_{H2}=0.2$ eV, where ΔS^0_{H2} is the entropy of H_2 in gas phase at standard conditions (Mir et al. 2016). Thus, the equation reduces to $\Delta G_H = \Delta E_{ads} + 0.24$ eV taking into consideration the values of ΔE_{ZPE} and ΔS_H. For an optimal HER catalyst, $\Delta G_H \simeq 0$ eV and hence the ΔE_{ads} should be of the order of -0.24 eV, where the binding strength of hydrogen is neither too strong nor too weak obeying the Sabatier principle (Seh et al. 2017). The adsorption energy of hydrogen was calculated according to the following equation:

$$\Delta E_{ads}=E_{S+nH} - E_S - n/2H_2 \quad (6.7)$$

here, E_{S+nH} and E_S represents the calculated total energies of the system with and without adsorbed hydrogen respectively. Here n is the number of hydrogen atoms, in the present case n=1. Since adsorption of H can be done at different sites, the H atom was initially set on-top position of the semiconductor surface and its atomic position was allowed to relax without any constraints along either x, y and z axes being imposed over it. The atomic positions of the rest of the atoms were also allowed to relax keeping the interlayer distance fixed at 10 Å. The final positions of the H atom after the atomic relaxation of all the above-mentioned systems are represented in Figure 6.10. The calculated ΔE_{ads} and ΔG_H for MoS_2, WO_3 and WO_3/MoS_2 are presented in Table 2. Using ΔG_H as an indicator for HER catalytic activity of the systems investigated in this study, the calculated ΔE_{ads} ought to be in the order of -0.2 eV. From the calculations, WO_3/MoS_2 heterojunction has ΔE_{ads} within this optical catalytic activity range. This indicated that the formation of heterojunction can improve the HER activity significantly.
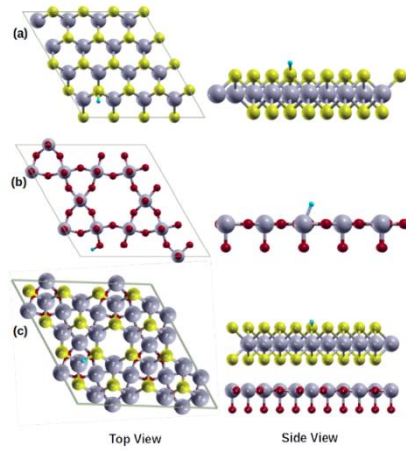
Figure 6.10: Final calculated geometry of H adsorbed on (a) MoS_2, (b) WO_3 and (c) WO_3/MoS_2 heterojunction.

6.3.8 Proposed photocatalytic mechanism

The mechanism of photocatalysis depends mainly on the generation, separation, transfer and participation of photogenerated charge carriers during the process of photocatalytic water splitting and photodegradation of organic pollutants. To interpret the participation of photoinduced charge carriers on the recombination rate and redox reaction of charge carriers, the band edge positions of MoS_2, WO_3 and WO_3/MoS_2 heterojunction were determined based on the following equations:

$$E_{VB} = \chi - E_e + 1/2\ E_g \qquad (6.8)$$

$$E_{CB} = E_{VB} - E_g \qquad (6.9)$$

here E_g represents the bandgap of the system, E_e is the energy of free electrons in the hydrogen scale (4.5 eV), E_{VB}, and E_{CB} are the VB and CB edge potentials, respectively (Opoku et al. 2018). The χ values of WO_3 and MoS_2 are 6.59 and 5.32 respectively (Xu and Schoonen 2000). The calculated CB and VB positions of WO_3 and MoS_2 are presented in Table 6.1.

If WO_3 and MoS_2 can form a conventional electron-hole separation process, the electrons accumulated in the CB of MoS_2 tend to move to the CB of WO_3 as the CB position of MoS_2 is more negative with respective to WO_3. Meanwhile, the holes present in the VB of WO_3

will migrate to the VB of MoS_2 under visible light irradiation, as the VB position of WO_3 is more positive compared to MoS_2. Subsequently, the heterojunction forms a type-II staggered band alignment, which favors for the separation and transfer of photogenerated charge carriers. However, the photoinduced electrons present on the CB of WO_3 cannot reduce O_2 into superoxide anion radical ($^{\bullet}O^{2-}$) as their CB position of 0.59 eV is less negative with reference to the potential required for O_2 generation ($O_2/^{\bullet}O_2- = -0.33$ eV vs. NHE). In addition, the VB potential of 1.69 eV for MoS_2 is lower compared to the $H_2O/^{\bullet}OH$ redox potential (2.68 eV vs. NHE) signifying that the photogenerated holes on the VB of MoS_2 cannot oxidize the adsorbed water molecules to form hydroxyl radical ($^{\bullet}OH$). Hence if the separation and transfer of the photoinduced charge carriers in the WO_3/MoS_2 heterojunction occurs via the conventional heterojunction process, the formation of $^{\bullet}O^{2-}$ and $^{\bullet}OH$ reactive species are not favorable, resulting in lower photocatalytic activity. Moreover, the photoinduced electrons on the CB of WO_3 cannot reduce H^+ in the water to generate H_2 gas owing to the CB position of WO_3 being lower than the H^+/H_2O (0 V vs. NHE) potential. However, the holes in the VB of MoS_2 can produce O_2 gas from water due to its VB potential being more positive compared to O_2/H_2O (1.23 V vs. NHE) potential.

Based on the above discussion, the WO_3/MoS_2 heterojunction follows a typical Z-scheme charge transfer system rather than the conventional system and a tentatively possible mechanism of the charge separation is proposed to explain the improved photocatalytic performance of the heterojunction as shown in Figure 6.11.
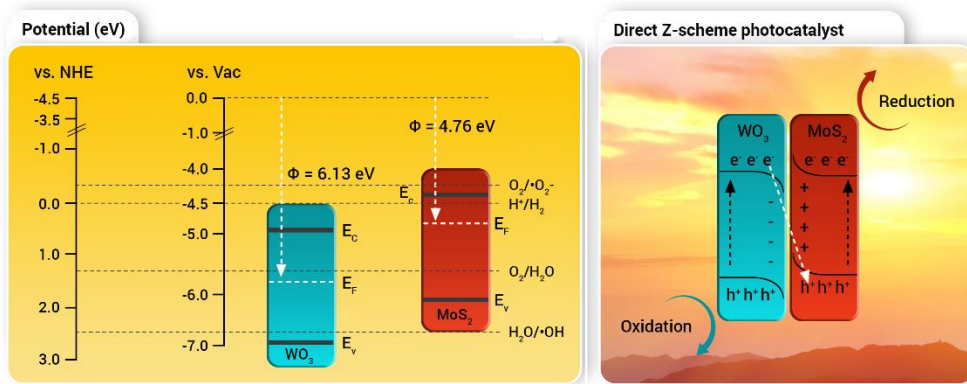
Figure 6.11: Proposed Z-scheme charge transfer mechanism for the enhanced photocatalytic performance over WO_3/MoS_2 heterojunction.

In the direct Z-scheme charge transfer process, the photogenerated electrons in the CB of WO_3 are migrated to the VB of MoS_2. The more positive VB potential of WO_3 (3.59 eV) compared to the $H_2O/{}^{\bullet}OH$ potential can oxidize the water molecules to form ${}^{\bullet}OH$ radicals. Similarly, ${}^{\bullet}O_2{}^{-}$ radicals are produced over more negative CB of MoS_2. Thus, the generation of these reactive species may induce a higher redox ability in the heterojunction, which enhances its photocatalytic activity in comparison to the pristine photocatalysts. The band alignment of WO_3/MoS_2 heterojunction with reference to the standard hydrogen electrode shows that the MoS_2 CB potential is more negative compared to the H^+/H_2 and has ability to reduce H^+ to H_2. In addition, the VB potential of WO_3 is more positive compared to the O_2/H_2O and can easily generate ${}^{\bullet}O_2{}^{-}$ radicals. Comparing the relative band edges of WO_3 and MoS_2 to the redox potentials, the WO_3/MoS_2 heterojunction forms a typical Z-scheme photocatalyst for the overall water splitting process. Owing to which, the energy band edges of MoS_2 with higher Fermi level are tend to bend upwards continuously towards the interface, while those in WO_3 with lower Fermi level are bended downwards towards the interface. Thus, the CB electrons in WO_3 are allowed to flow freely while the holes are confined in the VB. Furthermore, since the energy band of MoS_2 is bended upwards, holes in the VB can be easily migrated towards the interface. Although, there is movement of photogenerated electrons and holes towards the interface they cannot flow into the energy bands of the other semiconductors, and hence they can only recombine with each other at the interface. On the other hand, the CB electrons of MoS_2 and VB holes of WO_3 stay in their primary energy bands to take part in photocatalytic reactions. Thus WO_3/MoS_2 composite forms a direct Z-scheme photocatalyst.

6.4 Summary

In this study, the various experimental results and first-principles calculations with a new and interesting discussion to explain the photocatalytic activity of WO_3/MoS_2

heterojunction in the degradation of organic pollutants and hydrogen evolution reaction were studied. The work function and the charge density difference of the heterojunction indicated that it is a Z-scheme charge transfer mechanism. Under light illumination, the built-in electric field accelerates the transfer of photogenerated electrons in the CB of WO_3 into the VB of MoS_2. And the photogenerated electrons and holes gathering on the different semiconductor surfaces efficiently prolong their lifetime and enhance the photocatalytic activity. Using dispersion corrected DFT, the catalytic activity towards HER has been investigated. The calculated ΔG_H in the case of heterojunction was found to be very close to the thermoneutral point $\Delta G_H = 0$ eV indicating that its activity towards HER was significantly improved owing to the formation of Z-scheme heterojunction. WO_3/MoS_2 heterojunction synthesized *via* hydrothermal approach exhibited good performance towards photodegradation of methylene blue under visible light irradiation. The enhanced photocatalytic performance is attributed to the efficient charge separation and transfer across the heterojunction The advantages of the insights gained through this work are two-fold. First, the mechanism and origin of the photocatalytic activity can be rationalized. Second, it is expected to provide new insights that can contribute to the rational design of new materials for multifunctional applications.

CHAPTER 7

CONCLUSION AND FUTURE SCOPE

This chapter summarizes the main results of the investigation presented in the thesis. Possible future works in this direction are also suggested at the end.

7.1 Conclusion

In the 21st century, with the ever-increasing energy demand and growing environmental concerns, the efficient utilization of sunlight for the production of clean energy and environmental remediation is becoming an important global issue. Towards this end, photocatalysis as an economic, renewable, clean, and safe technology for realizing the solar-to-chemical energy conversion has attracted increasing attention.

Among the available photoactive TMCs, cadmium sulfide is of great interest to researchers. It possesses a narrower bandgap of 2.4 eV for visible light response and more suitable band edge positions for hydrogen production and removal of organic pollutants. Importantly, CdS can be surface-assembled with other semiconductor photocatalysts to form a heterojunction, thereby enabling the activity and selectivity of photocatalytic reactions.

At first, CdS nanostructures with 1D, 2D, and 3D morphology as visible-light-responsive photocatalysts were synthesized and verified the influence of morphology on the photocatalytic activity towards the degradation of erioglaucine and generation of hydrogen under visible light irradiation. Among the synthesized photocatalysts, 3D CdS exhibited enhanced photocatalytic efficiency in the photodegradation of erioglaucine as well as for hydrogen generation. Major factors responsible for the enhanced photocatalytic efficiency of 3D CdS were, (i) hexagonal crystal structure, (ii) high crystallinity with single-crystalline nature that hindered bul^k electron-hole pair recombination, and (iii) hierarchical 3D structure assembled with many thin nanowires containing numerous photocatalytically active sites that facilitated the mobility of photogenerated charge carriers for the reaction with surface adsorbed molecules. The role of scavengers and cyclic photodegradation studies for understanding the stability of 3D CdS against photocorrosion was discussed. Furthermore, the surprising effect of sonication in the enhancement of photocatalytic activity has been illustrated.

Although CdS has emerged as one of the most classical semiconductor photocatalysts, however bare CdS exhibits poor photocatalytic activity owing to the rapid recombination

of photogenerated charge carriers. In this regard, combining CdS with other suitable semiconductor photocatalysts to form heterojunctions is an effective strategy for driving the spatial separation of electrons and holes and reducing the possibility of charge carrier recombination. Thus, g-C$_3$N$_4$/CdS heterojunction were synthesized through the hydrothermal method and were employed as photocatalysts in the degradation of methylene blue dye molecules under visible light irradiation. Among the synthesized photocatalysts, g-C$_3$N$_4$/CdS heterojunction exhibited enhanced photocatalytic efficiency for the degradation of 20 ppm MB. The superior photocatalytic performance of g-C$_3$N$_4$/CdS was attributed to the reduced rate of recombination of the photogenerated electron-hole pairs, as tracked from photoluminescence spectroscopy.

To develop efficient semiconductor-based photocatalyst materials for water splitting as well as for the photodegradation of organic pollutants in water, the optical, electronic, and structural properties of materials have to be carefully investigated. First-principles approaches have been a useful tool in providing a deeper understanding of photocatalysis, explaining experimental data as well as predicting novel semiconductor photocatalysts materials with superior performance. In the present section the electronic structures of the CdS (110), CdSe (110) and CdS/CdSe heterojunction were investigated on the basis of hybrid-DFT method. Calculated band structure and atom projected DOS confirm that the CdS/CdSe forms a type-II heterojunction. The proper band edge positions and their alignment with respect to the NHE were determined from the calculated bandgap and work function for each surface. The band edge positions of both the semiconductors changed with the Fermi level while formation of heterojunction and a large band offset both in valence and conduction band was observed. The existence of an internal electric field near the interface due to large band offsets will facilitate the charge separation across the CdS/CdSe interface, which in turn reduced the recombination of electron–hole pairs. The charge carrier mobility is also improved in the heterojunction and the band alignment of the system is such that both photoreduction and photooxidation processes associated with water splitting are energetically feasible. The results indicated that the CdS/CdSe

heterojunction may have wide application in photocatalysis for pollutant degradation and water splitting.

Recently, noble-metal-free MoS_2 (belonging to TMCs family) has attracted attention owing to its high mobility of charge carriers and excellent optical absorption property. Various experimental results and first principles calculations with a new and interesting discussion to explain the photocatalytic activity of WO_3/MoS_2 heterojunction in degradation of organic pollutant and hydrogen evolution reaction were explained. The structural, electronic, optical and charge transfer properties of the heterojunction were investigated using DFT calculations. Using dispersion corrected DFT, the catalytic activity towards HER has been investigated. The calculated ΔG_H in case of heterojunction were found to be very close to the thermo neutral point $\Delta G_H = 0$ eV indicating that its activity towards HER was significantly improved owing to the formation of Z-scheme heterojunction. In addition, WO_3/MoS_2 heterojunction synthesized *via* hydrothermal approach exhibited good performance towards photodegradation of methylene blue under visible light irradiation. The enhanced photocatalytic performance is attributed to the efficient charge separation and transfer across the heterojunction. The advantages of the insights gained through this work are two-fold. First, the mechanism and origin of the photocatalytic activity can be rationalized. Second, it is expected to provide new insights that can contribute to the rational design of new materials for multifunctional applications. The study provides an in-depth knowledge of the fundamental mechanism and understanding of the interfacial electron transfer process that is useful to aid an experimentalist to design and fabricate novel photocatalysts to expand their applicability.

7.2 Future scope

In the present study, transition metal chalcogenide photocatalysts for applications in photodegradation of organic pollutants and for hydrogen generation were successfully designed. Although considerable progress about the understanding of the optical and electronic properties of these semiconductors has received much attention, research in this field is still at the fundamental stage and further improvements are needed. The design of

first-principles approaches and software packages allow experimentalists to fabricate existing and new materials. However, the major challenges involve the incorporation of first-principles calculations, databases, and atomistic modeling into a single system, so that the realization of efficient design of hybrid materials, as well as visualizing their synthesis reactions can be achieved.

The photocatalytic performance of the photocatalysts can be also evaluated towards wide range of applications. Among them carbon dioxide reduction, and oxygen evolution reaction will be focus of the work in the near future.

References

Abbood, H. A., Alabadi, A., Al-Hawash, A. B., Abbood, A. A., and Huang, K. (2020). "Square CdS Micro/Nanosheets as Efficient Photo/Piezo-bi-Catalyst for Hydrogen Production." *Catal Lett*, 150(11), 3059–3070.

Ahmed, B., Kumar, S., Kumar, S., and Ojha, A. K. (2016). "Shape induced (spherical, sheets and rods) optical and magnetic properties of CdS nanostructures with enhanced photocatalytic activity for photodegradation of methylene blue dye under ultra-violet irradiation." *Journal of Alloys and Compounds*, 679, 324–334.

Al Balushi, B. S. M., Al Marzouqi, F., Al Wahaibi, B., Kuvarega, A. T., Al Kindy, S. M. Z., Kim, Y., and Selvaraj, R. (2018). "Hydrothermal synthesis of CdS sub-microspheres for photocatalytic degradation of pharmaceuticals." *Applied Surface Science*, 457, 559–565.

Archer, E., Petrie, B., Kasprzyk-Hordern, B., and Wolfaardt, G. M. (2017). "The fate of pharmaceuticals and personal care products (PPCPs), endocrine disrupting contaminants (EDCs), metabolites and illicit drugs in a WWTW and environmental waters." *Chemosphere*, 174, 437–446.

Ashokkumar, M. (1998). "An overview on semiconductor particulate systems for photoproduction of hydrogen." *International Journal of Hydrogen Energy*, 23(6), 427–438.

Azadi, S., and Kühne, Th. D. (2012). "Absence of metallization in solid molecular hydrogen." *Jetp Lett.*, 95(9), 449–453.

Babu, B., Kim, J., and Yoo, K. (2020). "Improved solar light-driven photoelectrochemical performance of cadmium sulfide-tin oxide quantum dots core-shell nanorods." *Materials Letters*, 274, 128005.

Bae, Y.-S., Yazaydın, A. Ö., and Snurr, R. Q. (2010). "Evaluation of the BET Method for Determining Surface Areas of MOFs and Zeolites that Contain Ultra-Micropores." *Langmuir*, 26(8), 5475–5483.

Bai, S., Wang, L., Chen, X., Du, J., and Xiong, Y. (2015). "Chemically exfoliated metallic MoS2 nanosheets: A promising supporting co-catalyst for enhancing the photocatalytic performance of TiO2 nanocrystals." *Nano Research*, 8(1), 175–183.

Bai, Z., Bai, Z., Gao, T., Bai, Z., and Zhu, Y. (2019). "Preparation effects on the morphology and photocatalytic properties of carbon nitride nanotubes." *Results in Physics*, 13, 102254.

Bao, N., Shen, L., Takata, T., and Domen, K. (2008). "Self-Templated Synthesis of Nanoporous CdS Nanostructures for Highly Efficient Photocatalytic Hydrogen Production under Visible Light." *Chem. Mater.*, 20(1), 110–117.

Benck, J. D., Hellstern, T. R., Kibsgaard, J., Chakthranont, P., and Jaramillo, T. F. (2014). "Catalyzing the Hydrogen Evolution Reaction (HER) with Molybdenum Sulfide Nanomaterials." *ACS Catal.*, 4(11), 3957–3971.

Bera, R., Dutta, A., Kundu, S., Polshettiwar, V., and Patra, A. (2018). "Design of a CdS/CdSe Heterostructure for Efficient H2 Generation and Photovoltaic Applications." *J. Phys. Chem. C*, 122(23), 12158–12167.

Bera, R., Kundu, S., and Patra, A. (2015). "2D Hybrid Nanostructure of Reduced Graphene Oxide–CdS Nanosheet for Enhanced Photocatalysis." *ACS Appl. Mater. Interfaces*, 7(24), 13251–13259.

Bhat, K. S., Shenoy, S., Nagaraja, H. S., and Sridharan, K. (2017). "Porous cobalt chalcogenide nanostructures as high performance pseudo-capacitor electrodes." *Electrochimica Acta*, 248, 188–196.

Bie, C., Fu, J., Cheng, B., and Zhang, L. (2018). "Ultrathin CdS nanosheets with tunable thickness and efficient photocatalytic hydrogen generation." *Applied Surface Science*, 462, 606–614.

Blöchl, null. (1994a). "Projector augmented-wave method." *Phys. Rev., B Condens. Matter*, 50(24), 17953–17979.

Blöchl, P. E. (1994b). "Projector augmented-wave method." *Phys. Rev. B*, 50(24), 17953–17979.

Bridewell, V. L., Alam, R., Karwacki, C. J., and Kamat, P. V. (2015). "CdSe/CdS Nanorod Photocatalysts: Tuning the Interfacial Charge Transfer Process through Shell Length." *Chem. Mater.*, 27(14), 5064–5071.

Buhro, W. E., and Colvin, V. L. (2003). "Semiconductor nanocrystals: Shape matters." *Nature Materials*, 2(3), 138–139.

Burda, C., Chen, X., Narayanan, R., and El-Sayed, M. A. (2005). "Chemistry and Properties of Nanocrystals of Different Shapes." *Chem. Rev.*, 105(4), 1025–1102.

Calloway, D. (1997). "Beer-lambert law." *J. Chem. Educ*, 74(7), 744.

Cao, S.-W., Yuan, Y.-P., Barber, J., Loo, S. C. J., and Xue, C. (2014). "Noble-metal-free g-C3N4/Ni(dmgH)2 composite for efficient photocatalytic hydrogen evolution under visible light irradiation." *Applied Surface Science*, Photocatalytic materials for energy and environmental applications, 319, 344–349.

Caudillo-Flores, U., Muñoz-Batista, M. J., Kubacka, A., Zárate-Medina, J., Cortés, J. A., and Fernández-García, M. (2018). "Measuring and interpreting quantum efficiency of acid blue 9 photodegradation using TiO2-based catalysts." *Applied Catalysis A: General*, 550, 38–47.

Chai, B., Xu, M., Yan, J., and Ren, Z. (2018). "Remarkably enhanced photocatalytic hydrogen evolution over MoS2 nanosheets loaded on uniform CdS nanospheres." *Applied Surface Science*, 2nd International Workshop on Graphene and C3N4-based Photocatalysts, 430, 523–530.

Chang, F., Li, C., Luo, J., Xie, Y., Deng, B., and Hu, X. (2015). "Enhanced visible-light-driven photocatalytic performance of porous graphitic carbon nitride." *Applied Surface Science*, Graphene and C3N4-based Photocatalysts, 358, 270–277.

Chang, F., Xie, Y., Li, C., Chen, J., Luo, J., Hu, X., and Shen, J. (2013). "A facile modification of g-C3N4 with enhanced photocatalytic activity for degradation of methylene blue." *Applied Surface Science*, 280, 967–974.

Chauhan, H., Kumar, Y., Dana, J., Satpati, B., Ghosh, H. N., and Deka, S. (2016). "Photoinduced ultrafast charge separation in colloidal 2-dimensional CdSe/CdS-Au hybrid nanoplatelets and corresponding application in photocatalysis." *Nanoscale*, 8(34), 15802–15812.

Chen, J., Wu, X.-J., Yin, L., Li, B., Hong, X., Fan, Z., Chen, B., Xue, C., and Zhang, H. (2015). "One-pot Synthesis of CdS Nanocrystals Hybridized with Single-Layer Transition-Metal Dichalcogenide Nanosheets for Efficient Photocatalytic Hydrogen Evolution." *Angewandte Chemie*, 127(4), 1226–1230.

Chen, J., Yu, D., Liao, W., Zheng, M., Xiao, L., Zhu, H., Zhang, M., Du, M., and Yao, J. (2016). "WO3–x Nanoplates Grown on Carbon Nanofibers for an Efficient Electrocatalytic Hydrogen Evolution Reaction." *ACS Appl. Mater. Interfaces*, 8(28), 18132–18139.

Chen, L., Xu, Y., and Chen, B. (2019). "In situ photochemical fabrication of CdS/g-C3N4 nanocomposites with high performance for hydrogen evolution under visible light." *Applied Catalysis B: Environmental*, 256, 117848.

Chen, W., Wang, Y., Liu, M., Gao, L., Mao, L., Fan, Z., and Shangguan, W. (2018). "In situ photodeposition of cobalt on CdS nanorod for promoting photocatalytic hydrogen production under visible light irradiation." *Applied Surface Science*, 444, 485–490.

Chen, X., Shen, S., Guo, L., and Mao, S. S. (2010). "Semiconductor-based Photocatalytic Hydrogen Generation." *Chem. Rev.*, 110(11), 6503–6570.

Chen, Y.-C., and Smirniotis, P. (2002). "Enhancement of Photocatalytic Degradation of Phenol and Chlorophenols by Ultrasound." *Ind. Eng. Chem. Res.*, 41(24), 5958–5965.
Cheng, L., Xiang, Q., Liao, Y., and Zhang, H. (2018). "CdS-Based photocatalysts." *Energy & Environmental Science*, 11(6), 1362–1391.

Comninellis, C., Kapalka, A., Malato, S., Parsons, S. A., Poulios, I., and Mantzavinos, D. (2008). "Advanced oxidation processes for water treatment: advances and trends for R&D." *J. Chem. Technol. Biotechnol.*, 83(6), 769–776.

Cui, X., Zhou, Y., Wu, J., Ling, S., Zhao, L., Zhang, J., Wang, J., Qin, W., and Zhang, Y. (2020). "Controlling Pt co-catalyst loading in a WO3 quantum dot and MoS2 nanosheet composite Z-scheme system for enhanced photocatalytic H2 evolution." *Nanotechnology*, 31(18), 185701.

Dai, H., Wang, T. Y., and Li, M. C. (2016). "Spotlight on ultrasonic fracture behaviour of nanowires: their size-dependent effect and prospect for controllable functional modification." *RSC Adv.*, 6(76), 72080–72085.

Dai, Z., Geng, H., Wang, J., Luo, Y., Li, B., Zong, Y., Yang, J., Guo, Y., Zheng, Y., Wang, X., and Yan, Q. (2017). "Hexagonal-Phase Cobalt Monophosphosulfide for Highly Efficient Overall Water Splitting." *ACS Nano*, 11(11), 11031–11040.

Daneshvar, N., Salari, D., Niaei, A., and Khataee, A. R. (2006). "Photocatalytic degradation of the herbicide erioglaucine in the presence of nanosized titanium dioxide: comparison and modeling of reaction kinetics." *J Environ Sci Health B*, 41(8), 1273–1290.

Deng, F., Lu, X., Zhong, F., Pei, X., Luo, X., Luo, S., Dionysiou, D. D., and Au, C. (2016). "Fabrication of 2D sheet-like BiOCl/carbon quantum dot hybrids via a template-free coprecipitation method and their tunable visible-light photocatalytic activities derived from different size distributions of carbon quantum dots." *Nanotechnology*, 27(6), 065701.

Devipriya, S., and Yesodharan, S. (2005). "Photocatalytic degradation of pesticide contaminants in water." *Solar Energy Materials and Solar Cells*, 86(3), 309–348.

Di, T., Xu, Q., Ho, W., Tang, H., Xiang, Q., and Yu, J. (2019). "Review on Metal Sulphide-based Z-scheme Photocatalysts." *ChemCatChem*, 11(5), 1394–1411.

Di, T., Zhu, B., Zhang, J., Cheng, B., and Yu, J. (2016). "Enhanced photocatalytic H2 production on CdS nanorod using cobalt-phosphate as oxidation cocatalyst." *Applied Surface Science*, 389, 775–782.

Dong, G., Qiu, P., Meng, F., Wang, Y., He, B., Yu, Y., Liu, X., and Li, Z. (2020). "Facile synthesis of sulfur-doped polymeric carbon nitride/MoS2 face-to-face heterojunction for highly efficient photocatalytic interfacial charge separation." *Chemical Engineering Journal*, 384, 123330.

Dong, S., Feng, J., Fan, M., Pi, Y., Hu, L., Han, X., Liu, M., Sun, J., and Sun, J. (2015). "Recent developments in heterogeneous photocatalytic water treatment using visible light-responsive photocatalysts: a review." *RSC Advances*, 5(19), 14610–14630.

Durán-Álvarez, J. C., Del Angel, R., Ramírez-Ortega, D., Guerrero-Araque, D., and Zanella, R. (2020). "An alternative method for the synthesis of functional Au/WO3 materials and their use in the photocatalytic production of hydrogen." *Catalysis Today*, SI: 5th LACP3 2017, 341, 49–58.

El-Sayed, M. A. (2004). "Small Is Different: Shape-, Size-, and Composition-Dependent Properties of Some Colloidal Semiconductor Nanocrystals." *Acc. Chem. Res.*, 37(5), 326–333.

Fan, Q., Huang, Y., Zhang, C., Liu, J., Piao, L., Yu, Y., Zuo, S., and Li, B. (2016a). "Superior nanoporous graphitic carbon nitride photocatalyst coupled with CdS quantum

dots for photodegradation of RhB." *Catalysis Today*, Catalysis promoting the development of chemical industry: A special issue dedicated to Tianjin University's 120th anniversary, 264, 250–256.

Fan, X., Zhang, L., Wang, M., Huang, W., Zhou, Y., Li, M., Cheng, R., and Shi, J. (2016b). "Constructing carbon-nitride-based copolymers via Schiff base chemistry for visible-light photocatalytic hydrogen evolution." *Applied Catalysis B: Environmental*, 182, 68–73.

Farner Budarz, J., Turolla, A., Piasecki, A. F., Bottero, J.-Y., Antonelli, M., and Wiesner, M. R. (2017). "Influence of Aqueous Inorganic Anions on the Reactivity of Nanoparticles in TiO2 Photocatalysis." *Langmuir*, 33(11), 2770–2779.

Fujishima, A., and Honda, K. (1972). "Electrochemical photolysis of water at a semiconductor electrode." *nature*, 238(5358), 37–38.

Ganesh, R. S., Sharma, S. K., Durgadevi, E., Navaneethan, M., Binitha, H. S., Ponnusamy, S., Muthamizhchelvan, C., Hayakawa, Y., and Kim, D. Y. (2017). "Surfactant free synthesis of CdS nanospheres, microstructural analysis, chemical bonding, optical properties and photocatalytic activities." *Superlattices and Microstructures*, 104, 247–257.

Gao, Q., Zhao, A., Gan, Z., Tao, W., Li, D., Zhang, M., Guo, H., Wang, D., Sun, H., Mao, R., and Liu, E. (2012). "Facile fabrication and growth mechanism of 3D flower-like Fe3O4 nanostructures and their application as SERS substrates." *CrystEngComm*, 14(14), 4834–4842.

Garg, P., Kumar, S., Choudhuri, I., Mahata, A., and Pathak, B. (2016). "Hexagonal Planar CdS Monolayer Sheet for Visible Light Photocatalysis." *J. Phys. Chem. C*, 120(13), 7052–7060.

Ge, L., and Han, C. (2012). "Synthesis of MWNTs/g-C3N4 composite photocatalysts with efficient visible light photocatalytic hydrogen evolution activity." *Applied Catalysis B: Environmental*, 117–118, 268–274.

Grimme, S. (2004). "Accurate description of van der Waals complexes by density functional theory including empirical corrections." *Journal of Computational Chemistry*, 25(12), 1463–1473.

Gross, E. K. U., and Dreizler, R. M. (2013). *Density Functional Theory*. Springer Science & Business Media.

Guo, J., Zhou, Z., Wang, T., Lu, Z., Yang, Z., and Liu, C. (2017). "Electronic structure and optical properties for blue phosphorene/graphene-like GaN van der Waals heterostructures." *Current Applied Physics*, 17(12), 1714–1720.

Gupta, S., Mehta, B., and R. Satsangi, V. (2012). "Size and oxygen passivation induced reversal of photoconducting behaviour in CdS nanorods." *Nanotechnology*, 23, 355702.

Hafner, J. (2008). "Ab-initio simulations of materials using VASP: Density-functional theory and beyond." *J Comput Chem*, 29(13), 2044–2078.

Han, B., Liu, S., Zhang, N., Xu, Y.-J., and Tang, Z.-R. (2017). "One-dimensional CdS@MoS2 core-shell nanorods for boosted photocatalytic hydrogen evolution under visible light." *Applied Catalysis B: Environmental*, 202, 298–304.

Hashimoto, K., Irie, H., and Fujishima, A. (2005). "TiO2 Photocatalysis: A Historical Overview and Future Prospects." *Jpn. J. Appl. Phys.*, 44(12R), 8269.

Heyd, J., Scuseria, G. E., and Ernzerhof, M. (2003). "Hybrid functionals based on a screened Coulomb potential." *J. Chem. Phys.*, 118(18), 8207–8215.

Hinnemann, B., Moses, P. G., Bonde, J., Jørgensen, K. P., Nielsen, J. H., Horch, S., Chorkendorff, I., and Nørskov, J. K. (2005). "Biomimetic Hydrogen Evolution: MoS2 Nanoparticles as Catalyst for Hydrogen Evolution." *J. Am. Chem. Soc.*, 127(15), 5308–5309.

H. Mir, S., Chakraborty, S., Wärnå, J., Narayan, S., C. Jha, P., K. Jha, P., and Ahuja, R. (2017). "A comparative study of hydrogen evolution reaction on pseudo-monolayer WS 2 and PtS 2 : insights based on the density functional theory." *Catalysis Science & Technology*, 7(3), 687–692.

Hoffmann, M. R., Martin, S. T., Choi, Wonyong., and Bahnemann, D. W. (1995). "Environmental Applications of Semiconductor Photocatalysis." *Chem. Rev.*, 95(1), 69–96.

Hollander, J. M., and Jolly, W. L. (1970). "X-ray photoelectron spectroscopy." *Acc. Chem. Res.*, 3(6), 193–200.

Hu, S., Ma, L., Xie, Y., Li, F., Fan, Z., Wang, F., Wang, Q., Wang, Y., Kang, X., and Wu, G. (2015). "Hydrothermal synthesis of oxygen functionalized S–P codoped g-C3N4 nanorods with outstanding visible light activity under anoxic conditions." *Dalton Trans.*, 44(48), 20889–20897.

Hu, Y., Gao, X., Yu, L., Wang, Y., Ning, J., Xu, S., and Lou, X. W. (David). (2013).

"Carbon-Coated CdS Petalous Nanostructures with Enhanced Photostability and Photocatalytic Activity." *Angewandte Chemie International Edition*, 52(21), 5636–5639.

Huang, Z.-F., Song, J., Pan, L., Wang, Z., Zhang, X., Zou, J.-J., Mi, W., Zhang, X., and Wang, L. (2015). "Carbon nitride with simultaneous porous network and O-doping for efficient solar-energy-driven hydrogen evolution." *Nano Energy*, 12, 646–656.

Isari, A. A., Mehregan, M., Mehregan, S., Hayati, F., Rezaei Kalantary, R., and Kakavandi, B. (2020). "Sono-photocatalytic degradation of tetracycline and pharmaceutical wastewater using WO3/CNT heterojunction nanocomposite under US and visible light irradiations: A novel hybrid system." *Journal of Hazardous Materials*, 390, 122050.

Jank, M., Köser, H., Lücking, F., Martienssen, M., and Wittchen, S. (1998). "Decolorization and Degradation of Erioglaucine (Acid Blue 9) Dye in Wastewater." *Environmental Technology*, 19(7), 741–747.

Joseph, C. G., Li Puma, G., Bono, A., and Krishnaiah, D. (2009). "Sonophotocatalysis in advanced oxidation process: A short review." *Ultrasonics Sonochemistry*, 16(5), 583–589.

Kabra, K., Chaudhary, R., and Sawhney, R. L. (2004). "Treatment of Hazardous Organic and Inorganic Compounds through Aqueous-Phase Photocatalysis: A Review." *Ind. Eng. Chem. Res.*, 43(24), 7683–7696.

Khataee, A. R., and Khataee, H. R. (2008). "Photooxidative removal of the herbicide Acid Blue 9 in the presence of hydrogen peroxide: modeling of the reaction for evaluation of electrical energy per order (EEO)." *Journal of Environmental Science and Health, Part B*, 43(7), 562–568.

Khataee, A. R., Vatanpour, V., and Amani Ghadim, A. R. (2009). "Decolorization of C.I. Acid Blue 9 solution by UV/Nano-TiO2, Fenton, Fenton-like, electro-Fenton and electrocoagulation processes: A comparative study." *Journal of Hazardous Materials*, 161(2), 1225–1233.

Kinney, C. A., Furlong, E. T., Zaugg, S. D., Burkhardt, M. R., Werner, S. L., Cahill, J. D., and Jorgensen, G. R. (2006). "Survey of Organic Wastewater Contaminants in Biosolids Destined for Land Application." *Environ. Sci. Technol.*, 40(23), 7207–7215.

Kohn, W., and Sham, L. J. (1965). "Self-Consistent Equations Including Exchange and Correlation Effects." *Phys. Rev.*, 140(4A), A1133–A1138.

Kong, Z., Chen, X., Ong, W.-J., Zhao, X., and Li, N. (2019). "Atomic-level insight into the mechanism of 0D/2D black phosphorus quantum dot/graphitic carbon nitride (BPQD/GCN) metal-free heterojunction for photocatalysis." *Applied Surface Science*, 463, 1148–1153.

Koper, M. T. M. (2011). "Thermodynamic theory of multi-electron transfer reactions: Implications for electrocatalysis." *Journal of Electroanalytical Chemistry*, Physics and Chemistry of Charge Transfer in Condensed Media, 660(2), 254–260.

Kresse, G., and Furthmüller, J. (1996a). "Efficiency of ab-initio total energy calculations for metals and semiconductors using a plane-wave basis set." *Computational Materials Science*, 6(1), 15–50.

Kresse, G., and Furthmüller, J. (1996b). "Efficient iterative schemes for ab initio total-energy calculations using a plane-wave basis set." *Phys. Rev. B*, 54(16), 11169–11186.

Krukau, A. V., Vydrov, O. A., Izmaylov, A. F., and Scuseria, G. E. (2006). "Influence of the exchange screening parameter on the performance of screened hybrid functionals." *J. Chem. Phys.*, 125(22), 224106.

Kumar, S. G., Kavitha, R., and Nithya, P. M. (2020). "Tailoring the CdS surface structure for photocatalytic applications." *Journal of Environmental Chemical Engineering*, 8(5), 104313.

Kumar, S., Layek, S., Yashpal, M., and Ojha, A. K. (2015). "Room temperature ferromagnetism in undoped and Mn doped CdO nanostructures." *Journal of Magnetism and Magnetic Materials*, 393, 555–561.

Li, F., Bi, W., Kong, T., Wang, C., Li, Z., and Huang, X. (2009). "Effect of sulfur sources on the crystal structure, morphology and luminescence of CdS nanocrystals prepared by a solvothermal method." *Journal of Alloys and Compounds*, 479(1), 707–710.

Li, Q., Guo, B., Yu, J., Ran, J., Zhang, B., Yan, H., and Gong, J. R. (2011). "Highly Efficient Visible-Light-Driven Photocatalytic Hydrogen Production of CdS-Cluster-Decorated Graphene Nanosheets." *J. Am. Chem. Soc.*, 133(28), 10878–10884.

Li, Q., Li, X., Wageh, S., Al-Ghamdi, Ahmed. A., and Yu, J. (2015a). "CdS/Graphene Nanocomposite Photocatalysts." *Advanced Energy Materials*, 5(14), 1500010.

Li, R., Weng, Y., Zhou, X., Wang, X., Mi, Y., Chong, R., Han, H., and Li, C. (2015b). "Achieving overall water splitting using titanium dioxide-based photocatalysts of different phases." *Energy Environ. Sci.*, 8(8), 2377–2382.

Li, X., Zhang, S., and Wang, Q. (2013). "Stability and physical properties of a tri-ring based porous g-C4N3 sheet." *Phys. Chem. Chem. Phys.*, 15(19), 7142–7146.

Li, Y., Liao, H., Ding, Y., Fan, Y., Zhang, Y., and Qian, Y. (1999). "Solvothermal Elemental Direct Reaction to CdE (E = S, Se, Te) Semiconductor Nanorod." *Inorg. Chem.*, 38(7), 1382–1387.

Li, Y., Wu, M., Yang, D., Zeng, H., Zhang, T., Shen, J., Zhang, B., and Li, Q. (2019). "Novel High Efficiency Layered Oxide Photocatalyst Li2SnO3 for Rhodamine B and Tetracycline Degradation." *Catalysts*, 9(9), 712.

Lin, F., Shao, Z., Li, P., Chen, Z., Liu, X., Li, M., Zhang, B., Huang, J., Zhu, G., and Dong, B. (2017). "Low-cost dual cocatalysts BiVO 4 for highly efficient visible photocatalytic oxidation." *RSC Advances*, 7(25), 15053–15059.

Liqiang, J., Yichun, Q., Baiqi, W., Shudan, L., Baojiang, J., Libin, Y., Wei, F., Honggang, F., and Jiazhong, S. (2006). "Review of photoluminescence performance of nano-sized semiconductor materials and its relationships with photocatalytic activity." *Solar Energy Materials and Solar Cells*, 90(12), 1773–1787.

Liu, D., Zhang, C., Yu, Y., Shi, Y., Yu, Y., Niu, Z., and Zhang, B. (2018). "Hydrogen evolution activity enhancement by tuning the oxygen vacancies in self-supported mesoporous spinel oxide nanowire arrays." *Nano Res.*, 11(2), 603–613.

Liu, J. (2015). "Origin of High Photocatalytic Efficiency in Monolayer g-C3N4/CdS Heterostructure: A Hybrid DFT Study." *J. Phys. Chem. C*, 119(51), 28417–28423.

Liu, J., Wang, H., and Antonietti, M. (2016). "Graphitic carbon nitride 'reloaded': emerging applications beyond (photo)catalysis." *Chemical Society Reviews*, 45(8), 2308–2326.

Low, J., Dai, B., Tong, T., Jiang, C., and Yu, J. (n.d.). "In Situ Irradiated X-Ray Photoelectron Spectroscopy Investigation on a Direct Z-Scheme TiO2/CdS Composite Film Photocatalyst." *Advanced Materials*, 0(0), 1802981.

Lynch, M., and Weiner, E. (1979). "HPLC: high performance liquid chromatography." *Environmental Science & Technology*, 13(6), 666–671.

Ma, L., Fan, H., Wang, J., Zhao, Y., Tian, H., and Dong, G. (2016). "Water-assisted ions in situ intercalation for porous polymeric graphitic carbon nitride nanosheets with superior photocatalytic hydrogen evolution performance." *Applied Catalysis B: Environmental*, 190, 93–102.

Ma, S., Xie, J., Wen, J., He, K., Li, X., Liu, W., and Zhang, X. (2017). "Constructing 2D layered hybrid CdS nanosheets/MoS2 heterojunctions for enhanced visible-light photocatalytic H2 generation." *Applied Surface Science*, 2nd International Symposium on Energy and Environmental Photocatalytic Materials, 391, 580–591.

Mamba, G., and Mishra, A. K. (2016). "Graphitic carbon nitride (g-C3N4) nanocomposites: A new and exciting generation of visible light driven photocatalysts for environmental pollution remediation." *Applied Catalysis B: Environmental*, 198, 347–377.
Marinho, B. A., Djellabi, R., Cristóvão, R. O., Loureiro, J. M., Boaventura, R. A. R., Dias, M. M., Lopes, J. C. B., and Vilar, V. J. P. (2017). "Intensification of heterogeneous TiO2 photocatalysis using an innovative micro–meso-structured-reactor for Cr(VI) reduction

under simulated solar light." *Chemical Engineering Journal*, Emerging Advanced Oxidation Processes for the Elimination of Micro-Pollutants, 318, 76–88.

Martin, D. J., Reardon, P. J. T., Moniz, S. J. A., and Tang, J. (2014a). "Visible Light-Driven Pure Water Splitting by a Nature-Inspired Organic Semiconductor-Based System." *J. Am. Chem. Soc.*, 136(36), 12568–12571.

Martin, D. J., Reardon, P. J. T., Moniz, S. J. A., and Tang, J. (2014b). "Visible Light-Driven Pure Water Splitting by a Nature-Inspired Organic Semiconductor-Based System." *J. Am. Chem. Soc.*, 136(36), 12568–12571.

Mir, S. H., Chakraborty, S., Jha, P. C., Wärnå, J., Soni, H., Jha, P. K., and Ahuja, R. (2016). "Two-dimensional boron: Lightest catalyst for hydrogen and oxygen evolution reaction." *Appl. Phys. Lett.*, 109(5), 053903.

Mo, Y., Tian, G., and Tao, J. (2017). "Comparative study of semilocal density functionals on solids and surfaces." *Chemical Physics Letters*, 682, 38–42.

Murphy, A. B. (2007). "Band-gap determination from diffuse reflectance measurements of semiconductor films, and application to photoelectrochemical water-splitting." *Solar Energy Materials and Solar Cells*, 91(14), 1326–1337.

Nørskov, J. K., Bligaard, T., Logadottir, A., Kitchin, J. R., Chen, J. G., Pandelov, S., and Stimming, U. (2005). "Trends in the Exchange Current for Hydrogen Evolution." *J. Electrochem. Soc.*, 152(3), J23.

Omrani, N., and Nezamzadeh-Ejhieh, A. (2020). "A comprehensive study on the enhanced photocatalytic activity of Cu2O/BiVO4/WO3 nanoparticles." *Journal of Photochemistry and Photobiology A: Chemistry*, 389, 112223.

Opoku, F., Govender, K. K., Sittert, C. G. C. E. van, and Govender, P. P. (2018). "Insights into the photocatalytic mechanism of mediator-free direct Z-scheme g-C3N4/Bi2MoO6(010) and g-C3N4/Bi2WO6(010) heterostructures: A hybrid density functional theory study." *Applied Surface Science*, 427, 487–498.

Ouma, C. N. M., Obodo, K. O., Braun, M., Amolo, G. O., and Bessarabov, D. (2019). "Insights on hydrogen evolution reaction in transition metal doped monolayer TcS2 from density functional theory calculations." *Applied Surface Science*, 470, 107–113.

Paier, J., Marsman, M., Hummer, K., Kresse, G., Gerber, I. C., and Ángyán, J. G. (2006). "Screened hybrid density functionals applied to solids." *J. Chem. Phys.*, 124(15), 154709. Panchangam, S. C., Lin, A., Tsai, J.-H., and Lin, C.-F. (2009). "Sonication-assisted photocatalytic decomposition of perfluorooctanoic acid." *Chemosphere*, 75, 654–60.

Pawar, R. C., Khare, V., and Lee, C. S. (2014). "Hybrid photocatalysts using graphitic carbon nitride/cadmium sulfide/reduced graphene oxide (g-C3N4/CdS/RGO) for superior photodegradation of organic pollutants under UV and visible light." *Dalton Trans.*, 43(33), 12514–12527.

Pera-Titus, M., García-Molina, V., Baños, M. A., Giménez, J., and Esplugas, S. (2004). "Degradation of chlorophenols by means of advanced oxidation processes: a general review." *Applied Catalysis B: Environmental*, 47(4), 219–256.

Perdew, J. P., and Wang, Y. (1992). "Accurate and simple analytic representation of the electron-gas correlation energy." *Phys. Rev. B*, 45(23), 13244–13249.

Perdew, J. P., and Zunger, A. (1981). "Self-interaction correction to density-functional approximations for many-electron systems." *Phys. Rev. B*, 23(10), 5048–5079.

Rani, B. J., Kumar, M. P., Ravichandran, S., Ravi, G., Ganesh, V., Guduru, R. K., Yuvakkumar, R., and Hong, S. I. (2019). "WO3 nanocubes for photoelectrochemical water-splitting applications." *Journal of Physics and Chemistry of Solids*, 134, 149–156.

Rao, M. P., Sathishkumar, P., Mangalaraja, R. V., Asiri, A. M., Sivashanmugam, P., and Anandan, S. (2018). "Simple and low-cost synthesis of CuO nanosheets for visible-light-driven photocatalytic degradation of textile dyes." *Journal of Environmental Chemical Engineering*, 6(2), 2003–2010.

Rauf, M. A., and Ashraf, S. S. (2009). "Fundamental principles and application of heterogeneous photocatalytic degradation of dyes in solution." *Chemical Engineering Journal*, 151(1), 10–18.

Roduner, E. (2006). "Size matters: why nanomaterials are different." *Chem. Soc. Rev.*, 35(7), 583–592.

Saien, J., Delavari, H., and Solymani, A. R. (2010). "Sono-assisted photocatalytic degradation of styrene-acrylic acid copolymer in aqueous media with nano titania particles and kinetic studies." *Journal of Hazardous Materials*, 177(1), 1031–1038.

Saikia, L., Bhuyan, D., Saikia, M., Malakar, B., Dutta, D. K., and Sengupta, P. (2015). "Photocatalytic performance of ZnO nanomaterials for self sensitized degradation of malachite green dye under solar light." *Applied Catalysis A: General*, 490, 42–49.

Sánchez-Martín, J., Beltrán-Heredia, J., and Rodríguez-Sánchez, M. T. (2012). "Removal of Erioglaucine (Acid Blue 9) with a new coagulant agent from Acacia mearnsii tannin extract." *Coloration Technology*, 128(1), 15–20.

Schultz, D. M., and Yoon, T. P. (2014). "Solar Synthesis: Prospects in Visible Light Photocatalysis." *Science*, 343(6174), 1239176.

Seh, Z. W., Kibsgaard, J., Dickens, C. F., Chorkendorff, I., Nørskov, J. K., and Jaramillo, T. F. (2017). "Combining theory and experiment in electrocatalysis: Insights into materials design." *Science*, 355(6321).

Serpone, N., and Pelizzetti, E. (1989). *Photocatalysis: fundamentals and applications*. Wiley.

Shang, X., Rao, Y., Lu, S.-S., Dong, B., Zhang, L.-M., Liu, X.-H., Li, X., Liu, Y.-R., Chai, Y.-M., and Liu, C.-G. (2017). "Novel WS2/WO3 heterostructured nanosheets as efficient electrocatalyst for hydrogen evolution reaction." *Materials Chemistry and Physics*, 197, 123–128.

Sharma, S., Dutta, V., Raizada, P., Hosseini-Bandegharaei, A., Singh, P., and Nguyen, V.-H. (2021). "Tailoring cadmium sulfide-based photocatalytic nanomaterials for water decontamination: a review." *Environ Chem Lett*, 19(1), 271–306.

Singh, A., and Sinha, A. S. K. (2018). "Active CdS/rGO photocatalyst by a high temperature gas-solid reaction for hydrogen production by splitting of water." *Applied Surface Science*, 2nd International Workshop on Graphene and C3N4-based Photocatalysts, 430, 184–197.

Snyder, S. A., Westerhoff, P., Yoon, Y., and Sedlak, D. L. (2003). "Pharmaceuticals, Personal Care Products, and Endocrine Disruptors in Water: Implications for the Water Industry." *Environmental Engineering Science*, 20(5), 449–469.

Spasiano, D., Marotta, R., Malato, S., Fernandez-Ibañez, P., and Di Somma, I. (2015). "Solar photocatalysis: Materials, reactors, some commercial, and pre-industrialized applications. A comprehensive approach." *Applied Catalysis B: Environmental*, 170–171, 90–123.

Sridharan, K., Jang, E., and Joo Park, T. (2013a). "Deformation assisted fabrication of uniform spindle, tube and rod shaped nanoscale 3D TiO 2 architectures and their photocatalytic activity." *CrystEngComm*, 15(41), 8241–8245.

Sridharan, K., Jang, E., Park, J. H., Kim, J.-H., Lee, J.-H., and Park, T. J. (2015a). "Silver Quantum Cluster (Ag9)-Grafted Graphitic Carbon Nitride Nanosheets for Photocatalytic Hydrogen Generation and Dye Degradation." *Chemistry – A European Journal*, 21(25), 9126–9132.

Sridharan, K., Jang, E., and Park, T. J. (2013b). "Novel visible light active graphitic C3N4– TiO2 composite photocatalyst: Synergistic synthesis, growth and photocatalytic treatment of hazardous pollutants." *Applied Catalysis B: Environmental*, 142–143, 718–728.

Sridharan, K., Jang, E., Park, Y. M., and Park, T. J. (2015b). "Superior Photostability and Photocatalytic Activity of ZnO Nanoparticles Coated with Ultrathin TiO2 Layers through Atomic-Layer Deposition." *Chem. Eur. J.*, 21(52), 19136–19141.

Sridharan, K., Kuriakose, T., Philip, R., and Park, T. J. (2014a). "Transition metal (Fe, Co and Ni) oxide nanoparticles grafted graphitic carbon nitrides as efficient optical limiters and recyclable photocatalysts." *Applied Surface Science*, 308, 139–147.

Sridharan, K., and Park, T. J. (2013). "Thorn-ball shaped TiO2 nanostructures: Influence of Sn2+ doping on the morphology and enhanced visible light photocatalytic activity." *Applied Catalysis B: Environmental*, 134–135, 174–184.

Sridharan, K., Roy, N., Philip, R., and Park, T. J. (2014b). "Anomalous growth of multi-phased and multi-dimensional Manganese oxide–Metal (Fe, Co and Ni) oxide nanostructures: Synthesis and optical limiting properties." *Journal of Alloys and Compounds*, 611, 82–90.

Su, D. S., Zhang, J., Frank, B., Thomas, A., Wang, X., Paraknowitsch, J., and Schlögl, R. (2010). "Metal-Free Heterogeneous Catalysis for Sustainable Chemistry." *ChemSusChem*, 3(2), 169–180.

Tan, T. L., Wang, L.-L., Johnson, D. D., and Bai, K. (2013). "Hydrogen Deposition on Pt(111) during Electrochemical Hydrogen Evolution from a First-Principles Multiadsorption-Site Study." *J. Phys. Chem. C*, 117(44), 22696–22704.

Tian, H., Fan, H., Ma, J., Liu, Z., Ma, L., Lei, S., Fang, J., and Long, C. (2018). "Pt-decorated zinc oxide nanorod arrays with graphitic carbon nitride nanosheets for highly efficient dual-functional gas sensing." *Journal of Hazardous Materials*, 341, 102–111.

Tsai, C., Chan, K., K. Nørskov, J., and Abild-Pedersen, F. (2015). "Rational design of MoS 2 catalysts: tuning the structure and activity via transition metal doping." *Catalysis Science & Technology*, 5(1), 246–253.

Vaquero, F., Navarro, R. M., and Fierro, J. L. G. (2017). "Influence of the solvent on the structure, morphology and performance for H2 evolution of CdS photocatalysts prepared by solvothermal method." *Applied Catalysis B: Environmental*, 203, 753–767.

Voiry, D., Yang, J., and Chhowalla, M. (2016). "Recent Strategies for Improving the Catalytic Activity of 2D TMD Nanosheets Toward the Hydrogen Evolution Reaction." *Advanced Materials*, 28(29), 6197–6206.

Wang, C., Fan, H., Ren, X., and Fang, J. (2018). "Room temperature synthesis and enhanced photocatalytic property of CeO2/ZnO heterostructures." *Appl. Phys. A*, 124(2), 99.

Wang, Q. H., Kalantar-Zadeh, K., Kis, A., Coleman, J. N., and Strano, M. S. (2012a). "Electronics and optoelectronics of two-dimensional transition metal dichalcogenides." *Nature Nanotechnology*, 7(11), 699.

Wang, X., Blechert, S., and Antonietti, M. (2012b). "Polymeric Graphitic Carbon Nitride for Heterogeneous Photocatalysis." *ACS Catal.*, 2(8), 1596–1606.

Wang, X., Maeda, K., Thomas, A., Takanabe, K., Xin, G., Carlsson, J. M., Domen, K., and Antonietti, M. (2009a). "A metal-free polymeric photocatalyst for hydrogen production from water under visible light." *Nature Materials*, 8(1), 76.

Wang, X., Maeda, K., Thomas, A., Takanabe, K., Xin, G., Carlsson, J. M., Domen, K., and Antonietti, M. (2009b). "A metal-free polymeric photocatalyst for hydrogen production from water under visible light." *Nat Mater*, 8(1), 76–80.

Wang, Y., Wang, F., and He, J. (2013). "Controlled fabrication and photocatalytic properties of a three-dimensional ZnO nanowire/reduced graphene oxide/CdS heterostructure on carbon cloth." *Nanoscale*, 5(22), 11291–11297.

Warren, B., and Diffraction, X. (1969). "Courier Dover Publications." *New York*.

Wei, C., Cheng, C., Zhao, J., Zheng, S., Hao, M., and Pang, H. (2014). "Assembling CdS mesoporous nanosheets into 3D hierarchitectures for effective photocatalytic performance." *Dalton Transactions*, 43(15), 5687–5693.

Wei, S.-H., and Zhang, S. B. (2000). "Structure stability and carrier localization in $\mathrm{Cd}X(X=\mathrm{S},\mathrm{}\mathrm{S}\mathrm{e},\mathrm{}\mathrm{Te})$ semiconductors." *Phys. Rev. B*, 62(11), 6944–6947.

Williams, D. B., and Carter, C. B. (1996). "The Transmission Electron Microscope." *Transmission Electron Microscopy*, Springer, Boston, MA, 3–17.

Xiao, X., and Zhang, W.-D. (2010). "Facile synthesis of nanostructured BiOI microspheres with high visible light-induced photocatalytic activity." *Journal of Materials Chemistry*, 20(28), 5866–5870.

Xiong, J., Li, Z., Chen, J., Zhang, S., Wang, L., and Dou, S. (2014). "Facile Synthesis of Highly Efficient One-Dimensional Plasmonic Photocatalysts through Ag@Cu2O Core–Shell Heteronanowires." *ACS Appl. Mater. Interfaces*, 6(18), 15716–15725.

Xiong, S., Xi, B., Wang, C., Zou, G., Fei, L., Wang, W., and Qian, Y. (2007). "Shape-Controlled Synthesis of 3D and 1D Structures of CdS in a Binary Solution with L-Cysteine's Assistance." *Chemistry – A European Journal*, 13(11), 3076–3081.

Xu, Y., and Schoonen, M. A. A. (2000). "The absolute energy positions of conduction and valence bands of selected semiconducting minerals." *American Mineralogist*, 85(3–4), 543–556.

Xu, Y., and Zhang, W.-D. (2015). "CdS/g-C3N4 Hybrids with Improved Photostability and Visible Light Photocatalytic Activity." *European Journal of Inorganic Chemistry*, 2015(10), 1744–1751.

Yan, Z., Sun, Z., Liu, X., Jia, H., and Du, P. (2016). "Cadmium sulfide/graphitic carbon nitride heterostructure nanowire loading with a nickel hydroxide cocatalyst for highly efficient photocatalytic hydrogen production in water under visible light." *Nanoscale*, 8(8), 4748–4756.

Ye, M.-Y., Zhao, Z.-H., Hu, Z.-F., Liu, L.-Q., Ji, H.-M., Shen, Z.-R., and Ma, T.-Y. (2017). "0D/2D Heterojunctions of Vanadate Quantum Dots/Graphitic Carbon Nitride Nanosheets for Enhanced Visible-Light-Driven Photocatalysis." *Angewandte Chemie International Edition*, 56(29), 8407–8411.

Yin, W.-J., Tang, H., Wei, S.-H., Al-Jassim, M. M., Turner, J., and Yan, Y. (2010). "Band structure engineering of semiconductors for enhanced photoelectrochemical water splitting: The case of ${\text{TiO}}2$." *Phys. Rev. B*, 82(4), 045106.

Yu, J., Qi, L., and Jaroniec, M. (2010). "Hydrogen Production by Photocatalytic Water Splitting over Pt/TiO2 Nanosheets with Exposed (001) Facets." *J. Phys. Chem. C*, 114(30), 13118–13125.

Yu, J., Yu, Y., Zhou, P., Xiao, W., and Cheng, B. (2014). "Morphology-dependent photocatalytic H2-production activity of CdS." *Applied Catalysis B: Environmental*, 156–157, 184–191.

Yu, W., Chen, J., Shang, T., Chen, L., Gu, L., and Peng, T. (2017). "Direct Z-scheme g-C3N4/WO3 photocatalyst with atomically defined junction for H2 production." *Applied Catalysis B: Environmental*, 219, 693–704.

Yu, W., Zhang, S., Chen, J., Xia, P., Richter, M. H., Chen, L., Xu, W., Jin, J., Chen, S., and Peng, T. (2018). "Biomimetic Z-scheme photocatalyst with a tandem solid-state electron flow catalyzing H2 evolution." *J. Mater. Chem. A*, 6(32), 15668–15674.

Yuan, Y.-J., Chen, D., Yu, Z.-T., and Zou, Z.-G. (2018). "Cadmium sulfide-based nanomaterials for photocatalytic hydrogen production." *Journal of Materials Chemistry A*, 6(25), 11606–11630.

Yuan, Y.-J., Shen, Z., Wu, S., Su, Y., Pei, L., Ji, Z., Ding, M., Bai, W., Chen, Y., Yu, Z.-T., and Zou, Z. (2019). "Liquid exfoliation of g-C3N4 nanosheets to construct 2D-2D MoS2/g-C3N4 photocatalyst for enhanced photocatalytic H2 production activity." *Applied Catalysis B: Environmental*, 246, 120–128.

Yue, X., Yi, S., Wang, R., Zhang, Z., and Qiu, S. (2016). "Cadmium Sulfide and Nickel Synergetic Co-catalysts Supported on Graphitic Carbon Nitride for Visible-Light-Driven Photocatalytic Hydrogen Evolution." *Sci Rep*, 6.

Zeng, Y., Guo, N., Li, H., Wang, Q., Xu, X., Yu, Y., Han, X., and Yu, H. (2019a). "A novel route to manufacture WO3@MoS2 p–n heterostructure hollow tubes with enhanced photocatalytic activity." *Chem. Commun.*, 55(5), 683–686.

Zeng, Y., Guo, N., Xu, X., Yu, Y., Wang, Q., Wang, N., Han, X., and Yu, H. (2019b). "Degradation of bisphenol a using peroxymonosulfate activated by WO3@MoS2/Ag hollow nanotubes photocatalyst." *Chemosphere*, 227, 589–597.

Zhang, H., Wang, S., Wang, Y., Yang, J., Gao, X., and Wang, L. (2014a). "TiO2(B) nanoparticle-functionalized WO3 nanorods with enhanced gas sensing properties." *Phys. Chem. Chem. Phys.*, 16(22), 10830–10836.

Zhang, J., Sun, J., Maeda, K., Domen, K., Liu, P., Antonietti, M., Fu, X., and Wang, X. (2011). "Sulfur-mediated synthesis of carbon nitride: Band-gap engineering and improved functions for photocatalysis." *Energy & Environmental Science*, 4(3), 675–678.

Zhang, J., Wageh, S., Al-Ghamdi, AhmedA., and Yu, J. (2016). "New understanding on the different photocatalytic activity of wurtzite and zinc-blende CdS." *Applied Catalysis B: Environmental*, 192, 101–107.

Zhang, J., Zhu, Z., and Feng, X. (2014b). "Construction of Two-Dimensional MoS2/CdS p–n Nanohybrids for Highly Efficient Photocatalytic Hydrogen Evolution." *Chem. Eur. J.*, 20(34), 10632–10635.

Zhang, J.-R., Zhao, Y.-Q., Chen, L., Yin, S.-F., and Cai, M.-Q. (2019a). "Density functional theory calculation on facet-dependent photocatalytic activity of MoS2/CdS heterostructures." *Applied Surface Science*, 469, 27–33.

Zhang, L., Zhang, H., Jiang, C., Yuan, J., Huang, X., Liu, P., and Feng, W. (2019b). "Z-scheme system of WO3@MoS2/CdS for photocatalytic evolution H2: MoS2 as the charge

transfer mode switcher, electron-hole mediator and cocatalyst." *Applied Catalysis B: Environmental*, 259, 118073.

Zhang, M., Xu, Y., Fan, H., Zhao, N., Yan, B., Wang, C., Ma, J., Yadav, A. K., Zhang, W., Du, Z., Zheng, X., Li, M., Dong, G., and Wang, W. (2020). "In situ synthesis of 3D Co@Co3O4 nanosheet arrays for hybrid supercapacitors with ultra-high rate performance." *Journal of Alloys and Compounds*, 826, 154115.

Zhao, N., Fan, H., Zhang, M., Wang, C., Ren, X., Peng, H., Li, H., Jiang, X., and Cao, X. (2019). "Preparation of partially-cladding NiCo-LDH/Mn3O4 composite by electrodeposition route and its excellent supercapacitor performance." *Journal of Alloys and Compounds*, 796, 111–119.

Zhao, W., Zhang, C., Geng, F., Zhuo, S., and Zhang, B. (2014). "Nanoporous Hollow Transition Metal Chalcogenide Nanosheets Synthesized via the Anion-Exchange Reaction of Metal Hydroxides with Chalcogenide Ions." *ACS Nano*, 8(10), 10909–10919.

Zhao, Y., Fang, Z.-B., Feng, W., Wang, K., Huang, X., and Liu, P. (2018). "Hydrogen Production from Pure Water via Piezoelectric-assisted Visible-light Photocatalysis of CdS Nanorod Arrays." *ChemCatChem*, 10(16), 3397–3401.

Zheng, D., zhang, G., and Wang, X. (2015). "Integrating CdS quantum dots on hollow graphitic carbon nitride nanospheres for hydrogen evolution photocatalysis." *Applied Catalysis B: Environmental*, 179, 479–488.

Zhou, B.-X., Ding, S.-S., Zhang, B.-J., Xu, L., Chen, R.-S., Luo, L., Huang, W.-Q., Xie, Z., Pan, A., and Huang, G.-F. (2019). "Dimensional transformation and morphological control of graphitic carbon nitride from water-based supramolecular assembly for

photocatalytic hydrogen evolution: from 3D to 2D and 1D nanostructures." *Applied Catalysis B: Environmental*, 254, 321–328.

Zhu, J., Wang, Z.-C., Dai, H., Wang, Q., Yang, R., Yu, H., Liao, M., Zhang, J., Chen, W., Wei, Z., Li, N., Du, L., Shi, D., Wang, W., Zhang, L., Jiang, Y., and Zhang, G. (2019). "Boundary activated hydrogen evolution reaction on monolayer MoS 2." *Nature Communications*, 10(1), 1348.

Zou, Y., Shi, J.-W., Ma, D., Fan, Z., Cheng, L., Sun, D., Wang, Z., and Niu, C. (2018). "WS2/Graphitic Carbon Nitride Heterojunction Nanosheets Decorated with CdS Quantum Dots for Photocatalytic Hydrogen Production." ChemSusChem, 11(7), 1187–1197.

Miss. Sulakshana Shenoy
Research Scholar
Department of Physics,
National Institute of Technology Karnataka
Surathkal 575 025, Karnataka, INDIA
Email: shenoy26sulakshana@gmail.com
Phone: +91 9108124363
Web: https://scholar.google.com/citations?user=uFAtsacAAAAJ&hl=en

Education

PhD in Physics	National Institute of Technology
Advisors: Dr. Kartick Tarafder and Dr. Kishore Sridharan	Karnataka (NITK), Surathkal,
Thesis Title: Photo-physical studies and bandgap	Karnataka, India
engineering on transition metal chalcogenides for	July 2016 – Present
applications in photocatalysis.	

MSc in Physics   National Institute of Technology
Thesis Title: Synthesis, characterization and   Karnataka (NITK), Surathkal,
electrochemical study of vanadium pentoxide-graphene   Karnataka, India
oxide nanocomposites.   May 2015

BSc in Physics, Chemistry, Mathematics   St. Agnes College
(Autonomous), Mangalore,
Karnataka, India
June 2013

Research Expertise

- Synthesis of functional nanomaterials consisting of metal oxides, doped metal oxides, transition metal chalcogenides, graphene oxide and carbon nitride-based nanocomposites using solid-state pyrolysis approach, hydrothermal, solvothermal, co-precipitation and ultrasonic techniques.

- Design and development of novel nanostructured materials capable of exhibiting good photocatalytic activity under visible light towards the degradation of organic pollutants (dyes and emerging pollutants) and for hydrogen generation.

- Hands on experience in using sophisticated instruments: X-ray Diffractometer (XRD), Photoluminescence spectrophotometer (PL), UV-Visible spectrophotometer, High performance liquid chromatography (HPLC), electrochemical workstation.

- Expertise in high performance computing (HPC) using Density Functional Theory (DFT) for molecular modelling and investigating their structural, electronic and optical properties.

- Prediction of semiconductor band edges with respect to redox potentials using first-principles calculation.

- Hands on experience in professional software: VASP, DLPOLY, SIESTA, Quantum ESPRESSO and QuantumATK.

List of Publications

1. Antil, B., Kumar, L., Ranjan, R., **Shenoy, S**., Tarafder, K., Gopinath, C.S., Deka, S., 2021. One-Dimensional Multichannel g-C3N4.7 Nanostructure Realizing an Efficient Photocatalytic Hydrogen Evolution Reaction and Its Theoretical Investigations. ACS Appl. Energy Mater. https://doi.org/10.1021/acsaem.0c02858

2. Bhat, K.S., **Shenoy, S.,** Nagaraja, H.S., Sridharan, K., 2017. Porous cobalt chalcogenide nanostructures as high performance pseudo-capacitor electrodes. Electrochimica Acta 248, 188–196. https://doi.org/10.1016/j.electacta.2017.07.137

3. Hadagalli, K., **Shenoy, S.,** Shakya, K.R., G, M., Tarafder, K., Mandal, S., Basu, B., 2021. Effect of Fe3+ substitution on the structural modification and band structure modulated UV absorption of hydroxyapatite. International Journal of Applied Ceramic Technology 18, 332–344. https://doi.org/10.1111/ijac.13674

4. Payra, S., **Shenoy, S.,** Chakraborty, C., Tarafder, K., Roy, S., 2020. Structure-Sensitive Electrocatalytic Reduction of CO2 to Methanol over Carbon-Supported Intermetallic PtZn Nano-Alloys. ACS Appl. Mater. Interfaces 12, 19402–19414. https://doi.org/10.1021/acsami.0c00521

5. **Shenoy, S.,** Ahmed, S., Lo, I.M.C., Singh, S., Sridharan, K., 2021a. Rapid sonochemical synthesis of copper doped ZnO grafted on graphene as a multi-component hierarchically structured visible-light-driven photocatalyst. Materials Research Bulletin 140, 111290. https://doi.org/10.1016/j.materresbull.2021.111290

6. **Shenoy, S.,** Jang, E., Park, T.J., Gopinath, C.S., Sridharan, K., 2019. Cadmium sulfide nanostructures: Influence of morphology on the photocatalytic degradation of erioglaucine and hydrogen generation. Applied Surface Science 483, 696–705. https://doi.org/10.1016/j.apsusc.2019.04.018

7. **Shenoy, S.,** Sridharan, K., 2020. Bismuth oxybromide nanoplates embedded on activated charcoal as effective visible light driven photocatalyst. Chemical Physics Letters 749, 137435. https://doi.org/10.1016/j.cplett.2020.137435

8. **Shenoy, S.,** Tarafder, K., 2020. Enhanced photocatalytic efficiency of layered CdS/CdSe heterostructures: Insights from first principles electronic structure calculations. J. Phys.: Condens. Matter 32, 275501. https://doi.org/10.1088/1361-648X/ab7b1c

9. **Shenoy, S.,** Tarafder, K., Sridharan, K., 2021b. Bimetallic nanoparticles grafted ZnO hierarchical structures as efficient visible light driven photocatalyst: An experimental and theoretical study. Journal of Molecular Structure 1236, 130355. https://doi.org/10.1016/j.molstruc.2021.130355

10. **Shenoy, S.,** Tarafder, K., Sridharan, K., 2020. Graphitic C3N4/CdS composite photocatalyst: Synthesis, characterization and photodegradation of methylene blue under visible light. Physica B: Condensed Matter 595, 412367. https://doi.org/10.1016/j.physb.2020.412367

11. Sreejesh, M., **Shenoy, S.,** Sridharan, K., Kufian, D., Arof, A.K., Nagaraja, H.S., 2017. Melt quenched vanadium oxide embedded in graphene oxide sheets as composite electrodes for amperometric dopamine sensing and lithium ion battery applications. Applied Surface Science 410, 336–343. https://doi.org/10.1016/j.apsusc.2017.02.246

12. Sridharan, K., **Shenoy, S.,** Kumar, S.G., Terashima, C., Fujishima, A., Pitchaimuthu, S., 2021. Advanced Two-Dimensional Heterojunction Photocatalysts of Stoichiometric and Non-Stoichiometric Bismuth Oxyhalides with Graphitic Carbon Nitride for Sustainable Energy and Environmental Applications. Catalysts 11, 426. https://doi.org/10.3390/catal11040426

Conference

- Graphitic C_3N_4/CdS composite photocatalyst: Synthesis, characterization and photodegradation of methylene blue under visible light, **Current Trends in Functional Material**, CTFM-2020, NITK, Surathkal *(Oral presentation)*.

- A robust photocatalyst using silver quantum clusters grafted in titanium dioxide nanotubes, **International conference on Zero Dimensional Materials,** P.C. Jabin Science College, Hubballi, Karnataka *(Oral presentation)*.

- Short term courses on the topic – **Basic Principles of DFT Calculations and Molecular Dynamics Simulation**, November 2020, Department of Chemical Engineering, MNIT, Jaipur, Rajasthan.